Confined ensembles of highly charged ions for studies of light-matter interaction at high intensities: The HILITE Penning trap setup

Dissertation zur Erlangung des Grades
Dr. rerum naturalium

FRIEDRICH-SCHILLER-UNIVERSITÄT JENA
PHYSIKALISCH-ASTRONOMISCHE FAKULTÄT

seit 1558

eingereicht von Nils Simon Stallkamp,
geboren am 14.01.1987 in Bad Dürkheim

Zusammenfassung

Die Untersuchung der Wechselwirkung zwischen Materie und Licht geht zurück auf die Beschreibung des 'photoelektrischen Effekts' zu Beginn des 20. Jahrhunderts. Mit der Entwicklung der ersten Lasersysteme, insbesondere von Systemen mit hoher Intensität und/oder hoher Photonenenergie, drang die Forschung sukzessive in neue Bereiche der Wechselwirkung vor. Zuvor unbekannte, nicht-lineare Effekte wie beispielsweise die Multiphotonenionisation oder Tunnelionisation traten auf und wurden Gegenstand theoretischer Fragestellungen und experimenteller Untersuchungen.

Unabhängig davon entwickelten sich parallel die Speichertechniken für geladene Teilchen (Elektronen und Ionen) weiter und führten zu verschiedenen Fallensystemen, wie beispielsweise der Paul- und der Penning-Falle. Aufgrund ihrer Eigenschaften die Teilchen lokalisiert in einem kleinen Volumen, in Ruhe, für eine im Grunde unbegrenzte Zeit zu speichern und zerstörungsfrei zu detektieren, ermöglichten sie fundamentale Eigenschaften der Materie (beispielsweise g-Faktor, Massenbestimmung) mit bis dahin unerreichter Präzision zu bestimmen und dadurch Vorhersagen des Standardmodells zu verifizieren.

Mit dem hier vorgestellten HILITE-Experiment (_H_igh-_I_ntensity _L_aser _I_on _T_rap _E_xperiment) sollen erstmals die Vorzüge der Penning-Falle hinsichtlich der Lokalisierung und Teilchenpräparation genutzt werden um Ionisationsexperimente an Hochintensitätslasern durchzuführen. Besonderes Augenmerk wurde dabei auf die Kompaktheit und Transportierbarkeit des ganzen Systems gelegt um an unterschiedlichen Laseranlagen genutzt werden zu können, deren Auswahl nach den Erfordernissen (hohe Intensität oder hohe Photonenenergie) der experimentellen Fragestellung erfolgt. Kentnisse über die Teilcheneigenschaften vor dem Laserbeschuss, wie beispielsweise deren Ladungszustand, reduzieren den Aufwand der theoretischen Beschreibung und vereinfachen ihn dadurch. Theoretische Vorhersagen physikalischer Größen, wie beispielsweise von Ionisationsquerschnitten, können dadurch besser mit den experimentell gewonnenen Ergebnissen verglichen werden.

Im Rahmen dieser Arbeit wurde das Experiment mit einer eigenen Ionenquelle, einer Ionenselektion, einer Strahlführung, sowie unter Abbremsung und Einfang in die Penning-Falle,

zunächst ohne Laser, an der GSI Helmholtzzentrum für Schwerionenforschung GmbH in Betrieb genommen. Die Speicherung sowie der resonante, zerstörungsfreie Teilchennachweis innerhalb der Falle konnten gezeigt werden. Die einzelnen Komponenten wurden charakterisiert und in ihrer Funktionsweise überprüft. Darüber hinaus wurde eine erste Strahlzeit an einer externen Laseranlage (FLASH am DESY) beantragt und auch durchgeführt. Die Interaktion zwischen Laser und gespeicherten Ionen konnte dabei für niedriggeladene Ionen nachgewiesen werden, allerdings verhinderten unvorhersehbare schlechte Vakuumbedingungen die Messung der eigentlich vorgesehenen Ionenspezies. Auf Grundlage dieser Erfahrungen wurden verschiedene Anpassungen und Verbesserungen an der Apparatur für zukünftige Strahlzeiten geplant und teilweise auch schon vorgenommen.

Abstract

The investigation of light-matter interactions is based on the description of the 'photoelectric effect' in the early 20th century. The development of the first laser systems, especially of systems with high intensities and/or high photon energies allowed science to enter new interaction regimes. Previously unknown, non-linear effects like multiphoton or tunnel ionisation processes occurred and became subject of theoretical descriptions and experimental studies.

Independently, the storage techniques for charged particles (electrons and ions) developed in parallel and different kind of devices, like Paul and Penning traps, had been invented in the 1950s and 1960s to study fundamental parameters of matter (for instance g-factor, mass etc.) with previously unknown accuracy. Thereby, they were able to verify predictions given by the Standard Model.

The HILITE experiment (*High-Intensity Laser Ion Trap Experiment*), presented within this thesis, is designed to combine and use for the first time the advantageous properties of target preparation a Penning trap can provide, like ensemble temperature, purity and localizability, in order to investigate laser-ion interactions at high intensities. Particular attention was paid to the compactness of the setup in order to be capable to transport the experiment to different laser facilities and perform experiments on site. According to the requirements (high intensities or high photon energies) of the experimental question, their selection is done. By knowing the target properties before the laser irradiation, for instance the charge state, precisely, allows theory to reduce the amount of occurring interactions and by that a 'simpler' description. Theoretical predictions of physical quantities, like ionisation cross sections, can therefore be linked better to the experimental data.

In the frame of this thesis, the experimental setup was built and put into operation in terms of its dedicated ion source, ion selection, beam transport, deceleration and capture inside the Penning trap at the GSI Helmholtzzentrum für Schwerionenforschung GmbH. During commissioning, the storage and non-destructive detection of pure ion ensembles within the trap was demonstrated. The individual components have been characterised and

their operation was checked. Additionally, a propsal was handed in for the first beamtime at an external laser facility (FLASH at DESY), which was granted and carried out. The interaction between the laser and low charged ions could be verified. Unfortunately an unexpected high background pressure prevented the measurement of the previously planned ion species. Due to the experiences gained, some improvements and adaptions are planned or have been already implemented for future laser experiments.

Contents

Contents

1. Introduction and motivation

This chapter gives a brief description of the history related to the topic of light-matter interaction in general, as well as the development over the last decades of tools, such as laser systems as monochromatic, coherent and intense light sources and Penning traps as devices for the confinement and study of electrically charged particles and their properties. The HILITE Penning trap is such a tool and will be presented in the scope of this thesis.

1.1. Light-matter interaction

Over 100 years ago, back in the late 80s and 90s of the 19th century, it was Heinrich Hertz while studying the effects of the transmission of electromagnetic waves, who recognized that the spark discharge between two electrodes was affected while illuminated by UV light [1, 2]. Based on those results, Wilhelm Hallwachs conducted an experiment to investigate this effect further one year later. He used an experimental setup specially designed for this purpose, and found out that the sign of the charge in the spark was negative [3]. In 1899 Philipp Lenard further improved the experimental conditions by evacuating the setup and was able to extract the specific charge q/m of the released negative charges to be the same as the one Thomson had found for free electrons [4]. Additional systematic measurements revealed characteristic properties of this 'photoelectric effect' like:

- The velocity of extracted particles is independent of the light intensity, but dependent on the 'sort of light' - today known as frequency, as well as the material they are released from.

- The number of extracted electrical particles is proportional to the light intensity.

On the basis of those experimental results and referring to Max Planck's work [5], Albert Einstein postulated in 1905 that monochromatic light, which was described in terms of an electromagnetic wave at that time, behaves like an energy quantum with a specific amount

1. Introduction and motivation

$h\nu$ [6]. Considering energy conservation he formulated

$$h\nu = \frac{m}{2}v^2 + e\phi \tag{1.1}$$

connecting the properties of the light $h\nu$, with the energy of the released electrons $\frac{m}{2}v^2$ and material quantities $e\phi$, nowadays known as the 'work function' W. A work for which he was awarded the Nobel Prize in physics in 1921.

Today one distinguishes between three different cases of this effect. The *outer* and *inner photoelectric effect* as well as *photo-ionisation*.

Outer photoelectric effect

This effect basically describes the situation found and studied by Hertz, Hallwachs, Lenard and Einstein. For a conductor or semiconductor illuminated by light, electrons can be extracted from the surface with a certain kinetic energy and be detected. This energy depends on the frequency of the light and the work function of the material as can be seen in equation (1.1). A schematic in figure (1.1 (a)) shows the principle in terms of the band structure in solid-state physics. If the frequency and by that the energy of the incident light is sufficient, nearly-free electrons in the valence band can gain enough energy to overcome the gap between the Fermi energy E_F for conductors, or valence band energy E_{val} for semiconductors and the vacuum-energy E_{vac}.

Inner Photoelectric effect

As the name suggests, the inner photoelectric effect does not result in an emission of photo-electrons by incident light on a surface, rather than in internal 'excitation' of electrons. It only occurs in semiconductors, where a characteristic band-gap E_{gap} between the valence band and the conduction band exists. By illumination with a frequency sufficient to overcome this band-gap, electrons from the valence band can be lifted into the conduction band and by that a change in the conductivity of the semiconductor can be achieved. An example of such a case is the working principle of a solar cell. As previously, a schematic in figure (1.1 (b)) shows the concept in terms of the band structure.

Photo-ionisation

In the case of photo-ionisation one leaves the picture of a solid-state and corresponding description of atoms in a lattice and goes over to free atoms and molecules. Due to non-overlapping energy states of the single atoms, the model of valence and conduction

bands does not hold any more. The electrons are in general more tightly bound to their nucleus and therefore the energy needed to remove them is typically higher. Like in the cases before, a schematic in figure (1.1 (c)) shows the process occurring.
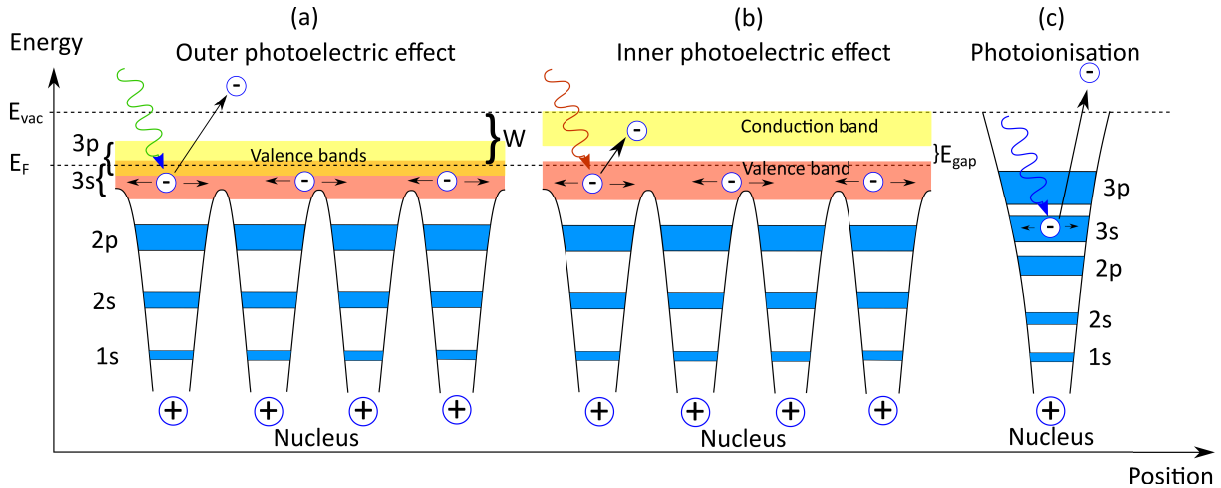
Figure 1.1.: Principle sketch of the three different processes. (a) Outer photoelectric effect: Nearly-free electrons from the valence band can be released by a photon of sufficient energy to overcome the work function W. (b) Inner photoelectric effect: The incident photon has enough energy to lift an electron from the valence band over the band gap into the conduction band leading to a change in conductivity of the semiconductor. (c) Photo-ionisation: Electrons are more strongly bound than in the solid-state case. Hence, the energy to overcome the ionisation potential is higher and therefore a more energetic photon is needed.

The scope of this thesis is on photo-ionisation, in particular from one specific charge state of an ion to the next higher one. In such cases, the energy needed for a further ionisation, which is provided by the photon, has to be increased. This can easily be explained by picture (1.1 (c)) if one starts with the electron already in the 1s or 2s state instead of the 3s as it is shown there. The remaining bound electrons are located in the inner shells, so their probability being close to the nucleus is larger than for the outer shells, and by that the influence of the core potential is higher. Additionally, the heavier the nucleus, the stronger the potential 'seen' by the electrons. Therefore, the ionisation energy needed can easily reach from several tens of electronvolts for low charge states and light species (low-Z), over hundreds of electronvolts for medium-Z species up to kilo-electronvolts for high-Z systems. As an example figure (1.2) shows the ionisation energy as a function of the charge state for argon. Closed shells can easily be seen by a jump in energy due to higher probability of being closer to the nucleus and by that seeing higher core potential. It is obvious that

Figure 1.2: Ionisation energy as a function of the charge state for argon. Closed shells can easily be seen by a jump in energy.
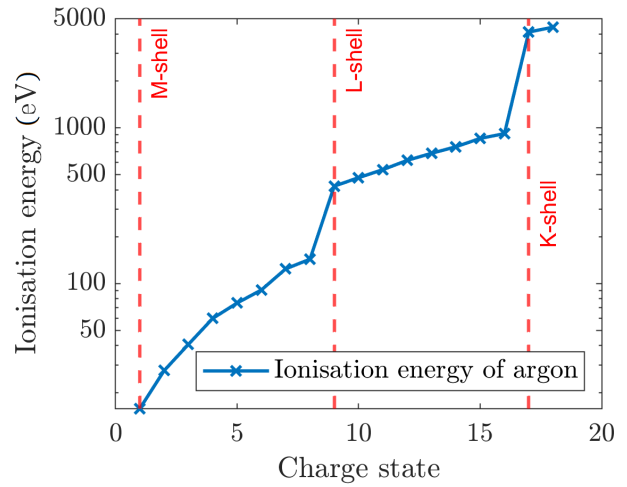
for these kinds of effects either the photon energy has to be increased significantly (from optical up to UV, XUV and X-ray regime), or the amount of photons, each with relatively low energy but large in number (high intensity), within a short period of time. Both parts will be further explained in the following section.

1.2. Lasers for high intensities or high photon energies

The uniqueness of laser light in terms of coherence, spectral bandwidth, intensity and the development and technical progress over the last decades in laser physics led to a wide range of possible uses for laser systems, such as medical applications, material processing, data transport and scientific research just to name a few. In the following, the focus will be on the techniques developed especially in terms of high-intensity and/or high photon energy, which is of relevance for this thesis.

High-Intensity optical laser

For scientific research, especially in our case for the study of ionisation processes in highly charged systems, one requires lasers which can provide high intensities and/or high photon energies. The intensity is defined as power per area, so energy per time and area

$$I = \frac{P}{A} = \frac{E}{tA}.$$ (1.2)

In order to maximize the intensity one has to increase the energy and/or decrease the time period in which the energy is released. The latter can be achieved by pulsed

laser systems. There are basically two techniques to create such laser pulses.

First, by use of a so-called 'Q-switch', which adjusts the quality of the resonator in such a way that the losses are kept high at the beginning, so the population inversion cannot be reduced by stimulated emission. Once the quality is increased at a certain time by the 'Q-switch', the population inversion can be reduced, so the energy is released within a short period, typically of the order of nanoseconds.

For even shorter pulses one uses the 'mode locking' technique, whereby the different longitudinal modes within the resonator are synchronised and phase matched with each other in a way that they interfere constructively. The more modes fit in the resonator the shorter the pulses will become. The spectral bandwidth of such a laser is preferred to be broad, so that a lot of modes can fit in the resonator simultaneously. This is for instance given for a titanium sapphire laser. Such systems can achieve pulse durations down to the order of several femtoseconds, however the energy per pulse is small, in the order of pico or nanojoule.

To increase the energy, an amplification has to be implemented. For instance the Nobel Prize awarded 'CPA(*Chirped Pulse Amplification*)-technique' is commonly used for that. It was devised by Donna Strickland and Gerard Mourou in 1985 [7]. It is based first on stretching the laser pulse in time, which reduces the energy density, second, an amplification of this stretched pulse, and finally a consecutive compression to increase the energy density again. A short and highly energetic pulse can thereby be created and intensities up to 10^{20} W/cm^2 can be achieved. Such high intensities, field strengths and photon fluxes compete with the intra-atomic forces and lead to various light-matter effects such as multiphoton-, above-threshold-, and tunneling-ionisation. So far the explained techniques are applied and valid for systems in the optical or at most near IR and UV regime, roughly $1 - 6$ eV photon energy.

Laser with high photon energy

If one wants to achieve higher photon energies, of the order of several tens or hundreds of electronvolts a new light source based on a different technique such as free-electron laser *FEL* is needed.

It was developed in the 1970s by John Madey [8] in Stanford. Free electrons are created by an electron source and are first accelerated up to relativistic velocities. Then they are transferred to an alternating magnetic field section called an undulator. A transverse motion due to the Lorentz force of the magnetic field is created and thereby synchrotron radiation is generated. A schematic of such an undulator section

is shown in figure (1.3).
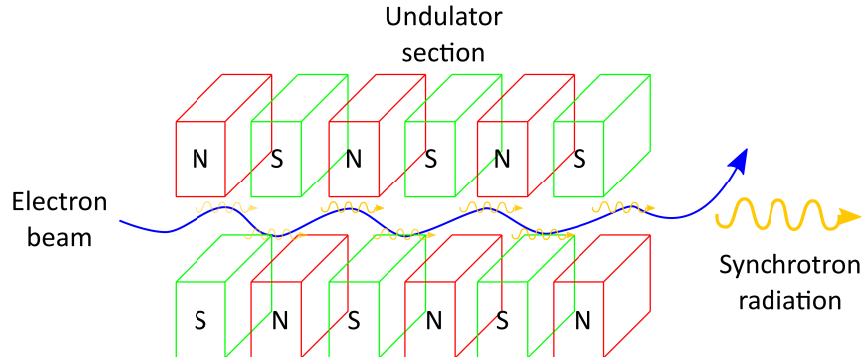
Figure 1.3.: Undulator section of a FEL. Accelerated free electrons entering an alternating magnetic field, called an undulator. Due to the Lorentz force a part of their motion is in the transverse direction of the beam direction. By that, synchrotron radiation is generated.

This radiation interacts with the electrons themselves and causes longitudinal bunching of the electrons into so-called microbunches, separated by one optical wavelength, whereby the emission is in phase and the light is coherent. In comparison to an optical laser, in which the laser medium causes the radiation, for a free-electron laser no such medium is required. So, no atomic transitions or states are involved at all. By that, the tunability of the photon energy is in principle not limited and high energies are available. For example FLASH @ DESY in Hamburg provides photon energies in the VUV or XUV regime $(10 - 300\,\text{eV})$, whereas European X-FEL located close to Hamburg operates in the X-ray regime $(0.26 - 25\,\text{keV})$. Another source of X-rays can be synchrotrons. Once charged particles, especially electrons, are forced on a curved trajectory they emit 'synchrotron radiation'. If the energy of the electrons is in the relativistic regime (typically GeV) the frequency of the emitted photons is shifted into the X-ray regime and the emission pattern has a narrow conical form leading to high photon flux in one direction, hence high 'brilliance'. In comparison to synchrotrons, the electron microbunches in an FEL emit photons in a coherent way and enhance previously emitted waves. The intensity without microbunching scales with the number of electrons $\propto N_e$, while with microbunching with $\propto N_e^2$, so a large amplification is achieved.

1.3. Penning traps: concept and current applications

A Penning trap is a device to store charged particles at a localized spot, basically at rest, for a certain period of time. The device is named after Frans M. Penning who in 1936 came up with the idea to add a magnetic field to improve the operation of vacuum gauges. Due to the cyclotron motion of charged particles within a magnetic field, their trajectory is extended in terms of distance they have to travel and by that the storage time within the volume is increased [9]. More detailed considerations were made by John R. Pierce in which he proposed a combination of a quadrupole electric field created by hyperbolic electrodes and an axial magnetic field in z direction to obtain a pure sinusoidal motion of trapped electrons [10]. The first device built in such a way was realised by Hans G. Dehmelt in 1959 for the storage of electrons. Together with colleagues he performed several spectroscopic measurements on stored ions in the following years [11, 12]. In 1989 he was awarded the Nobel Prize in physics together with Wolfgang Paul for the 'development of the ion trap technique'.

The basic principle of a Penning trap is the use of an electrostatic quadrupole field, superimposed with a homogeneous, static axial magnetic field to create a confinement volume for charged particles of all kinds, as shown in figure (1.4).
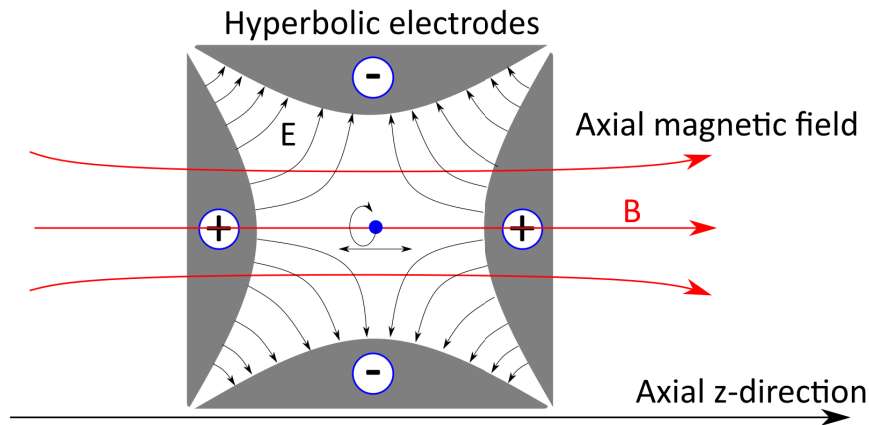
Figure 1.4.: Working principle of a Penning trap for a positively charged test-particle in blue. Hyperbolic shaped electrodes create an electrostatic quadrupole field for the confinement in axial z-direction, while an axial magnetic field prevents particle loss radially.

One of the key features of such traps is the possibility to store particles with a broad range of charge-over-mass ratios at the same time at the same place, while studying them basically at rest. The absence of rf-fields, which are used for example in Paul traps, prevents heating

effects of stored particles. Furthermore, techniques for non-destructive detection of the trapped particles, based on the pick-up and amplification of the induced image charges created by the particles' oscillation, allow a continuous analysis of the trap content [12]. With the same technique, a simultaneous cooling of the particles can be achieved as well [13, 14]. By attaching a resistance to a pick-up electrode, the image current is damped and the energy dissipation leads to a cooling of the particle motion - hence resistive cooling. For certain experimental conditions, a specific charge state is preferred to be the only one stored. Therefore a selection like the '*SWIFT*' technique (*Stored Waveform Inverse Fourier Transform*) can be used [15]. The frequency bands of all unwanted species are selected and by a Fourier transform into the time domain a transient signal is created. By irradiation, all the unwanted species become excited and lost. If a special shape or density of the ion cloud is needed, a way to manipulate the ions is required. There, for instance the 'Rotating wall' technique can be applied. It is a non-resonant excitation of the ensemble's rotation created by an additional rotating electric field [16].

Overall, the versatility of Penning traps in terms of confinement of single particles up to clouds of millions of particles, and storage time scales of the order of microseconds up to several months, together with various manipulation, detection, selection, and cooling techniques makes the Penning trap one of the most suitable devices for various different scientific questions. For instance the most precise measurement of fundamental constants, like proton and anti-proton masses or the magnetic moment of the electron, proton, anti-proton and positron have been performed in Penning traps specifically designed for that purpose [17, 18, 19]. By that, tests of quantum electrodynamics (QED) as well as charge, parity and time reversal (CPT)-symmetry have been performed.

As mentioned above, the specific design of a Penning trap depends on the experimental conditions and needs for the question of interest. In the frame of this thesis the aim is to study the interaction of highly charged ion ensembles under the influence of light at high intensities. The means of choice is the 'HILITE Penning trap'. *HILITE* is an acronym and stands for *High-Intensity Laser Ion Trap Experiment*.

Within the following chapters I will provide insight into the physical background, laser- as well as trap-wise, specifically related to the HILITE experiment and the current apparatus as it was designed, tested and set up first at GSI 'offline' without a laser, and for the first time 'in operation' at the FEL facility FLASH @ DESY. Finally, the results obtained and lessons learned during the beamtime will be presented.

2. Physics background and operation principles

In this chapter I will discuss the operation principle of our ion source and our charge state selection in general, followed by the concepts of several ion optical elements implemented and used in our setup in order to transport the ions from the source via a beamline to our Penning trap. A detailed description of the physics background of a Penning trap in general and specifically of the properties of our trap will be presented. In this context one of the key features of such traps, the non-destructive ion detection based on induced image charges and the implementation in our setup will be shown. In addition, another technique of non-destructive detection of bypassing ions will be presented. Finally the theoretical background of the processes involved in light-matter interactions in relation to high intensities or field strengths, relevant for the HILITE experiment will conclude the chapter.

2.1. Production and selection of highly charged ions

There are basically two options to produce highly charged ions for a Penning trap experiment. Either by an internal production process, called 'in-trap creation', or by an external source and a following consecutive extraction, transport, deceleration and capture process. There are advantages and disadvantages for both ways, like limitation in available particles species for 'in-trap' production, or the necessity of a defined capture process for externally produced ions. I will focus on the latter one, since it is the one used for the HILITE experiment.

2.1.1. Ion source - Electron Beam Ion Trap - EBIT

The ion source used for the HILITE experiment is a so-called *'Electron Beam Ion Trap*, or short and in the following just called - EBIT [20]. It is developed out of an *'Electron Beam Ion Source* - EBIS [21, 22] with an increased trapping time. The operation principle of both

2. Physics background and operation principles

are similar and based on electron impact ionisation [23]. A schematic depicted in figure (2.1 (a)) shows the basic concept. It is a rather simple form of ion production, in which either residual gas or a specific target gas is bombarded by electrons created by thermionic emission of a heated filament placed in the centre of a cathode. One requirement to be applicable is that the electron energy has to be at least equal to the ionisation potential of this charge state. Typically the beam energy is therefore optimized in order to produce the wanted target charge state. As a rule of thumb this is the case for an energy roughly 2-3 times larger than the ionisation potential of the charge state[24]. The created ions are trapped by an electrostatic potential, created by the 'drift tubes' $(1, 2$ and $3)$ along the confinement region in the axial direction, while the strong negative space charge created by the electron beam prevents them from escaping radially. This negative space charge potential of the electrons is shown in figure $(2.1(b))$.
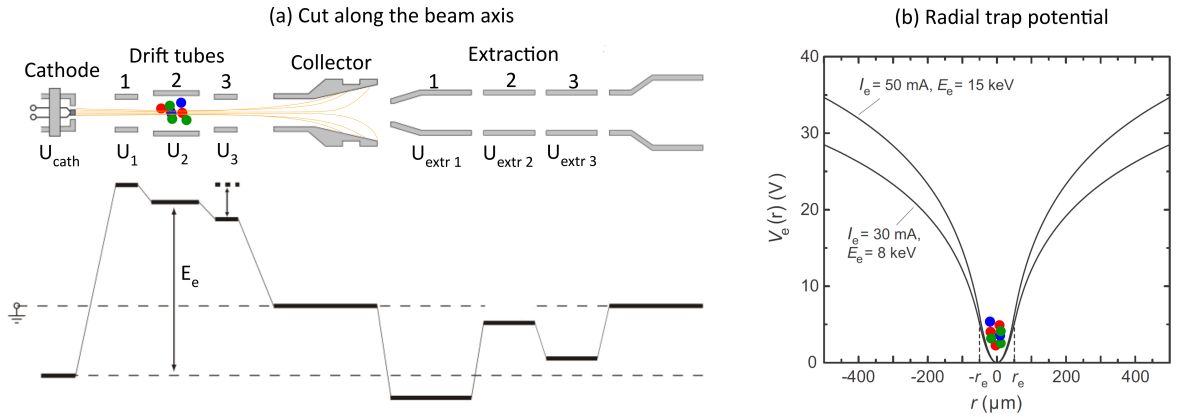
Figure 2.1.: Schematic of the operation principle of an EBIT. (a) Cut along the beam axis. Electrons (yellow) are created by the heated filament placed in the cathode and are accelerated towards the drift tubes (1,2,3). The superimposed magnetic field (not shown) compresses the electrons to maximize the overlap with the target gas. Higher charge states created by electron impact ionisation are extracted by lowering the last drift tube electrode (3) and guided by proper choice of the potential of the extraction electrodes. The electrons are repelled onto the collector. (b) Radial trap potential of an EBIT created by the space charge of the electron beam, shown for different electron energies and currents. From [25] - modified.

Depending on the charge state, there are several competing processes like charge exchange, radiative or dielectric recombination, which lower the charge state over time [26]. In order to produce higher charge states, the superposition between electron beam and target gas is extended in time, the so-called charge breeding time. The combination of electron current

12

density, breeding time and the charge-decreasing processes leads to an equilibrium state in which the ratio between the created charge states is constant. Once this is reached, the 'downstream' electrode of the drift tubes (3) responsible for the axial confinement is lowered and the created ions with a certain charge state distribution can leave the trap as a bunch, guided by proper electrostatic fields of the extraction electrodes. This operation mode is called 'pulsed mode'. The ion kinetic energy is in first order defined by the potential of the central drift tube $E_{kin} = q \cdot U_2$ and is in the range of several keV. The electrons are reflected towards a dedicated and water-cooled electrode, called 'collector', where they become absorbed. A typical extracted ion bunch consists of several different charge states, distributed around the wanted one. That's because of the competing processes of charge increasing and charge decreasing processes which are in an equilibrium state for fixed EBIT parameters like electron energy, background pressure and breeding time. The energy distribution ΔE of the ion bunch is given, as a rule of thumb, in the order of the trap depth, so the difference in potential height between the central drift tube and the outer drift tubes $\Delta E \approx U_{1,3} - U_2$ respectively.

2.1.2. Wien filter

The Wien filter, sometimes also called 'velocity filter' is a device to separate different velocity regimes within a charged particle beam and select a specific velocity which is transmitted. It uses a combination of an electrostatic field created by a plate capacitor, which is placed inside of a perpendicular, homogeneous magnetic field, see figure (2.2) [27]. Depending on the particle's kinetic energy, the magnetic field strength and the applied potential on the electrodes (U_+, U_-), a balance between the electrostatic force of the capacitor F_C and the Lorentz force F_L of the magnetic field leads to an undisturbed and straight motion of the particles with the wanted velocity v_0.

$$ F_C = F_L \qquad \Rightarrow \qquad q \cdot E = q \cdot v \cdot B \qquad \Rightarrow \qquad v = \frac{|E|}{|B|} = v_0 \qquad (2.1) $$

All the others will either be deflected too much or too little to be guided centrally on the axis, see figure (2.2). By that technique the inevitably created unwanted charge states of an extracted ion bunch from an EBIT (section 2.1.1) can be filtered out and the charge state of interest remains.
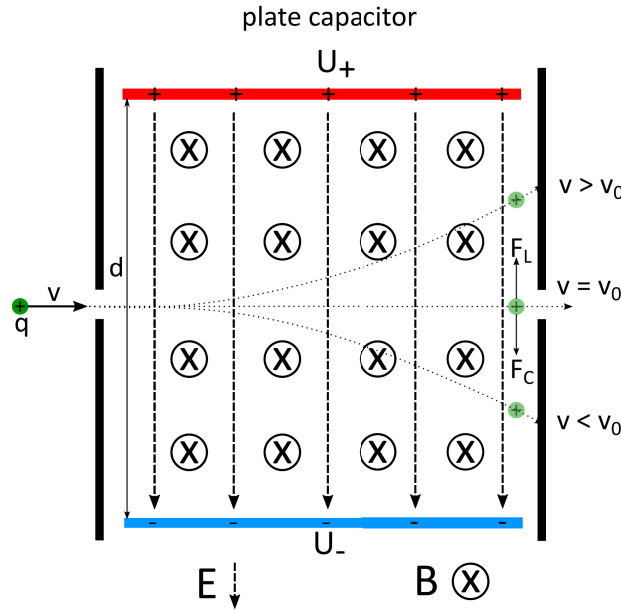
plate capacitor

Figure 2.2.: Schematic of the operation principle of a Wien filter. A plate capacitor with electrode distance d creates an electrostatic field E by applied voltages U_+ and U_- on the electrodes. It is placed perpendicular to a homogeneous magnetic field B. For a positively charged particle the transmission condition is fulfilled if the velocity is $v = v_0$, otherwise it will be either deflected up or downwards.

2.2. Ion transport: Ion optical devices used in HILITE

Once the ions of interest for a laser-ion interaction experiment have been produced and selected they have to be transported into the trap for preparation and investigation. Therefore, a low energy beamline, including several ion optical elements have to be implemented in order to deflect, steer, focus or decelerate the ions accordingly. The application of proper field configurations which are needed for an efficient transport are based on Coulomb and Lorentz-force for electric and magnetic fields. They are necessary for field calculations in order to simulate and estimate the behaviour of particles within the ion optical devices. A general description of the field equations, both time-dependent and time independent can be found in textbooks, like [28, 29] and will not be discussed further within this thesis.

Each accelerator, storage ring or beamline for charged particles requires ion optical elements in order to focus, deflect or just transport them efficiently from point 'A', for instance a source, towards 'B', a target or interaction region. The trajectory of charged particles can be altered by electric or magnetic fields. I will concentrate in this part on the general

functionality of the devices which are used in the current experimental setup, while the characterization of the like will be presented later on.

Einzel lens

The Einzel lens is one of the 'simplest' electrostatic ion optical elements. It consists typically of a bunch of hollow cylindrical electrodes, successively arranged along the beam axis z. A schematic representation can be seen in picture (2.3).
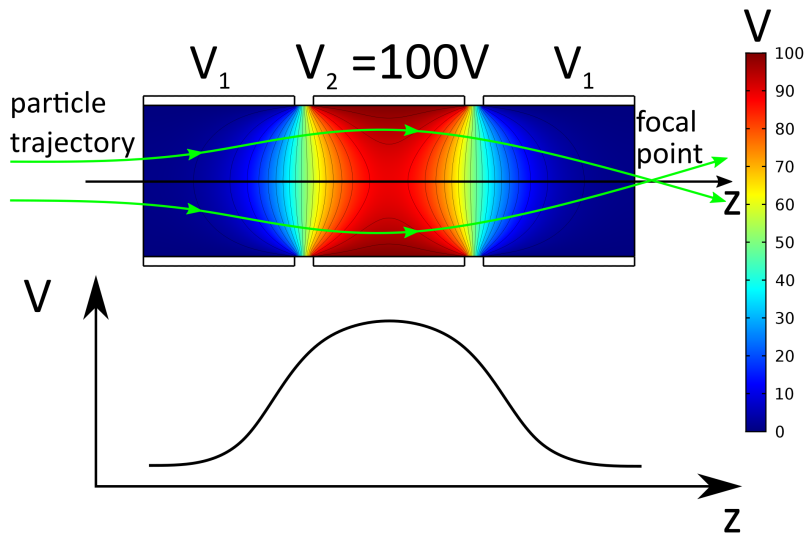
Figure 2.3.: Schematic of an Einzel lens with three consecutive electrodes and corresponding simulated electric potential as a function of position $V(z)$. The central electrode is on a higher potential $V_2 = 100V > V_1$ than the outer ones. The trajectory of charged particles is shown in green. The focal point can be shifted by adjusting the voltage on the central electrode.

The single electrodes are separated from each other by a small gap, allowing a different voltage to be applied. The polarity of those voltages is arbitrary, so it can be used for either low energy electron as well as ion beam applications. Having the same potential on both sides will not affect the energy of the particles after passing the device. Only the gradient between the central electrode and the outer ones will lead to a different energy of the particles while being inside. The ratio between the applied voltage on the central electrode V_2 and the particle's kinetic energy defines how the beam is affected. For instance, if the voltage reaches the kinetic energy of the particles a previously diverging beam can be made to converge.

Electrostatic 90°-deflection

Certain experimental setups require a change of the direction of the particle beam

for instance due to space restrictions or charge separation purposes. The direction of such a beam can be altered either by a magnetic field or an electrostatic field perpendicular to flight direction. In the low-energetic regime most often electrostatic devices, called 'deflectors' are used. More details about the development as well as advantages and disadvantages of several types of deflectors can be found in [30]. In our case, the decision was made to use an electrostatic radial cylindrical analyser [30, 31]. A schematic, depicted in figure (2.4) shows the basic principle.
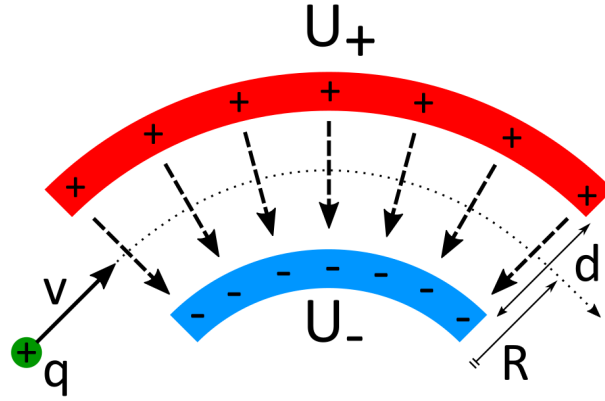
Figure 2.4.: Schematic of a radial cylindrical analyser. An applied voltage difference between the two bent electrodes leads to an electric field component towards the centre, hence perpendicular to the initial particles velocity v. A deflection inwards takes therefore place.

A potential difference $U_D = (U_+ - U_-)$ applied between the two bent electrodes at a distance d leads to an electric field $E = U_D/d$ perpendicular to the flight direction of the particles, hence their trajectory is changed. As a rule of thumb, the applied voltage has to be around a quarter of the particles' kinetic energy. The exact voltage needed for a particle on axis to be deflected can easily be calculated by considering that the force created by the electric field needs to be equal to the centripetal force, given by

$$F_{CP} = m \cdot \frac{v^2}{R} = q \cdot E \qquad \Rightarrow \qquad E = \frac{2 \cdot E_{kin}}{q \cdot R}, \tag{2.2}$$

with the particles' kinetic energy $E_{kin} = (m/2)v^2$ in the non-relativistic approximation, the charge of the particle q an the radius R of the particle trajectory. Together with the voltage difference U_D one gets

$$U_D = \frac{2 \cdot E_{kin} \cdot d}{q \cdot R}. \tag{2.3}$$

This relation tells, which voltage has to be applied at the bender electrodes in order to deflect particles on axis with charge q and kinetic energy E_{kin} for a certain bender geometry d, R respectively.

Pulsed drift tube - PDT

The pulsed drift tube, in the following just called PDT, is a conceptionally rather simple device to decelerate charged particles. It consists basically of an elongated, conducting tube as depicted in figure (2.5). Further, it requires a bunched beam to operate and works best if the spatial distribution of the bunch fits completely inside the tube. The electrode is set first on a high positive voltage, such that a bunch of positively charged particles becomes decelerated when entering the tube. While inside, the voltage is switched to a negative potential by a fast switch (around $3\,\mathrm{kV/\mu s}$). Therefore the particles become decelerated a second time while leaving the tube. Since the deceleration in axial direction leads to an acceleration in the radial direction [32] (conservation of phase space), it is appropriate to operate such a device in the vicinity of an axial magnetic field forcing the particles onto a cyclotron orbit, to minimize radial expansion. In case of a Penning trap, this results in a location close to the trap electrodes inside the magnet bore.

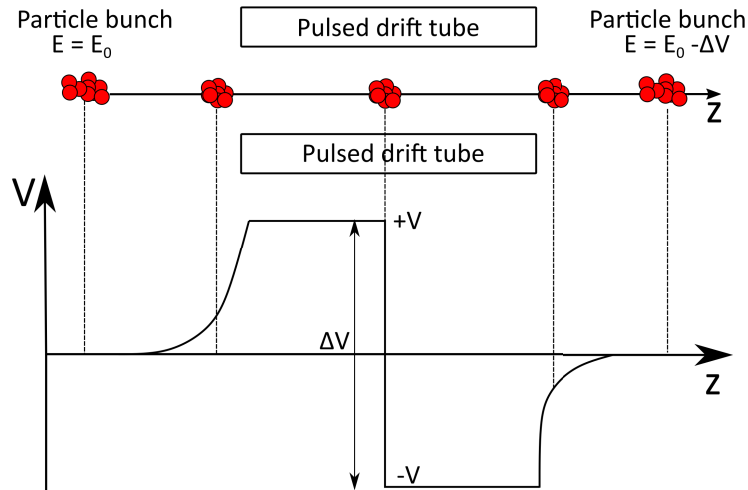Figure 2.5.: Operation principle of a PDT for positively charged particles. An ion bunch approaches the PDT electrodes and is decelerated due to the applied voltage (+V). While inside, the polarity of the voltage is changed (-V) by a fast switch. By doing so, the bunch is further decelerated while leaving the PDT.

The successful implementation and operation within a Penning trap experiment has

been shown for instance in [33].

2.3. The Penning trap

As briefly described in section (1.3), the confinement of charged particles in a Penning trap is realised by a superposition of a homogenous, strong magnetostatic field $\boldsymbol{B}$ and an electrostatic field $\boldsymbol{E}$.

2.3.1. Types and field configurations of Penning traps

The orientation of the magnetic field is along the trap axis (typically z-axis) $\boldsymbol{B} = (0, 0, B_0)$, whereas the electric field can be expressed as $\boldsymbol{E} = -\boldsymbol{\nabla}\Phi$ created by a quadrupolar potential Φ. It can typically be described by Cartesian coordinates in the form of

$$\Phi = \frac{U_0}{2d^2} \cdot (2z^2 - x^2 - y^2) \tag{2.4}$$

with U_0 being the applied voltage between the ring and the endcap electrodes and the so-called 'characteristic trap size' d, a specific value depending on the trap geometry, given by [32]

$$d^2 = \frac{1}{2}\left(z_0^2 + \frac{\rho_0^2}{2}\right). \tag{2.5}$$

z_0 is the distance of each endcap electrode to the trap centre, while ρ_0 describes the inner radius of the central ring electrode, see figure (2.6 (a)). This potential represents a harmonic potential along the z-axis and therefore the particles' axial oscillation frequency within the potential well is independent of the oscillation amplitude [34]. By geometry, a set of hyperbolic electrodes produces a quadrupolar potential, although it suffers from the lack of both mechanical and optical accessibility, as shown in (2.6 (a)). Inserting holes or slits to bypass will introduce perturbations to the electric potential and hence lead to anharmonicities, together with the challenge of precise manufacturing of hyperbolic-shaped electrodes [35, 36].

In general, close to the trap centre, the electrostatic potential Φ of a Penning trap can be expressed in terms of an expansion [34] in spherical coordinates by

$$\Phi = \frac{1}{2}U_0 \sum_{k=0}^{\infty} C_k \left(\frac{r}{d}\right)^k P_k(\cos\theta). \tag{2.6}$$

Here, U_0 is the trapping potential as explained above, $r = \sqrt{\rho^2 + z^2}$ the distance to the trap centre, d the trap size given by equation (2.5) and $P_k(\cos\theta)$ the Legendre polynomials of the k-th degree, with the argument $\cos\theta = z/r$. Due to symmetry only the even coefficients have non-zero values and hence contribute. The coefficient C_0 is an overall potential offset, and therefore not important for the particles' motion. C_2 represents the quadrupole term and would be the only non-zero factor for an ideal quadrupole trap, as can be seen by considering C_2 in (2.6) only, reduces to (2.4). The following C_4 and C_6 coefficients describe the 'anharmonicity', i.e. the imperfection of the electrostatic field of a 'real' trap in terms of imperfections of the manufacturing process or misalignment of the setup and hence have to be 'compensated'. C_6 is suppressed by $(r/d)^2$ in comparison to C_4 and can mostly be neglected for particles with small kinetic energies [32].
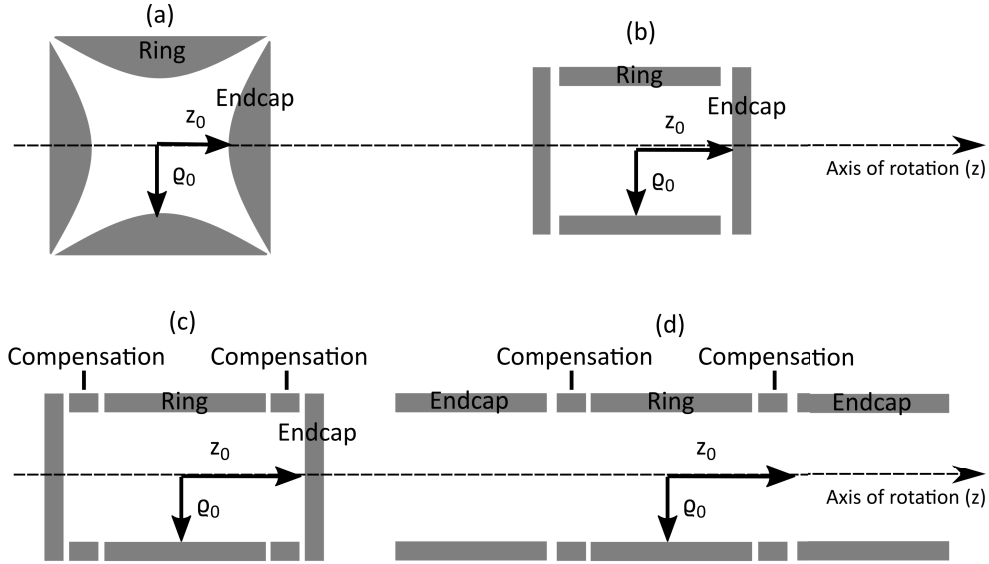
Figure 2.6.: Cross-section view of different types of Penning traps. (a) Hyperbolically shaped electrodes. 'Perfect' harmonic field configuration, but almost no optical and mechanical access. Difficult to produce to high precision. (b) Trap mechanically compensated by appropriate ρ_0/z_0 ratio. Easy to produce, but still no access possible. (c) Trap electrically compensated by dedicated compensation electrodes. Easy to produce, harmonicity in the centre can be 'tuned', but no access. (d) Open-endcap trap electrically compensated. Easy to produce, allows access to the trap centre, but harmonicity is obtained by the cost of larger geometric size.

As mentioned above, hyperbolic electrodes, although providing good confinement properties by design, limit the access of particles or laser beams. A more open structure is needed, and so the design of cylindrical electrodes was pushed forward [34]. For instance one can use a

central cylindrical ring electrode with two flat endcap electrodes, as depicted in (2.6 (b)). The gained access however led to a non-harmonic confinement potential which has to be compensated. By appropriate choice of the parameters, $\rho_0 \approx 1.203 z_0$ one can compensate the inherent anharmonicity created by the cylindrical shape. This is then called 'mechanical compensation' [37]. In order to realise an optical and/or mechanical access to the trap centre the flat endcap electrodes have to be replaced by cylindrical ones, see figure (2.6 (d)). Therefore the length has to be adapted/elongated ($z_E > 3\rho_0$) to compensate for the introduced anharmonicities. For even further improved access, conical electrodes allow access of laser beams with rather large solid angles. Such a system is used in our setup and the properties are describe and summarized in [38]. More details about various different designs and Penning traps in general can be found in [32].

For the HILITE experiment, the overall design idea was to set up a trap which allows access to a broad range of high-intensity and high-energy laser systems, some of which can be focussed very tightly, while others cannot. In addition the system should be rather robust, since it is supposed to be transported to those facilities. Therefore, we decided to combine several of those concepts to design and build such a trap. It is a mechanically compensated Penning trap with conical capture electrodes. Figure (2.7) gives an overview of the specific design of the trap electrodes for this experiment.

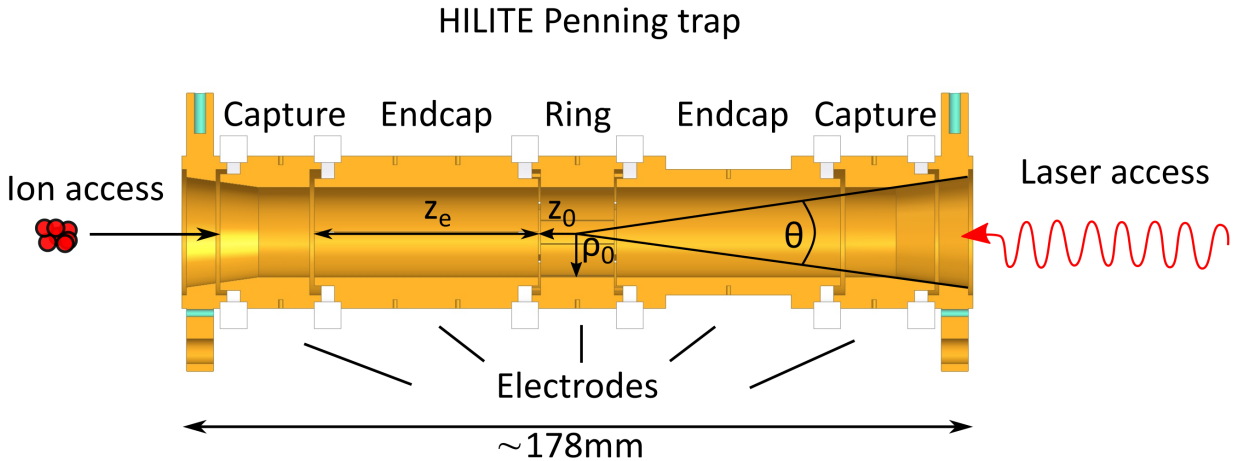Figure 2.7.: Schematic of the HILITE Penning trap. Cylindrical electrodes with conical openings at both sides to increase the laser and ion acceptance.

The challenge of this approach is to combine the conditions needed for the trap-part like ion production, selection, transport, deceleration, capture, storage and preparation, while not restricting at the same time the conditions given by the laser. This becomes even more

challenging because of the huge span of different operation parameters for different laser systems in terms of laser energy, repetition rate of the pulses and so on. Although the development of laser systems over the last decades was tremendous, the requirements of high intensities and/or high field strengths are huge, such that the systems of interest are mainly fairly large facilities. Hence, a system had to be set up which is flexible in terms of operation as well as transportable to be able to go to those various facilities and perform the experiments on site. The geometric and electrical characteristics are given in table (2.1).

Table 2.1.: HILITE Penning trap properties

ρ_0 (mm)	z_0 (mm)	z_e (mm)	d (mm)	θ (°)	C_2	C_4
10	8.7	50	7.9275	16	0.59567	0.00365

2.3.2. Single-particle motion

A single particle of charge q and mass m moving inside a Penning trap with a field configuration as described in section (2.3.1), i.e. a homogeneous magnetic field along the trap axis $\boldsymbol{B} = (0, 0, B_0)$ and an electrostatic quadrupole field $\boldsymbol{E} = -\boldsymbol{\nabla}\Phi$ derived from the potential (2.4), will experience the Lorentz force [39].

This leads to two coupled equations of motion in the radial (x, y)-plane and one independent equation of motion in the axial z-direction [32]

$$\ddot{x} = \omega_c\dot{y} + \frac{\omega_z^2}{2}x \qquad ; \qquad \ddot{y} = -\omega_c\dot{x} + \frac{\omega_z^2}{2}y \qquad ; \qquad \ddot{z} = -\omega_z^2 z, \qquad (2.7)$$

with the axial oscillation frequency due to the electric potential

$$\omega_z = \sqrt{\frac{q\Phi}{md^2}} = \sqrt{\frac{qU_0C_2}{md^2}} \qquad (2.8)$$

and the cyclotron oscillation frequency due to the magnetic field

$$\omega_c = \frac{qB_0}{m}. \qquad (2.9)$$

However combining both, the electric and magnetic field will lead to a deviation of the so-called 'free particle' cyclotron frequency ω_c to

$$\omega_\pm = \frac{\omega_c}{2} \pm \sqrt{\frac{\omega_c^2}{4} - \frac{\omega_z^2}{2}} \tag{2.10}$$

with ω_+ being the 'modified cyclotron frequency' and ω_- the magnetron frequency due to $\boldsymbol{E} \times \boldsymbol{B}$ drift, respectively.

Assuming a trap voltage between the ring and the endcap electrodes of $U_0 = 50\text{V}$ and a magnetic field of $B_0 = 3\text{T}$, the three motional oscillation frequencies for stored carbon ions within the HILITE Penning trap can be calculated by equation (2.8) and (2.10). The corresponding results are given in table (2.2).

Table 2.2.: Motional frequencies for carbon ions in the HILITE Penning trap for $U_0 = 50\text{V}$, $B_0 = 3\text{T}$ and given trap parameters from table (2.1)

Ion species	ω_z (kHz)	ω_+ (MHz)	ω_- (kHz)	ω_c (MHz)
C^{1+}	$2\pi\times310.7$	$2\pi\times3.827$	$2\pi\times12.613$	$2\pi\times3.838$
C^{2+}	$2\pi\times439.4$	$2\pi\times7.666$	$2\pi\times12.592$	$2\pi\times7.678$
C^{3+}	$2\pi\times538.1$	$2\pi\times11.51$	$2\pi\times12.585$	$2\pi\times11.52$
C^{4+}	$2\pi\times621.4$	$2\pi\times15.34$	$2\pi\times12.581$	$2\pi\times15.36$
C^{5+}	$2\pi\times694.7$	$2\pi\times19.18$	$2\pi\times12.579$	$2\pi\times19.20$
C^{6+}	$2\pi\times761.0$	$2\pi\times23.02$	$2\pi\times12.578$	$2\pi\times23.04$

2.3.3. Particle ensembles

Yet, the considerations and calculations made assumed confined single particles. For laser-ion interactions with small cross sections a particle ensemble with a high density would therefore be preferred. However, the introduction of many charged particles necessitates the description in terms of a plasma, which leads to a variety of effects which have to be considered [32].

Description of a particle ensemble in terms of a non-neutral plasma

A confined particle ensemble in a Penning trap can be considered as a non-neutral plasma. The particle-particle distance within such a plasma can be described by the Debye length,

given by

$$\lambda_D = \sqrt{\frac{\epsilon_0 k_B T}{2nq^2}} \tag{2.11}$$

with ϵ_0 being the permittivity of free space and n the particle number density. In a dense plasma, which is the case if the dimensions of the ensemble are smaller than the Debye length, the particles are influenced by their neighbours via the Coulomb force, hence a single-particle approach breaks down and the description in terms of a plasma becomes feasible. A quantity to describe the amount of correlation within a plasma is the so-called plasma parameter Γ_P defined by [40]

$$\Gamma_P \equiv \frac{q^2}{4\pi\epsilon_0 a_{WS} k_B T} \tag{2.12}$$

with a_{WS} being the effective ion-ion distance for a given plasma density n [41]. Depending on this parameter one speaks of a weakly (gas-like state) correlated plasma for $\Gamma_P \ll 1$ and of a strongly correlated plasma for $\Gamma_P > 1$. For the latter case one distinguishes further between a fluid-like state for $2 < \Gamma_P < 174$ and a crystal-like state for $\Gamma_P > 174$. From equation (2.12) follows that a cooling process of the particles leads to an increase in density, since the distance Γ_P between the particles decreases. Typical ion-ion distances are around $10\,\mu\text{m}$ and together with B_0^2-dependency of the density lead to values of $10^9\,1/\text{cm}^3$ in the current case.

2.3.4. Excitation and manipulation of particle motions

Most Penning trap experiments require a defined, well-controlled particle ensemble or single particles within a specific state, like charge or energy in order to investigate certain properties. In experiments with a pure ion cloud the ensemble has to be cleaned, so that only the charge state of interest remains, or the density/shape of the ensemble has to be varied. This can be achieved by application of appropriate electromagnetic excitation. This can be done either resonantly by addressing the respective motional frequency as well as non-resonantly to force specific particle motions.

The most common types are dipole and quadrupole excitations, this is why most Penning trap designs rely on split electrodes, like 4-fold, or 8-fold segmented ring electrodes and 2-fold segmented endcap electrodes as shown in figure (2.8) for the HILITE Penning trap electrodes.
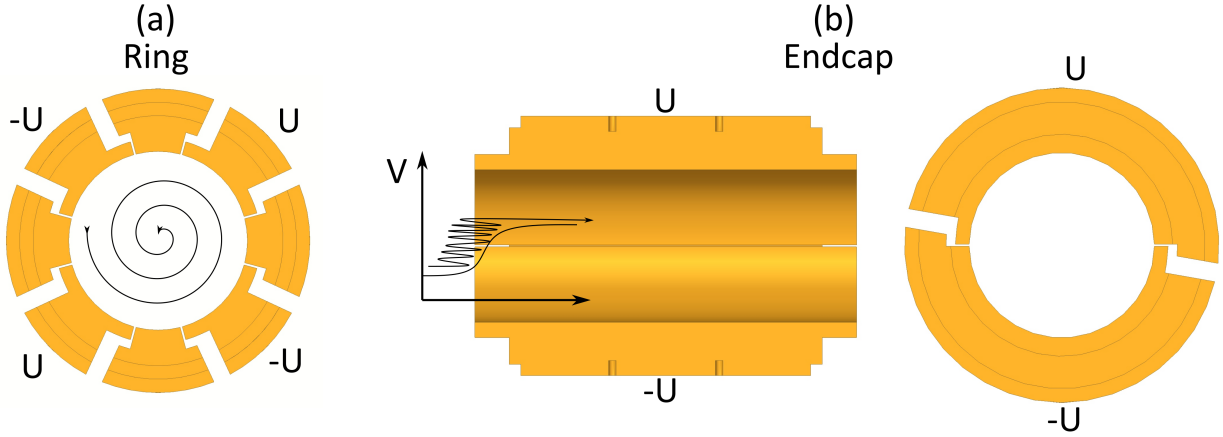
Figure 2.8.: Schematic of split trap electrodes of HILITE for particle excitation. (a) 8-fold segmented ring electrode for radial quadrupole excitation - for instance magnetron centring as depicted by the spiral trajectory. (b) 2-fold segmented endcap electrode for axial excitation - for instance removing of unwanted particle species as shown by the energy increase within the potential well until they overcome the potential barrier.

Dipole excitation of the particle motion

The main purpose of dipole particle excitation is the 'cleaning' of the trap content of all unwanted species. The general operation principle, both resonant and non-resonant, as well as for the axial and radial motions is the same. The particles' motional amplitude is excited until they exceed the confinement region and are lost. The energy needed to increase the amplitude in the axial motion scales with $E_z \propto qU_0$, while for the radial motion it scales with $E_R \propto q^2 B_0 R^2$, in which R is the radius where the confinement is lost. It becomes obvious that the axial motion is much easier to excite and requires less transferred power. The common ways are [32]

- narrow-band excitation of the individual unwanted oscillation frequencies

- broadband irradiation of white noise with a gap (notch filter) for the wanted species

- signal transient, which is the Fourier transform of all the corresponding unwanted species, called **SWIFT** - $\underline{S}$*tored* $\underline{W}$*aveform* $\underline{I}$*nverse* $\underline{F}$*ourier* $\underline{T}$*ransform* [15, 42]

which all rely first on the definition of the frequency bands. A schematic of the different techniques is depicted in figure (2.9).
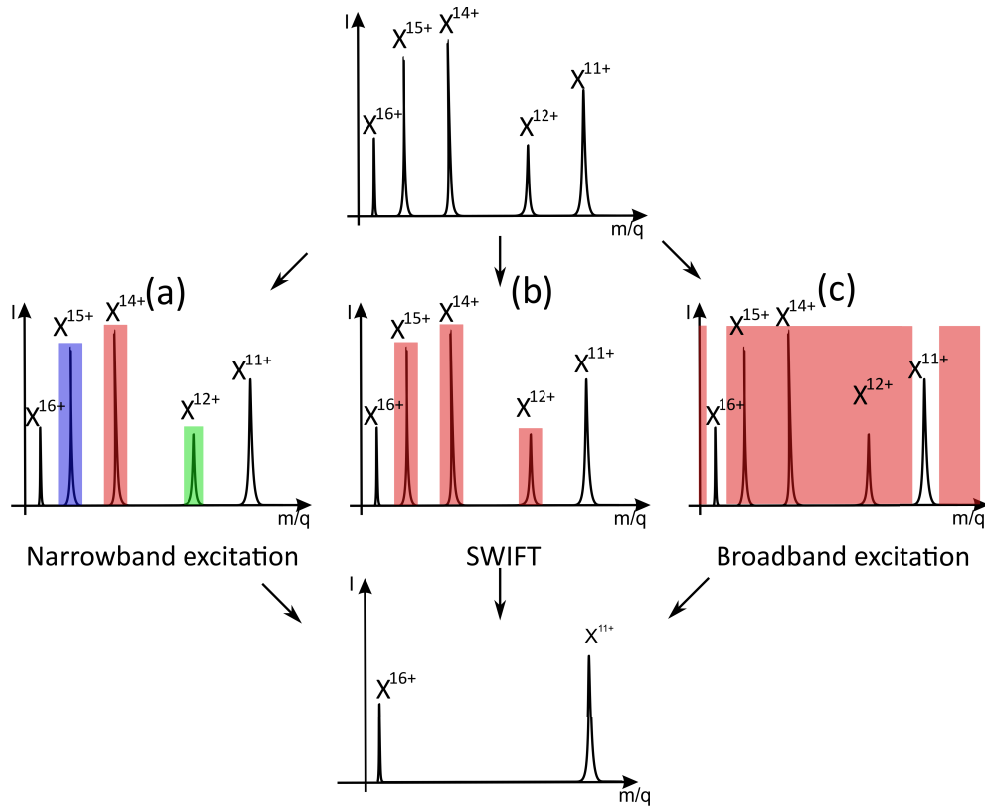
Figure 2.9.: Different excitation schemes to remove unwanted particle species. (top) Starting point with a particle ensemble of different charge states. (a) Narrow-band excitation of the unwanted species and sequential excitation. (b) SWIFT excitation. All the frequency bands are irradiated simultaneously by a FFT transient signal. (c) Broadband excitation with gaps ('notch filter') at the frequencies which should be kept. (bottom) 'Cleaned' particle ensemble.

2.3.5. Cooling of the particle motion

The trajectory of stored particles in a Penning trap as shown in (2.3.2) is described by three individual motions, axial, reduced cyclotron and magnetron motion with corresponding oscillation frequencies given by the equations (2.8, 2.10). Hence particle cooling for the axial and reduced cyclotron motions always refers to the reduction of the particles' energy and therefore a decrease of the motional amplitude. This is desired, since it leads to higher particle density and better localizability at the trap centre and hence improves the possibility for particle manipulation. For an ideal trap the individual motions are independent, therefore different temperatures can be assigned to the motions and they can be cooled and excited individually as well. Although the concept of temperature is basically

not applicable for single, or a small number of particles it can be given a meaning under certain circumstances [43]. If the particles are in thermal equilibrium with an infinitely large heat bath and the motional energy is measured repeatedly, the probability follows a Boltzmann distribution which assigns a certain temperature.

The Penning trap concept offers a lot of different cooling techniques. The most common ones are laser [44] and resistive cooling [14] from which I will present only the latter one in detail because it is used at HILITE.

Feedback cooling/slowing

Each cooling method has a certain efficiency depending mainly on the energy regime of the stored particles. Since for HILITE the ions are externally produced as a bunch and have to be captured first in the trap, their initial kinetic energy is fairly large ($\approx 5 - 10\,\mathrm{eV/q}$), hence a mechanism is needed to decrease first their motional amplitude in order for an efficient resistive cooling to be applicable. This can be achieved by the so-called 'feedback cooling' or 'slowing'. It is a technique which originates from storage ring physics (known there as stochastic cooling) to cool down a particle beam. A bunched structure or a motion of the centre of charge is needed, since cooling in this sense aims for reduction of the size and energy spread of the beam, while not being accompanied by beam loss [45]. It is based on the electronic pick-up of an image charge, created by an oscillating particle in the ring. By an amplification of this signal, a correction signal on a different electrode further 'downstream' can be applied in order to correct either the displacement or energy of the particle.

This technique can be adapted and applied to cool the particle's motion in a Penning trap [46]. The oscillating particles in the trap induce as well an image charge in the detection (pick-up) electrodes. As long as the bunch structure of the particles is preserved, the picked-up signal becomes phase-shifted by 180°, amplified and applied back onto an assigned electrode. By that, the particles' motion itself produces a counter-force damping the amplitude of the motion of the centre of charge. This technique was successfully demonstrated and used already in a Penning trap [47]. A more detailed description of the implementation at HILITE is given in [48].

Resistive Cooling

The working principle of resistive cooling is based on the damping (power dissipation) of induced image currents in an attached resonance (RLC-)circuit, created by charged particles

moving in the vicinity of an electrode. This current leads to a time-dependant voltage signal in the circuit which can be used for particle detection. Therefore the process of particle cooling by resistive cooling and (resonant) detection of the particles come along with each other and are basically equivalent. In the following, the focus will be on the cooling part of this process, while the detection will be described in detail in section (2.4.2).

A particle with charge q at distance $\boldsymbol{r}$ to a conductive surface will induce there a surface charge density $\sigma(\boldsymbol{r})$. By assuming this surface being an electrode and using Gauss' law, the total induced charge can now be calculated by integration over its surface

$$q_{ind} = \oiint\limits_{A} \sigma(\boldsymbol{r})\mathrm{d}A = -q \cdot \Xi(\boldsymbol{r}). \tag{2.13}$$

The geometry function $\Xi(\boldsymbol{r})$ describes the fraction of the original charge being induced, taking the shape of the pick-up electrode and the position of the particle into account, and obeying the condition $0 \leq \Xi(\boldsymbol{r}) \leq 1$. It is equivalent to the so-called 'weighting potential' Φ, introduced by Shockley and Ramo in their theorem [13, 49] which describes the amount of induced image current by a moving charged particle in the vicinity of a conducting surface and given by

$$I_P = \frac{\mathrm{d}q_{int}}{\mathrm{d}t} = \frac{\mathrm{d}q_{int}}{\mathrm{d}z}\frac{\mathrm{d}z}{\mathrm{d}t} = -q(\nabla_z \Phi)\dot{z} = qE_\Phi \dot{z} \tag{2.14}$$

in which $\dot{z}$ is the velocity of the charged particles (here in z-direction) and $E_\Phi = \nabla_z \Phi$ the so-called 'weighting field' [49]. By attaching a resistor to the pick-up electrode, the image current induced by the oscillation of the particle is damped in the form of heat within the resistor. The amplitude of the oscillation is therefore reduced and hence the particles' motion is cooled. This technique works for both the axial and reduced cyclotron motion, while the magnetron motion has to be 'cooled' indirectly, for instance by motional coupling (2.3.4) of the two radial motions, so that the energy is first transferred to the cyclotron motion and then cooled there directly.

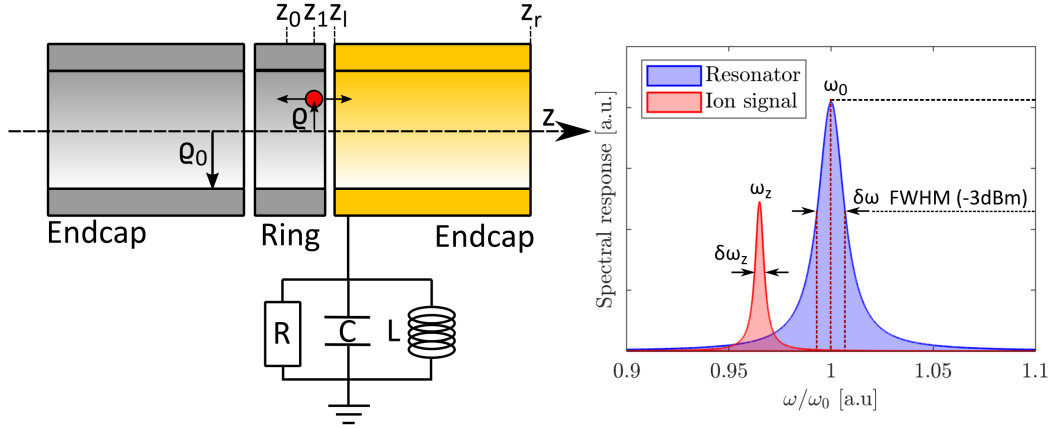## 2. Physics background and operation principles

Figure 2.10.: Schematic representation of resistive cooling. The motion of a charged particle induces an image charge in the pick-up electrode (yellow endcap). By attaching a tuned resonance (RLC-) circuit to the electrode the image current is damped within the circuit and hence the particle motion is cooled. A response of such an RLC circuit together with an ion signal is shown on the right hand side.

The experimental realization is typically done by a resonance circuit that is connected to the pickup electrode. Its resonance frequency is tuned onto the oscillation frequency of the corresponding particle motion ($\omega_0 = \omega_i$, while $i = z, +$). In resonance at frequency $\omega_0 = 1/\sqrt{LC}$ the impedance of that circuit is purely real with a resistance given by

$$R = QL\omega_0, \tag{2.15}$$

where Q describes the quality factor of the circuit and L its inductance. For any resonator circuit, Q is defined as the ratio between the stored energy and energy loss per angular cycle $Q = \omega_0/\delta\omega$ and can be obtained by measuring the frequency width $\delta\omega$ at the position of the -3 dBm frequency amplitude of the resonance [50, 51] as shown in figure (2.10). The power dissipation via the resistor reads as $P(t) = RI_P^2(t)$ with R being the effective resistance of the attached circuit and $I_P(t)$ the current induced by the charged particle. The damping can be modelled in terms of a frictional force $F_{damp} = -\gamma\dot{z}$, resulting in an exponential behaviour of the ion cooling $E_z(t) = E_z(t = 0)\exp(-\gamma t)$ with γ being the damping constant of the system. The cooling time constant for the axial motion of a single charged particle is therefore given by

$$\tau_z = \gamma^{-1} = \frac{D^2}{R}\frac{m}{q^2}, \tag{2.16}$$

with the effective electrode distance D, which basically describes the geometry of the pick-up electrode seen at the particles' position [52]. The final temperature which can be achieved by resistive cooling is typically limited by the temperature of the resonance circuit in general and specifically by the electronic thermal noise, called 'Johnson noise' within the frequency bandwidth $\delta\omega$ of interest [53]. It induces a voltage across the resistance R of the circuit and can be estimated by

$$U_T^2 = 4k_B T R \delta\omega. \tag{2.17}$$

Although in case of an ion ensemble, further effects like particle-particle interactions have to be incorporated which require a more complex approach in terms of simulations [54], the overall behaviour is similar and follows the same principles as in the single particle approach. For non-correlated phases of the stored ion ensemble, as is usually the case, the cooling time constant reads exactly as the single-particle case [32] and is therefore given by (2.16). In all cases, whether a single particle or a particle ensemble, a high resistance and therefore a high damping is needed to decrease the cooling time. From equation (2.15) one can see that this requires a high Q-value of the resonance circuit. On the other hand, a high Q-value results in a narrow resonance frequency as shown in figure (2.10) and limits the number of particles being simultaneously in resonance due to their frequency distribution.

2.4. Non-destructive ion detection

The possibility to detect and characterize confined particles in a non-destructive way is one of the most important features a Penning trap provides. It can be distinguished for the HILITE experiment between a non-resonant (single-pass) technique and a resonant technique with tuned resonance circuits to perform frequency measurements of the trap content. Common to both is the basic concept of operation in terms of detection and amplification of induced image charges in dedicated pick-up electrodes, as it was introduced already in section (2.3.5).

2.4.1. Non-resonant detection

One of the non-destructive detection devices within HILITE is a charge counter, which allows the detection and determination of the ion number and structure of the ion bunch. Due to the single-pass behaviour of each ion bunch this is a non-resonant scheme and therefore the counterpart to a resonant Schottky mass spectrometry in which the revolution

of an ion bunch in a storage ring is detected [55]. Nevertheless the overall concept is the same, although the single-pass character poses a challenge in terms of detectability, hence a high detection sensitivity and low noise (electronic-wise) is required.

The induced charge q_{in} in the detection electrode is converted into a voltage signal U_{in} by

$$U_{in} = \frac{q_{in}}{C_{tot}} \overset{2.13}{=} \frac{-q \cdot \Xi(\boldsymbol{r})}{C_{tot}} \tag{2.18}$$

with C_{tot} being the total capacitance of the detection system, including amplifiers, cables etc. and the induced charge q_{in} as defined in (2.13). The voltage signal from a single-pass event is typically too small to be directly read out, so an amplification is generally needed. This is done via a two-stage amplification system as can be seen in figure (2.11).
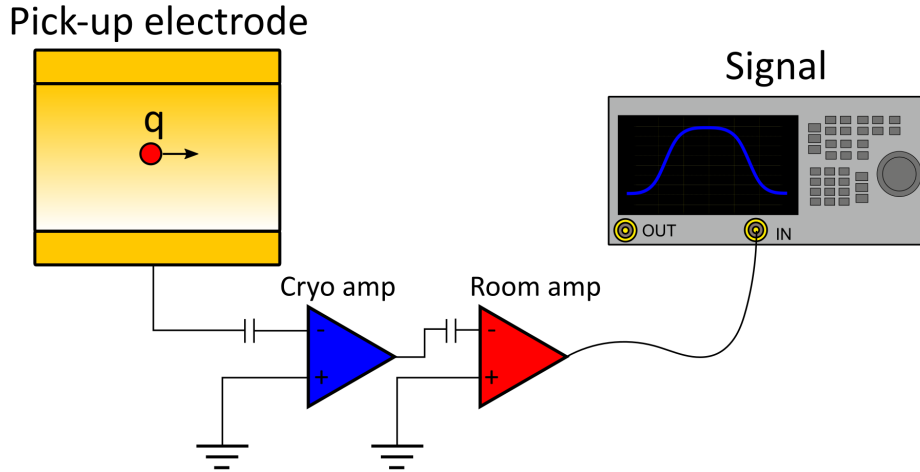
Figure 2.11.: Detection scheme of a single-pass charge counter. A bypassing charged particle induces a fraction of its charge in the pick-up electrode. This image charge is converted into a voltage signal and amplified in a two-stage process. The time-dependent signal is then read out on an oscilloscope.

One is placed close to the pick-up electrode in a cryogenic environment, and a second one outside at room temperature. The gain in signal they provide can be described by the amplification factor α. The output signal voltage of the detection system reads then [56]

$$U_{sig} = -\frac{\alpha}{C_{tot}} q_{in} \cdot \Xi(\boldsymbol{r}) = S q_{in} \cdot \Xi(\boldsymbol{r}) \tag{2.19}$$

with $S = -\alpha/C_{tot}$ being introduced as the sensitivity of system. The induced charge for an ion bunch consisting of N particles with charge q reads therefore as the sum over all

individual particles

$$U_{sig} = -\frac{\alpha}{C_{tot}} \sum_{i=0}^{N} q_{in}^i \cdot \Xi(\boldsymbol{r_i}) = S \sum_{i=0}^{N} q_{in}^i \cdot \Xi(\boldsymbol{r_i}). \tag{2.20}$$

It becomes obvious that in order to optimize the signal strength, the sensitivity S has to be maximized. This can be achieved by a reduction of the total capacitance C_{tot}, for instance short cables, small input capacitances of the amplifiers, and small capacitances of the pick-up electrode, as well as increasing the amplification α by low-noise amplification stages and cryogenic environments.

In order to be able to analyse a signal received from such a detector and determine important properties like particle number, kinetic energy or bunch length some parameters have to be introduced to characterize the signal shape. This is shown in figure (2.12).
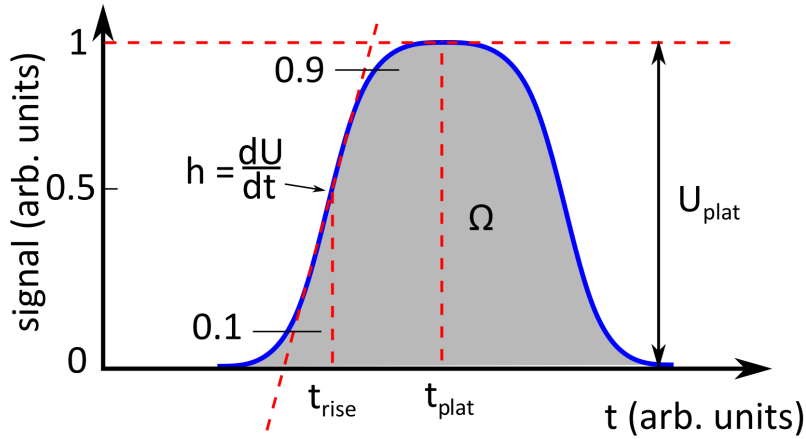
Figure 2.12.: Charge counter signal and corresponding parameters needed for evaluation. The plateau voltage U_{plat}, the area below the signal curve Ω and the slope of the signal h.

The parameters are the plateau voltage U_{plat}, the slope of the signal h and the area Ω below the signal curve [57]. They are given by

$$U_{plat} = U_{sig}(t_{plat}), \qquad h = \frac{\mathrm{d}U_{sig}(t_{rise})}{\mathrm{d}t} \qquad \text{and} \qquad \Omega = \int U_{sig}(t)\mathrm{d}t.$$

The number of particles can be determined in two different ways. The first one uses the plateau voltage U_{plat} to calculate the number of charges. Such a plateau will only be formed if the ion bunch fits totally into the detection electrode, or to be more precise, into the plateau region of the geometry function of the electrode. Remember, the geometry function

was defined as the fraction of the original charge is induced in the electrode taking their geometry and the position of the particles into account, see section (2.3.5). In the plateau region of the geometry function, all the induced charge is collected and therefore $\Xi(\boldsymbol{r}) \approx 1$ and equation (2.20) becomes [56]

$$U_{sig} = S \sum_{i=0}^{N} q_{in}^{i} \cdot \Xi(\boldsymbol{r_i}) = SNq = U_{plat}. \tag{2.21}$$

Rearranged, the particle number is given by

$$N = \frac{U_{plat}}{Sq} \tag{2.22}$$

and can be determined once the sensitivity S of the detection system is calibrated.

The second possibility to estimate the number of particles is by calculating the area Ω below the voltage signal.

$$\Omega = \int U_{sig}(t)\mathrm{d}t = Sq \sum_{i=0}^{N} \int \Xi(z_i, r_i)\mathrm{d}t. \tag{2.23}$$

Since the position in z-direction of the particle can be described in terms of the particles velocity by $z_i = v_i t$, the integral over time in equation (2.23) can be substituted by $t = z_i/v_i$ and therefore equation (2.23) changes to

$$\Omega = Sq \sum_{i=0}^{N} \frac{1}{v_i} \int \Xi(z_i, r_i)\mathrm{d}z. \tag{2.24}$$

Taking into account that $\int \Xi(z_i, r_i)\mathrm{d}z$ can be identified as the characteristic length L_{char} of the geometry function [57], the total number of particles is given by

$$N = \frac{v}{SqL_{char}}\Omega. \tag{2.25}$$

Combining both equations for the number of particles (2.22) and (2.25), one can determine the velocity of the particles and therefore their kinetic energy.

$$v = L_{char}\frac{U_{plat}}{\Omega} \qquad \Rightarrow \qquad E_{kin} = \frac{m}{2}\left(\frac{L_{char}U_{plat}}{\Omega}\right)^2. \tag{2.26}$$

It is worth noting that the sensitivity of the detection system cancels out and only the

characteristic length L_{char} of the electrode has to be know in order to determine the kinetic energy of the particles.

The last property which can be extracted out of the signal is the bunch length l_b of the particles. This can be done done by the slope h of the signal. It is given by [56]

$$h = \frac{\mathrm{d}U}{\mathrm{d}t} = \frac{NSqv}{l_b} \cdot \left[\Xi \left(z + \frac{l_b}{2} \right) - \Xi \left(z - \frac{l_b}{2} \right) \right] \tag{2.27}$$

in which z describes the position of the particle bunch. Between 0.1 and 0.9 of the signal amplitude this slope is constant. If the bunch is shorter than the rising edge of the geometry function the slope is independent of the bunch length and acts as a lower boundary for the bunch length determination. If it is longer, then the first part of the bunch has a geometry function value of unity and the last part of zero. Therefore, equation (2.27) can be used to determine the bunch length. Together with equation (2.22) and (2.25) this leads to [56]

$$l_b = \frac{U_{plat}^2 L_{char}}{\Omega h} \tag{2.28}$$

A more detailed description can be found in [57].

2.4.2. Resonant detection

Confined particles in a Penning trap perform oscillatory motions and hence lead to an oscillating image current I_p on the electrodes. The detection of this current is done by a RLC-circuit tuned to the motional frequency of the particles, and attached to one of the electrodes (pick-up electrode) as shown in figure (2.13). It was briefly mentioned in section (2.3.5) that the concepts of resonant detection and resistive cooling naturally come along with each other. While resistive cooling works by dissipation of the induced time-dependent image current in the resistance of the attached circuit without further requirements, in the case of resonant detection the time-dependent voltage drop, created by the induced current, is of interest. Going one step back, the motion of a stored particle in a Penning trap without dissipative elements like attached RLC circuits (ideal trap) can be described as an undamped oscillation [58] and the particle itself acts as a series LC circuit

$$l_P \frac{\mathrm{d}I_P}{\mathrm{d}t} + \frac{1}{c_P} \int I_P \mathrm{d}t = U_P. \tag{2.29}$$

2. Physics background and operation principles

Here, l_P and c_P are the inductance and capacitance of the equivalent LC circuit if connected to a voltage U_P [32, 50]. The induced current I_P for a single particle with charge q can be expanded in the case of a single charge state cloud with N particles to [32, 50]

$$I_p = \frac{Nq}{D_i}\dot{\rho}_i = \omega_i \frac{Nq}{D_i}\rho_i, \tag{2.30}$$

with ω_i, D_i and ρ_i $(i = z, +)$ being the oscillation frequency, effective electrode distance and position of the particle of the corresponding motion. Since the amount of current created by a particle, or even a particle cloud, is in the range of fA to pA, it becomes obvious that an amplification is required. This is done by attaching a coil with inductance L to the pick-up electrode.
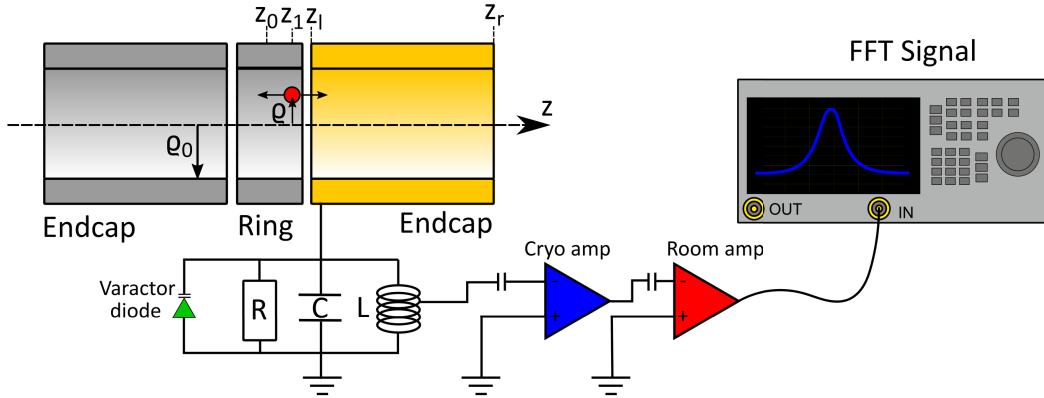
Figure 2.13.: Non-destructive resonant detection scheme with a parallel resonator (RLC-) circuit attached to the pick-up (endcap) electrode. R,L,C are the effective resistance, capacitance and inductance of the circuit. An additional varactor diode is used to tune the resonance frequency according to the particles oscillation frequency. A two-stage amplification with a cryogenic and room temperature amplifier is further connected. The signal is finally read out by a spectrum analyser which performs a FFT (Fast-Fourier-Transform) of the transient signal.

Like all real components, such a system comes along with a self capacitance C_{RLC} and together with the capacitance of the electrode C_{pick} it forms a parallel RLC-circuit. As described in section (2.3.5) this circuit has a resonance frequency of $\omega_0 = 1/\sqrt{LC}$, at which the impedance is purely real and acts as an effective parallel resistance given by

$$R = QL\omega_0, \tag{2.31}$$

with the quality factor Q of the circuit as defined by

$$Q = \frac{\omega_0}{\delta\omega}. \tag{2.32}$$

Together with the induced current I_P the expected voltage drop for a particle cloud reads as

$$U_P = RI_P = QL\omega_0 I_P = Q\sqrt{\frac{L}{C}}I_P, \tag{2.33}$$

in which $\omega_0 = 1/\sqrt{LC}$ has been used in the last step. It becomes obvious that higher charge states will produce a larger voltage drop, hence a larger signal, not only by an increase of the induced image current, but as well by an increase of the oscillation frequency and therefore a higher resonance frequency ω_0 of the detection circuit. Without changing the number or charge state of the particles, nor the geometry of the pick-up electrode, the only way to increase the signal can be achieved by increasing the effective resistance of the detection circuit. This can be done by a higher quality factor Q and/or a larger inductance of the coil. The latter most often results in an increase of capacitance as well which cancels out some of the effect. Nevertheless, even for a large effective resistance R of the circuit, the voltage drop is still small. Therefore, a further amplification is required. Most often this is realized by a two-stage amplification, as in the case of the charge counter (see section (2.4.1) and figure (2.13). One is located close to the pick-up electrode in the cryogenic environment and another one outside sitting at room temperature.

Design principles and considerations of the detection setup

In the previous section, equation (2.33) described the expected voltage signal from a single particle or particle cloud for a given detector with resonator parameters Q, L and C. A non-destructive, resonant detection system typically used in Penning traps consists of several components, beside the actual RLC-circuit, which cannot be neglected. These are for instance the pick-up electrode, the amplifiers or varactor diodes to tune the resonance frequency accordingly. Since all those individual parts have inherent losses, a lot of effort has to be made in order to keep parasitic capacitance as small as possible. Additionally equation (2.33) tells that the inductance of the coil has to be maximized. Finally the environmental conditions, for instance strong magnetic fields, cryogenic temperatures and most often the lack of space, requires specific design considerations which have to be incorporated and adjusted for each setup individually.

The most commonly used inductor coil designs are the helical and toroidal ones. I will

focus on the first one, as it is the one used for the HILITE resonators. A more detailed description of the latter one can be found in [50]. The basic idea is shown in figure (2.14).
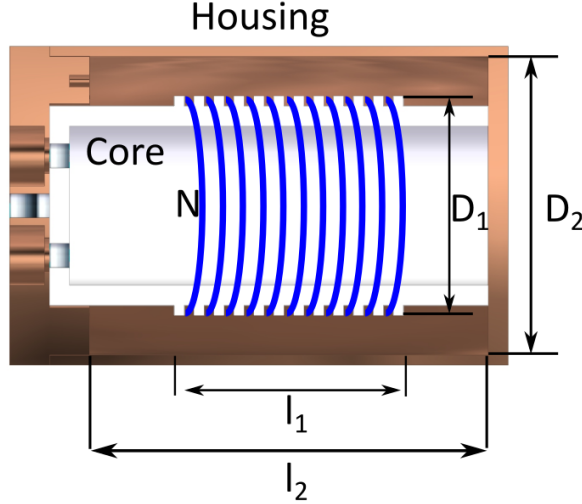

Figure 2.14.: Schematic of a helical resonator including important parameters. The wire (blue) is wound around the hollow core made of PTFE and together they are placed inside the OFHC copper housing.

The oxygen-free high-conductivity (OFHC) copper wire is wound around a hollow cylindrical core, most often made of polytetrafluoroethylene (PTFE, or Teflon) placed in the centre of a OFHC copper housing. The reason for those kinds of materials is their low dielectric losses. Alternatively, the material for the wire and the housing could be made of a superconducting material like niobium-titanium (NbTi) to further decrease the internal losses and increase the quality factor. Since the latter one is not used within HILITE. For more details about the implementation, challenges and capabilities I will refer the reader to [32, 50].

Although the calculation of the inductance and capacitance of individual ideal parts is rather easy and straightforward, one struggles while transferring towards real parts which are interconnected and further affected by the environmental conditions. Therefore the inductance and capacitance are estimated based on some semi-empirical formulas [59], which are given in the appendix (A.1).

One part of the detection system mentioned above which became important/popular over the recent years and is relevant for HILITE as well is the so-called varactor diode [50]. For experiments which use a rather broad spectrum of different charge states or, to be more precise, species with different q/m ratios, the use of varactor diodes can avoid the necessity to build several RLC-circuits, one for each q/m ratio. Since the motional frequencies of

charged particles in the axial and radial direction are described by equation (2.8) and (2.10) it becomes apparent that their frequencies are fixed. For the axial motion a change in the confinement potential opens a margin in frequency tunability, while the radial frequency cannot be changed, at least not without a huge effort in changing the magnetic field. Therefore, such a system is beneficial and used as well in the HILITE experiment. A varactor diode is basically a voltage-dependent capacitor. It operates in the reverse bias scheme, which means the current flow though the diode is blocked. Depending on the applied bias voltage the thickness of the diodes depletion zone (p-n junction in a semiconductor) changes as well as the capacitance. Connected in parallel to the RLC-circuit, as shown in figure (2.13), the total capacitance reads therefore as

$$C(U_{Var}) = C_{RLC} + C_{Var}(U_{Var}) \tag{2.34}$$

with the capacitance of the circuit C_{RLC} which is unaffected and the additional, voltage-dependent capacitance of the varactor diode $C_{Var}(U_{Var})$. Besides the capacitance, the quality factor Q is affected as well. It is given by

$$\frac{1}{Q_{(U_{Var})}} = \frac{1}{Q_{RLC}} + \frac{1}{Q_{Var}(U_{Var})}, \tag{2.35}$$

hence it has to be implemented in way not to be the 'bottleneck' of the systems' sensitivity.

2.5. Fundamentals of light-matter interactions

As already briefly discussed in (1.1) the photo-ionisation of ions from one charge state to the next higher one is the question of interest within this thesis. It requires, depending on the starting conditions like ion species and charge state, photon energies of at least several tens to hundreds of electronvolts to overcome the ionisation potential. Hence, either highly intense and/or high photon energy lasers are needed to access those domains. The concept of such systems was already described in (1.2) and the progress in development was tremendous. The effects taking place are usually higher-order processes, called multiphoton processes, corresponding to an involvement of more than one photon [60, 61]. The laser systems used are capable of generating fields, which can compete with the intra-atomic Coulomb forces. To give an idea, one can imagine a hydrogen atom in free space. The Coulomb force

2. Physics background and operation principles

between the nucleus (single proton) and surrounding electron can be described as

$$F_c = \frac{1}{4\pi\epsilon_0} \frac{e^2}{a_0^2},$$ (2.36)

assuming a_0 being the distance of the electron to the proton to be the first Bohr radius for atomic hydrogen and $q = |e|$ the absolute value of the electron charge. This force leads to an electric field at the position of the electron of the form

$$\mathcal{E} = \frac{1}{4\pi\epsilon_0} \frac{e}{a_0^2},$$ (2.37)

which results in a field strength for the hydrogen atom of about $\mathcal{E} \simeq 5 \times 10^9$ V/cm. The interaction of a laser and ion at high intensities can be described in a semi-classical approach, in which the laser field is treated classically, while the ion is described in terms of quantum mechanics [60]. This holds true, because the number of photons in such cases is large. A laser pulse, described as a classical electromagnetic wave, is defined by electric and magnetic fields. In the dipole-approximation only the electric field component remains, and the intensity I is proportional to the square of the amplitude of the electric field strength $I \propto \mathcal{E}^2$ and can be expressed as

$$I = \frac{1}{2}\epsilon_0 nc\mathcal{E}^2,$$ (2.38)

with c being the speed of light in vacuum and n the refractive index of the medium. So, the intensity of a laser has to be

$$I \simeq 3.5 \times 10^{16} \text{ W/cm}^2 := I_a$$ (2.39)

to equal the field strength created by an hydrogen atom. This is called atomic unit intensity I_a. If the laser intensity is much smaller than this intensity $I \ll I_a$, a perturbative approach can be used to describe the systems. Otherwise different techniques have to be used [60]. Increasing the nuclear charge Z and going to heavier elements changes the Bohr radius a_0 by $a_0 \propto 1/Z$ and hence, the electric field strength seen by the electron according to equation (2.37). Figure (2.15) gives an impression of the electric field strength and as a function of the nuclear charge Z for lowest-lying states in hydrogen-like systems. The corresponding intensity which is needed by a laser to reach the same field strength is shown as well.
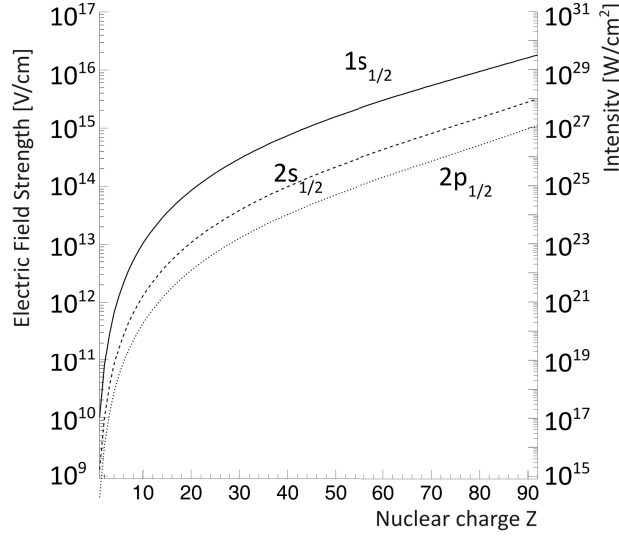
Figure 2.15.: Electric field strength and corresponding intensity as a function of the nuclear charge for lowest-lying states in hydrogen-like systems. From [62] - modified.

In general, one distinguishes between different regimes in terms of non-linear ionisation. The strong field or tunnel ionisation and the multi-photon ionisation. In 1965, Leonid Keldysh described in his model the influence of a strong, quasi-static electromagnetic field on the tunnel ionization rate of an atom [63]. Later, extended by the work of Ammosov, Delone and Krainov (ADK-theory) for slowly varying fields by averaging over one optical period [64]. An important quantity Keldysh introduced to distinguish the regimes is the so-called Keldysh-parameter γ_K defined as the ratio between the laser and tunnel frequency given by

$$\gamma_K = \sqrt{\frac{I_P}{2U_P}}. \tag{2.40}$$

Here, I_P represents the ionisation potential and U_P the ponderomotive potential, which is the cycle-averaged energy of an electron oscillating an electric field. In the case of a monochromatic laser field, it is given by

$$U_P = \frac{e^2 \mathcal{E}^2}{4m\omega} \tag{2.41}$$

with e being the electron charge, $\mathcal{E}$ the electric field strength, m the electron mass and ω the laser frequency. Combining equation (2.38) and (2.41) leads to $U_P \propto I/4\omega^2$ and finally with (2.40) to

$$\gamma_K = 2\omega \sqrt{\frac{I_P}{2I}}. \tag{2.42}$$

According to Keldysh, if $\gamma_K \ll 1$ the tunnel ionisation regime dominates, while for $\gamma_K \gg 1$ multi-photon ionisation is the preferred process. This distinction can be understood if one assumes for a fixed ionisation potential an increase in laser intensity and a low laser frequency. The higher the intensity, the larger the electric field strength becomes and by that the deformation of the Coulomb potential increases. Hence, the probability for the electron to tunnel through this barrier is increased as well - tunnel effect dominates. If the laser intensity is moderate, so is the field strength. Thereby the tunnel probability is decreased and multi-photon absorption is necessary for an ionisation to occur.

2.5.1. Multi-photon ionisation

As the name indicates, the process of multi-photon ionisation requires the absorption of at least two photons from an external laser field to occur. The first experimental observation and study was done by Damon and Tomlinson in 1963 [65] and subsequently by Voronov and Delone [66]. Following the distinction of Keldysh for $\gamma_K \gg 1$ the laser intensity should be moderate in relation to the ionisation potential and the frequency is preferred to be high. Figure (2.16 (a)) shows the effect schematically.
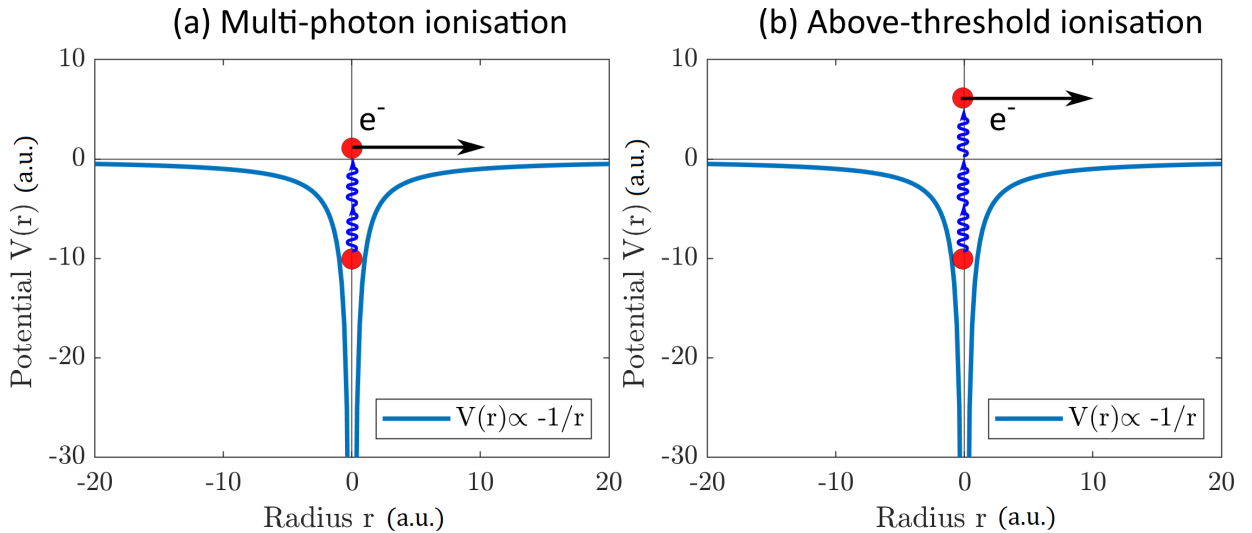
Figure 2.16.: Multi-photon ionisation regime according to Keldysh for $\gamma_K \gg 1$. (a) Multi-photon ionisation: Simultaneous absorption of at least two photons to reach the ionisation potential. (b) Above-threshold ionisation: If further photons are absorbed by the electron, the energy spectrum of such an electron will consist of distinct peaks, each separated by the photon energy $\hbar\omega$.

As long as the laser intensity is much smaller than the atomic unit intensity $I \ll I_a$

($I_a \simeq 10^{16}$ W/cm^2 for atomic hydrogen, which was defined as the intensity needed from the laser to be comparable to the field strength of the nucleus, see (2.39)), a perturbative approach, in which the laser field is described as a small perturbation of the intra-atomic Coulomb potential, can be applied. Performing those calculations, the ionisation rate of an n-photon process can be expressed as

$$w_n = \sigma_n \cdot I^n \tag{2.43}$$

in which σ_n represents the cross section of this n-photon process to happen and I^n is the intensity to the power of n, correspondingly. For higher field strengths, this approach breaks down, the cross section becomes intensity-dependent and deviations from the power law for the intensity arise.

Above-Threshold ionisation

Once the possibility of energy-resolved detection of the photoelectrons was achieved, a new effect occurred. In 1979, Pierre Agostini and co-workers [67] were able to resolve the energy spectra of a six-photon ionisation consisting of distinct peaks, separated by the photon energy $\hbar\omega$. By that, they showed that the electrons can absorb photons from the laser field, although the threshold for the number of photons for ionisation is already reached. This effect is therefore called *above-threshold ionisation*. A schematic impression can be seen in figure (2.16 (b)). As in the case for the multi-photon ionisation, for low intensities, the ionisation rates can be determined in a perturbative approach and leads to a dependency of $w_N \propto I^{N+s}$, with s being the number of excess photons.

2.5.2. Tunnel ionisation

The second regime introduced by Keldysh for $\gamma_K \ll 1$ describes the ionisation processes in terms of strong fields, like in the presence of intense lasers. Those fields compete with the Coulomb field created by the nucleus and if they are sufficiently strong, one refers here again to the atomic unit intensity (2.39), the Coulomb potential becomes deformed. The bound electron experiences an effective potential formed by the nucleus and the laser. It has therefore a finite probability to tunnel through this lowered potential. This is then called tunnel ionisation. Figure (2.17 (a)) displays this effect.

(a) Tunnel ionisation
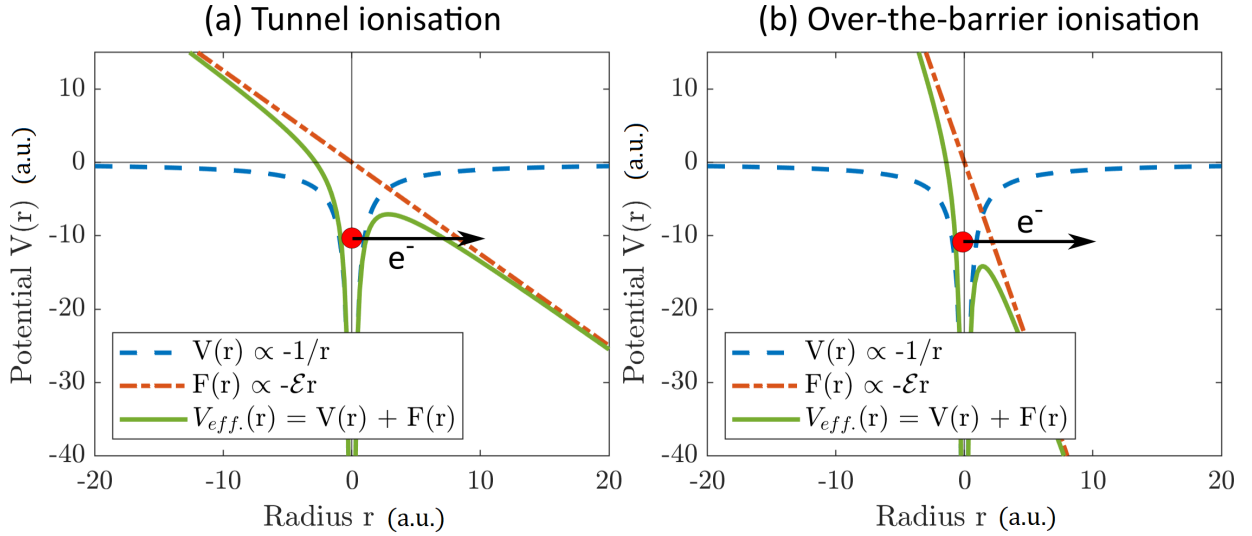
(b) Over-the-barrier ionisation

Figure 2.17.: Strong field ionisation regime according to Keldysh for $\gamma_K \ll 1$. (a) Tunnel ionisation: The strong field of the laser (red dashed line) bends the Coulomb potential of the nucleus (dashed blue line). The electron can tunnel through the resulting effective potential (green line). (b) Over-the-barrier ionisation: If the field strength is further increased, the effective potential is lowered in such a way, that the electron can escape by flying over the barrier.

The ionisation rate for this process to occur can be expressed as [60]

$$w_{tunnel} \propto \exp\left(-\frac{2(2I_P)^{3/2}}{3\mathcal{E}}\right). \tag{2.44}$$

with $\mathcal{E}$ being the electric field strength of the laser and I_P the ionisation potential of the undisturbed atom or ion, using the quasi-static model (ADK-theory) by [64].

Note that the intensity in an oscillating field varies throughout a cycle, and thereby the ionisation rate as well. Tunnel ionisation will most likely occur at the peaks of the electric field strength, so in a periodic way.

Over-the-barrier ionisation

In case the field strengths are further increased, the atomic potential can be lowered in such a way that the bound electron can 'classically' flow over the deformed barrier and no tunnelling has to occur at all. The description of the ionisation rate by a tunnel process therefore breaks down and the ionisation takes place 'immediately'. This is then called *over-the-barrier ionisation* and is depicted in figure (2.17 (b)).

3. The HILITE setup

This part of the thesis will concentrate on the setup of the HILITE experiment. An overview of the whole apparatus is shown in figure (3.1). For better presentation, the setup is additionally depicted from above in figure (3.2) and all the major parts are labelled and marked. The description and characterization of all those parts will be done in a consecutive way, starting with the ion production in our ion source and following their path through the setup. The subsequent charge state selection, several ion optical elements for beam guidance, diagnostic systems like MCP and charge counting devices and finally the deceleration and capture process in our Penning trap including the detection of stored ions inside the trap will be presented.
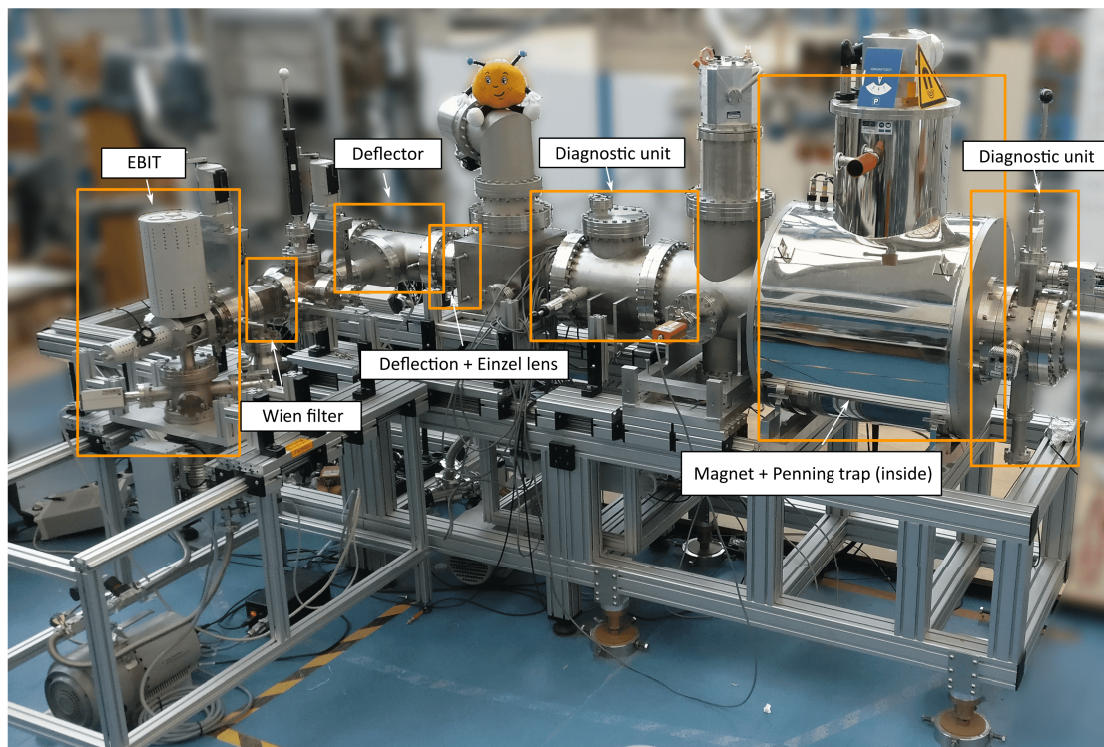

Figure 3.1.: Side view of the HILITE setup. Important parts are highlighted.
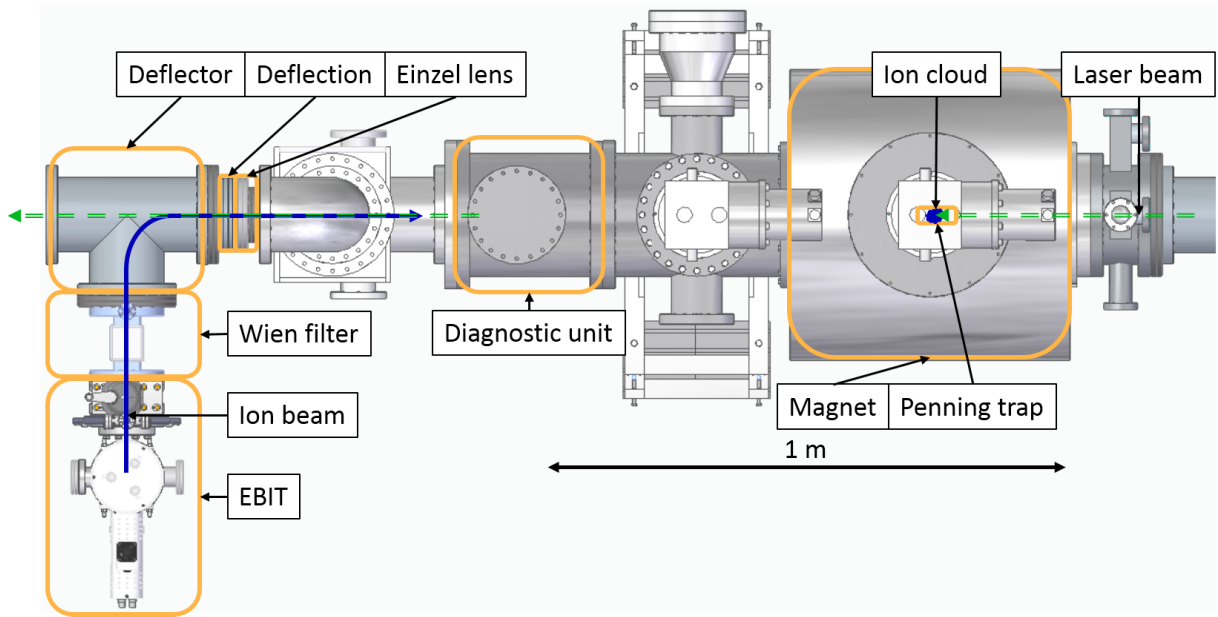
Figure 3.2.: CAD drawing of the HILITE setup seen from above. From [30] - modified. On the left hand side the ion source (EBIT) and charge state selection (Wien filter) can be seen, followed by a 90° electrostatic deflector to guide the ion beam onto the laser and Penning trap beam axis. Several ion optical elements and a diagnostic unit afterwards serve as and adjustment tool in order to enhance the efficiency of ion trapping.

3.1. Ion source - EBIT

The ion source used for the HILITE experiment is a commercially available EBIT (*Dresden-EBIT*) from the company *Dreebit* [68]. Since the general operation principles of such devices have been described in section (2.1.1), this part will focus on the specific properties of this device. Figure (3.3) gives an overview of EBIT, as well as a more detailed insight into the ion source indicating the most important parts. Relevant operation parameters are presented in table (3.1), while specific settings for different target species and charge states are given in table (A.2) and (A.3) in the appendix. The target gas used to benchmark the system was argon, since it has the advantage of being isotopic pure, easy to handle, all charge states accessible by the EBIT, and X-ray energy sufficiently high to be seen. Other relevant species for laser-ion interaction studies have been carbon and oxygen and will be discussed later on.

Table 3.1.: Dresden EBIT properties

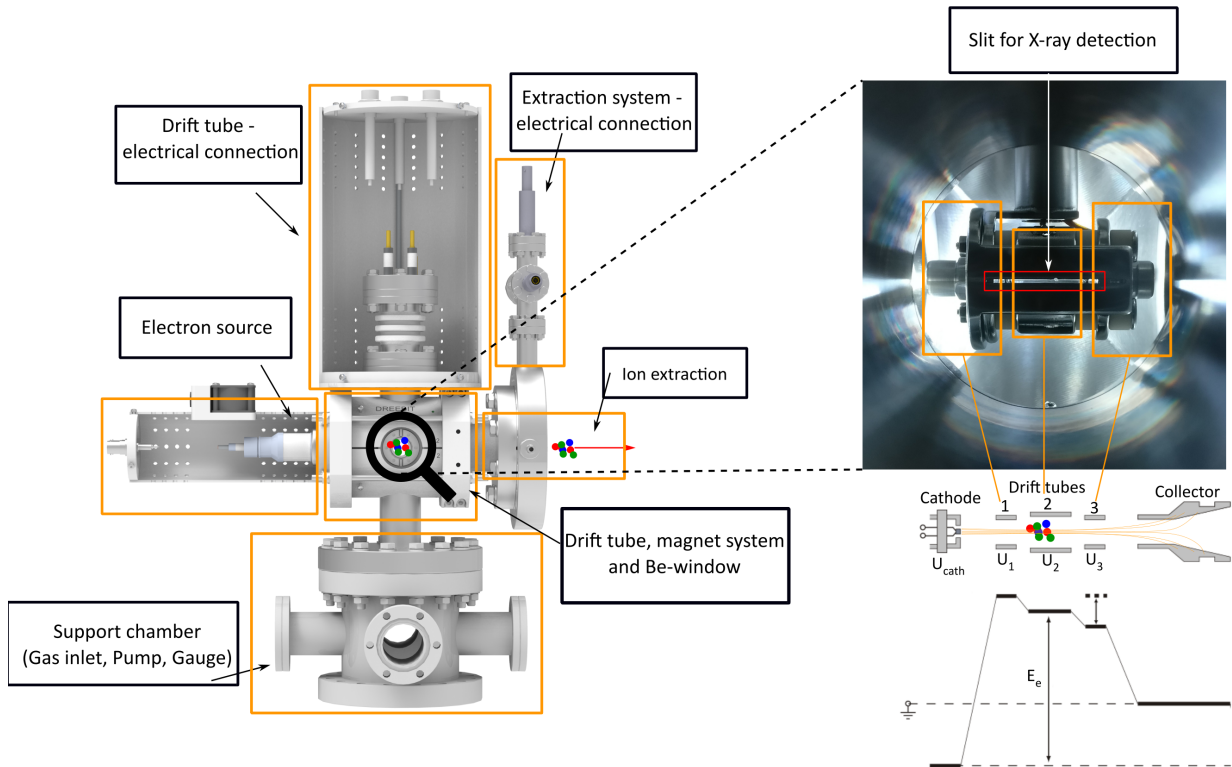| Parameter	max.	typical
Electron current I_e (mA)	50	10-30
Electron energy E_e (keV)	15	3-5
Cathode potential U_{cath} (kV)	-3	-3
Central drift tube Potential U_2 (kV)	12	0.8 - 1.0
Extraction potential $U_{extr1,2,3}$ (kV)	-6,-6,-6	$<U_{cath}$,≈ -2,≈ -2
Magnetic field strength (mT)	250	
Ionisation factor α_{IF} (e/cm^2)	$\approx 10^{21}$	
Heating current I_{cath} (A)	2.1	1.9 - 2.1
Operation pressure (mbar)	10^{-8}	$3 - 4 \cdot 10^{-9}$
Breeding time t_{breed} (pulsed mode) (ms)	10000	10-500

Figure 3.3.: (Left) Rendered CAD image of the EBIT indicating important parts. From [68] modified. (Right) Picture of the real ion source implemented in the experimental setup.

Starting from below, it consists of a 'support chamber' housing the turbo-molecular pump

(TMP), the pressure gauge and the gas inlet system controlled via a fine metering valve. Above that, the beam axis is placed. It can be divided in three major parts. The electron source, the drift tubes with the surrounding magnet system and the extraction system. The electron source is based on a filament with a diameter of 0.5 mm made out of iridium and cerium which is placed in the centre of a cathode. By application of a heating current I_{heat} through the filament (typically around 2 A) electrons are released and accelerated due to the negative potential applied at this electrode U_{cath}. In combination with the positive anode potential at the drift tube electrodes (U_1, U_2, U_3) the kinetic energy of the electrons is given as a first approximation by $E_e = e(|U_{cath}| + U_2)$. The superimposed magnetic field compresses the electron beam, such that the highest current density j_e is achieved at the drift tube region. There, the ionisation of the injected target gas takes place. The electron beam is damped in a water-cooled collector electrode and the ions are extracted via a system of three consecutive extraction electrodes.

The EBIT can be operated in two different modes. The first one is the so-called 'pulsed mode' in which the ions are extracted periodically in a bunch. This period (ionisation cycle) is defined by the sum of the breeding time t_{breed} and the opening time t_{open} of the 'downstream' drift tube electrode U_3 which is lowered to empty the trap. Afterwards a new ionisation cycle starts. The second operation mode is the 'leaky mode', in which the drift tube electrode U_3 remains at a high potential, whereby the trap stays 'closed' in the first place. Like all traps, the maximum number of charges within the confinement volume is limited. The longer the trap is closed, the more ions and/or higher charges states are produced. Once the maximum amount is reached, they can overcome the closed potential of the electrode in close analogy to an overflowing barrel of water, and a constant flow of ions is extracted. The characterization of the trap content of the EBIT can be performed in two different ways. The first one is by measuring the X-ray spectra created by the ionisation and recombination processes occurring in the trap while it is in a closed configuration. The second one is done by a time-of-flight (ToF) analysis of the extracted ion bunch outside of the EBIT. Both have been performed and will be presented.

3.1.1. X-ray analysis of the EBIT content

Since the maximum potentials and electron currents which can be applied to Dresden EBIT are limited, see table (3.1), the expected photon energies are in the soft X-ray regime, of the order of $2 - 30$ keV. For such small energies the absorption of the stainless steel drift tube electrodes would be sufficient to block all created photons, although the thickness is

only in the millimetre range. Therefore, the drift tubes are equipped with horizontal slits along the beam axis to transmit the X-ray photons, as can be seen on the right hand side of figure (3.3) within the red box. Now, the photons can be extracted from the drift tube, but will still be absorbed by the vacuum flanges of the EBIT. To circumvent this, one of those flanges is replaced by a beryllium (Be-)window. As a light element (atomic number of 4) and mechanical stability down to micrometre thickness the absorption especially for X-ray photons is in comparison to others materials small, and therefore commonly used in X-ray spectroscopy. The Be-window implemented in our setup is 50 µm thick and placed onto a CF-16 flange, as depicted in the left part of figure (3.3). The detector used for the spectroscopy is an *Amptek XR-100CR Si-PIN X-Ray detector* [69] with a resolution of 150 eV to 250 eV in the expected energy range. Additionally it is equipped with a 25-µm-thick Be-window in front of the silicon multilayer detector surface. The complete detection system was energy-calibrated with an Am-241 source and all extracted spectra have been efficiency corrected based on the detector and absorption corrected for 75 µm of beryllium (50 µm EBIT, 25 µm detector) and 10 mm of air (distance of the detector to the EBIT).

The measurements have been performed in the following way. First the target gas, argon in our case, has been injected by a fine metering valve into the EBIT. The pressure in the chamber was set to $3 - 4 \cdot 10^{-9}$ mbar. Afterwards a scan for different breeding times with a constant electron energy has been performed, followed by a scan of the electron energy for a fixed breeding time. The electron current $I_e = 12.7$ mA has been kept constant during all measurements by adjusting the heating current I_{cath} accordingly. Therefore the electron current density stays constant and the ionisation factor is purely dependent on the breeding time. The cathode potential $U_{cath} = -3$ kV, the drift tube potentials $U_1 = 30$ V, $U_3 = 25$ V and the trap opening time $t_{open} = 30$ ms were also unchanged. In order to achieve sufficient statistics, each X-ray spectrum was recorded for six hours. The results are plotted in figure (3.4). In this first measurement, the electron energy $E_e = 4450$ eV was kept constant and the breeding time was varied. For a constant current density ($I_e = const.$), larger breeding times result in higher charge states.
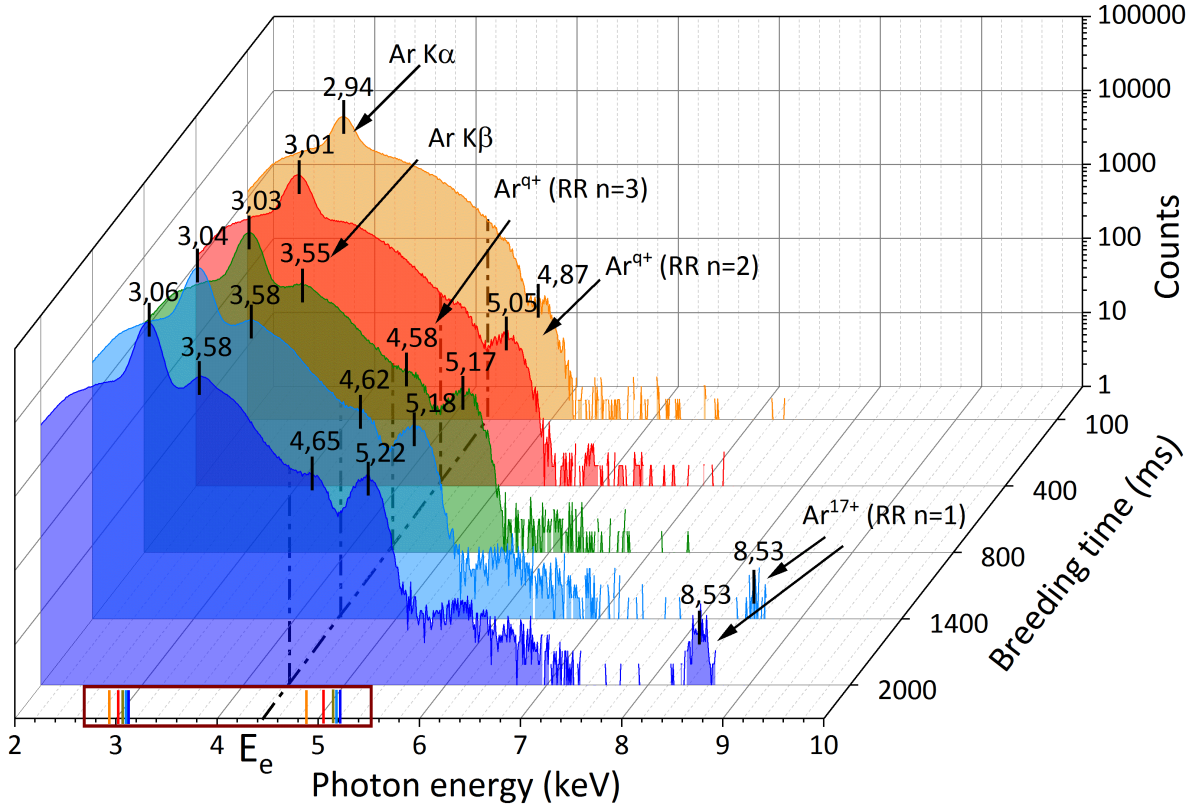
Figure 3.4.: X-ray spectra of argon ions in the EBIT for different breeding times τ_{breed}. Electron was kept constant at energy $E_e = 4.45\,\text{keV}$ as depicted. One can explain the energetic shift of the characteristic X-ray lines (Kα, Kβ) towards higher energies due to an increase of the average charge state for larger breeding times and therefore by an increase of the binding energy for the remaining electrons. Recombination processes like 'radiative recombination' (RR) into different shells can be seen and partially identified as well.

As expected, the characteristic X-ray lines, Kα and Kβ can be identified. They are created when outer-shell electrons fill a vacancy in the inner-shell of an atom. It is called 'characteristic', since the energy levels of each element is individual and therefore unambiguous. Kα-photons are emitted if an electron from the outer shell (L-shell, n = 2) is transferred towards the inner shell (K-shell, n = 1). The energy of those photons $E_{K\alpha} = |E_{n=2} - E_{n=1}|$ equals the difference in binding energy between those two shells. Kβ-photons are created by the transition from the outer shell (M-shell, n = 3) towards

the inner shell (K-shell, n = 1) correspondingly. Due to a screening effect in which the remaining electrons shield the potential of the nucleus, the energy levels and therefore the binding energies differ depending on the charge state of the ion. Hence, higher charge states result in less shielding, so an increase in binding energy and therefore a higher energy for the corresponding characteristic photons. This effect can be seen as well in figure (3.4). The coloured lines inside the box at the x-axis of figure (3.4) shows the shift of the X-ray lines towards higher energies for larger breeding times and hence higher charge states. Additionally, further peaks could be identified due to the effect of 'radiative recombination' (RR). Radiative recombination occurs if an electron vacancy in the shell is filled up with an electron of the electron beam. Therefore the emitted photon has the energy of the sum of the binding energy for this vacancy and the electron energy $E_{RR} = E_e + E_n$. Since this energy is always larger than the electron energy, it can be found after the edge of the X-ray bremsstrahlung, as indicated in figure (3.4) by the dashed line. RR-effects could be found for capture into the M,L-shells (n = 3, 2), as well as into the K-shell (n = 1) for larger breeding times. Specifically the charge state of the RR into the K-shell could be identified as Ar^{17+} since the energy difference for RR into K-shell for Ar^{18+} would be $300\,\text{eV}$ higher and could therefore be resolved by the detector. Since the difference in energy for the RR into the M- and L-shells are much smaller and the superposition of several charge states broadens the spectra, the exact assignment of charge states could not be achieved.
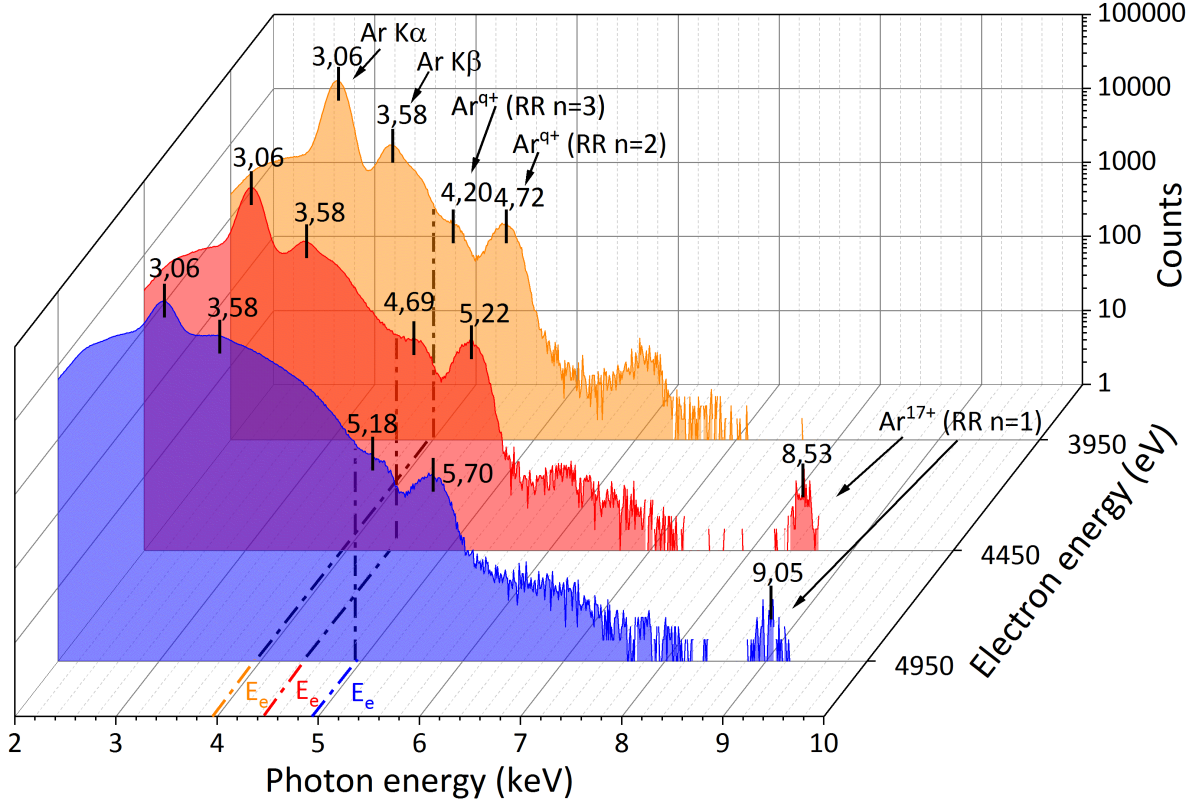
Figure 3.5.: X-ray spectra of argon ions in the EBIT for different electron energies E_e. Breeding time was kept constant at $\tau_{breed} = 2000\,\text{ms}$. Due to an increase of the electron energy one reaches the binding energy of the first K-shell electron (Ar^{17+}) and RR into this shell occurs. The X-ray energy of this effect is shifted by the same amount as the electron energy is increased.

The second measurement which was performed was a scan of the electron energy E_e for a fixed breeding time of $\tau_{breed} = 2000\,\text{ms}$. Two additional electron energies of $E_e = 3950\,\text{eV}$ and $E_e = 4950\,\text{eV}$ in comparison to the previous one of $E_e = 4450\,\text{eV}$ have been used. The results are depicted in figure (3.5). Since the breeding time for all electron energies is sufficiently high to produce the highest charge states, only the electron energy defines if a charge state is accessible or not. This can be seen for instance for an electron energy of $E_e = 3950\,\text{eV}$, in which no RR into the K-shell could be measured. That's because the energy needed to ionise Ar^{16+} to Ar^{17+} is about $E_{e16+\to17+} \approx 4100\,\text{eV}$ and hence only possible for higher energies. This process occurring could be verified for the two subsequent

measurements with higher electron energies as shown as well in picture (3.5). The position of the RR line into the K-shell $E_{RR,n=1} = 8530\,\text{eV}$ for Ar^{17+} fits with the theoretical expectation, that it should be at $E_{RR,n=1} = E_e + E_{16+\to17+} = 8550\,\text{eV}$ for an electron energy of $E_e = 4450\,\text{eV}$ and $E_{RR,n=1} = 9050\,\text{eV}$ for $E_e = 4950\,\text{eV}$. Additionally, the positions of the RR lines into the M- and L-shell have been shifted as well by the same energy difference of the electron energy of $\Delta E_e = 500\,\text{eV}$ between the two measurement settings. The characteristic Kα and Kβ lines have not been shifted in this measurements due to the fact that the highest charges states had already been produced for $\tau_{breed} = 2000\,\text{ms}$.

3.1.2. Time-of-flight (ToF) analysis of the extracted ion bunch

Another method to characterize and measure the ion content of the EBIT is the extraction by lowering one of the drift-tube potentials, as described in (3.1), and release of the ions onto an external detector. The system used is a multichannel plate (MCP) detector, with a timing anode to measure the arrival time of the ions. The start time of the ions is defined by a trigger pulse of the EBIT's power supply once the drift tube potential is lowered. The time between those two points is defined as the time of flight of the ions. Since the ions' kinetic energy is in first order given by the potential of the central drift tube times their charge $E_{ion} = q \cdot U_2$, the arrival time and therefore the time of flight will change and lead to a spatial spread of the different charge states. It can formally be described by

$$t_{ToF} = s\,\sqrt{\frac{m}{2U_2}} \cdot \frac{1}{\sqrt{q}}, \tag{3.1}$$

in which s is the distance the ions have to travel between the EBIT and the MCP and m is the ion mass. The first part is a constant, since the mass will not change due to the isotopic purity of argon, and therefore the time of flight can be described as a linear function dependent on the inverse square root of the charge state. Even further, they can be explicitly identified by that. Each deviation from the linear behaviour would tell that the assignment for the charge states was wrong. The results of such a ToF measurement can be seen in figure (3.6) and (3.7). The electron energy ($E_e \approx 4100\,\text{eV}$) and current ($I_e \approx 11\,\text{mA}$) , the extraction parameters and the pressure ($p = 4 \cdot 10^{-9}\,\text{mbar}$) have been kept constant, while the breeding time was varied. Although the energy was not changed one can clearly see on the left hand side of picture (3.6) the shift in the composition of the ion bunch towards higher charge states for larger breeding times.
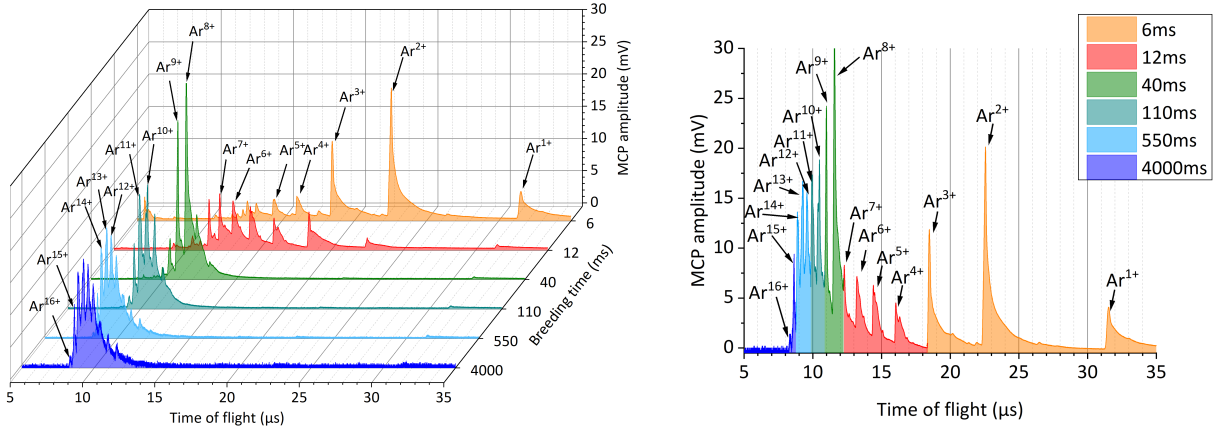
Figure 3.6.: ToF spectra of argon for different breeding times, hence different charge states. While the left hand side shows the complete spectra of each breeding time setting, the right hand side is a combination showing only the most prominent ones for each setting. The position of the peaks in this plot is used further for the linear fit in figure (3.7). A shift of the charge state composition of the extracted ion bunch towards higher states for larger breeding times can easily be identified.

The second plot on the right hand side of (3.6) is basically a projection of the results from the left side, in which only the most prominent peaks for each breeding time is shown and combined. The colour representation is equal for both plots. The projection plot is further used to identify the position (ToF) of the individual charge states and plot them as a function of the square root of the inverse charge state, as follows from equation (3.1). The result is plotted in figure (3.7) and shows the expected linear dependency in ToF for different charge states with the same atomic mass. The well-disposed reader will recognize that the highest charge state achieved in the ToF measurements is Ar^{16+}, while in case of the X-ray spectroscopy it was Ar^{17+}. The reason for that is the reduced electron energy used for those measurements which is not sufficient to access the K-shell electrons starting from Ar^{16+}. Due to deceleration limits in the remaining experimental setup the maximum kinetic energy ions are allowed to have in order to be captured in the Penning trap is $E_{ion} \approx 1000\,\text{eV}$ ($E_e = e(|U_{cath}| + U_2)$) and limits therefore the maximum charge state.
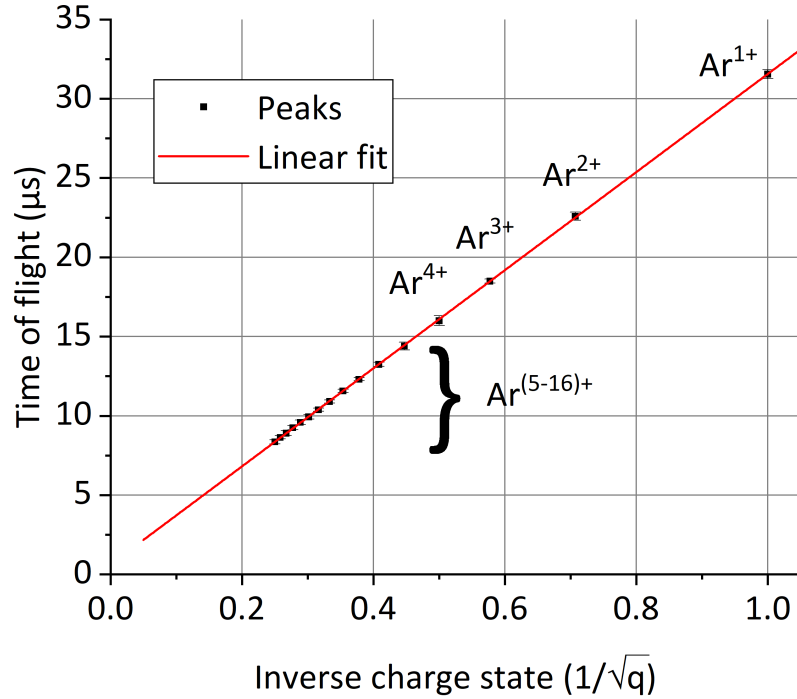
Figure 3.7.: Linear fit of the ToF for different argon charge states, extracted from the measurements shown in figure (3.6). Error bars are barely visible. Since the expected linear behaviour is well represented by the fit, the assignment of the charge states is shown to be correct.

In summary, both methods, the X-ray spectroscopy and the ToF measurements reveal the same results under the considerations of the slightly different EBIT settings (mainly electron energy and breeding time) and can be used complementarily. The spectroscopy is limited by the resolution of the X-ray detection and absorption in the low energetic ($< 3\,\mathrm{keV}$) regime, while it can be applied without affecting the trap content. In case of the ToF measurements, the limits are given by the physical dimensions of the setup, since longer distances lead to spatial spread and hence higher resolution of the different charge states. A compact setup limits this capability. Additionally, the detection ('destructive') of ions with an MCP leads to a loss of those ions and prevents them from being used further. Nevertheless, the successful extraction of an ion bunch, which includes the wanted charge state, is the first step for laser-ion experiments.

3.2. In-flight ion selection: Wien filter

Since extracted ion bunches from an EBIT ion source are always a combination of different charge states, a selection or separation process for one of them is required, in order to perform experiments with an ion target of a specific, isolated charge state. This is realised in our setup by a Wien filter implemented downstream of the EBIT. The operation principle is based on the superposition of an electric field perpendicular to a magnetic field as well as towards the flight direction of the ions. Due to a balance between the electric and magnetic parts of the Lorentz force, ions with a specific velocity, which corresponds to a specific charge state, will be transmitted. A more detailed description and operation principle were already presented in section (2.1.2), so this part will be focused on the experimental realisation. The system used is a commercially available Wien filter from the company *Dreebit* [68], like the aforementioned EBIT ion source. The most important device properties are given in table (3.2).

Table 3.2.: Wien filter properties

Parameter	max.	typical/used
Magnetic field [mT]	140, 500	140
Voltage [V]	± 1000	$30 - 150$
$\varnothing$ aperture [mm]	0.5, 1.0, 1.5, (2.0)	2.0
Inter. length [mm] (Superimposed fields)	75	

A picture of the device, indicating the most important parts, is presented in figure (3.8). The permanent magnet is changeable and is placed on the atmospheric side, so a vacuum break is not needed in order to change it. Two different field strengths ($B = 140\,\text{mT}$ and $B = 500\,\text{mT}$) are available. Unless otherwise stated, the weaker one is used during the measurements. Since the magnetic field is oriented in the horizontal plane, the electric field has therefore to be in the vertical plane as indicated in figure (3.8) to be perpendicular to both the magnetic field and the flight direction of the ions. For a fixed and given distance between the electrodes, the applied potential defines the field strength. The characterisation of the device and operation procedure are explained in the following for argon of various charge states, as was the case for the EBIT, and can directly be transferred to other ion species.

First, the transmission 'without' the Wien filter is performed. This means that the
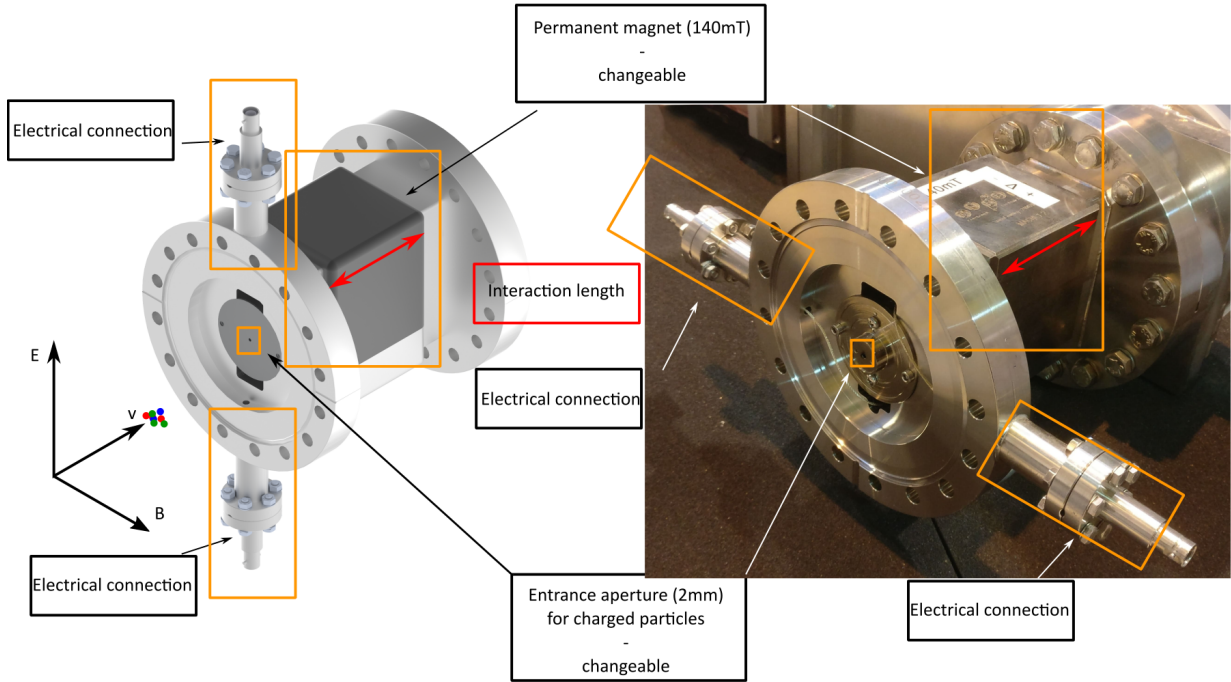
Figure 3.8.: Pictures of the Wien filter. Left hand side shows a rendered CAD image, from [68] - modified, while the on the right the Wien filter within the experimental setup is depicted. Important parts like the changeable permanent magnet as well as the entrance aperture which can be changed in size are marked and labelled.

permanent magnet is removed and the electrodes are earthed (set to zero potential). By that, ions which enter the filter can pass unhindered onto a MCP detector ('full transmission'). The time-of-flight information received from this measurement can be used to identify the charge state, as already shown in section (3.1.2). This is depicted by the blue curve in figure (3.9) for a breeding time of $\tau_{breed} = 300\,\text{ms}$. Once this is done, the magnet is put back into place and a potential is set onto the Wien filter electrodes. Once a balance between the magnetic and the electric forces is achieved, a transmission of a certain velocity/charge state can be observed. Since the balance between the two fields only holds true for a small velocity window, only a single charge state is selected and passed through the filter. A repeated process of a stepwise increase of the Wien filter potential is performed until the settings for the charge state of interest are found. As an example, the selection of Ar^{13+} with the Wien filter potential of $U_{wien} = 102\,\text{V}$ can be seen in figure (3.9).
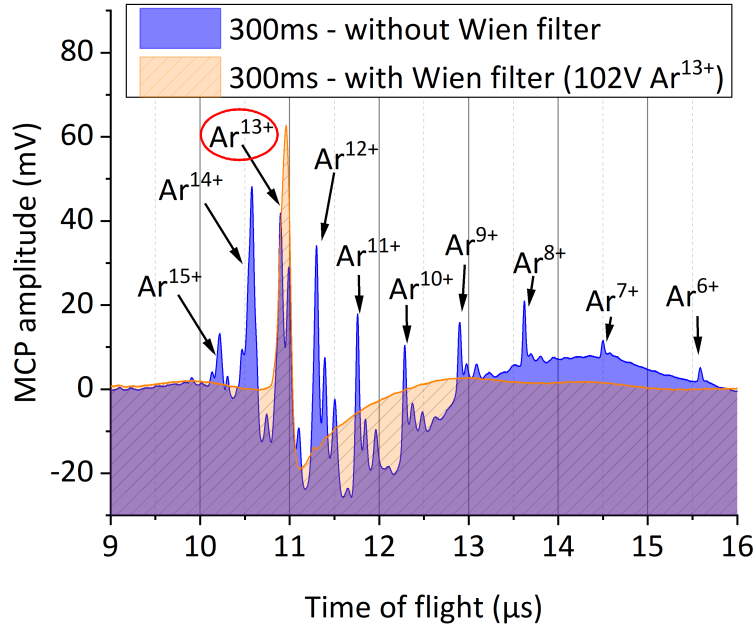
Figure 3.9.: Acquired argon spectra for a breeding time of $\tau_{breed} = 300\,\text{ms}$. First, the permanent magnet was removed and no electric potential was applied. By that, the transmission of all produced charge states can be recorded (blue curve). Once the magnet is back in place, charge states can be selected by appropriate choice of the electric potential applied onto the Wien filter electrodes. Shown as an example for Ar^{13+} (orange curve).

The potential needed on the electrodes for all argon charge states, as well as for different species, like carbon and oxygen is shown in table (A.3) in the appendix.

After the successful selection of the desired charge state, further steps have to be performed in order to finally store the ions in the Penning trap.

3.3. Ion beam optics and diagnostics

After passing through the previously described Wien filter, the ion bunch consists of a single charge state but as can be seen in figure (3.2) the trajectory is still perpendicular towards the Penning trap axis. Hence, further ion optical elements to manipulate and diagnostic systems for the detection of the ion beam are needed.

3.3.1. Electrostatic 90°-deflector

In a first step, the charged particles have to be guided onto the trap axis and therefore a device is needed which can deflected the beam by 90°. At the same time, the laser which is used for the ionisation processes during the experiment has to be able to pass the deflector in order to prevent laser ablation and damage of the system. Due to those constraints, the system used is an electrostatic deflector, equipped with a hole in the electrode to pass the laser beam. An impression of the device is given in picture (3.10). It is a *Columbia CIBD-100-H* double-focusing 90°-deflector from *Beam Imaging Solutions* [70].
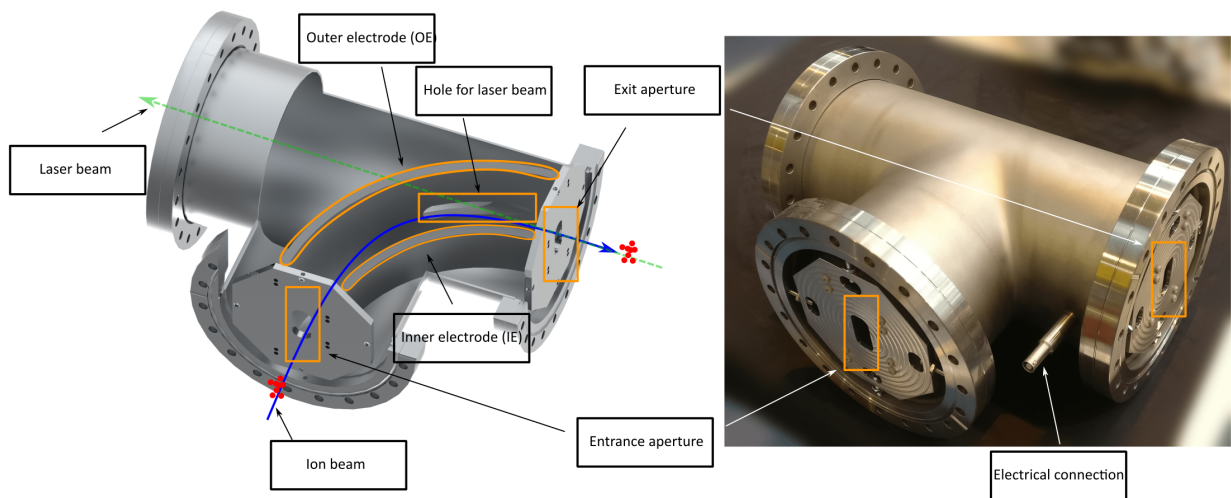

Figure 3.10.: (Left) Rendered CAD image of the electrostatic 90° deflector. The ions enter the system from 'below' and the trajectory is changed due to an electrostatic field, created by a potential applied to the outer and inner electrodes (OE,IE). The laser beam can pass the device unaffected through the hole in the OE. (Right) Picture of the actual electrostatic 90° deflector.

It consists of two concentric cylindrical plates with a radius of 140 mm for the inner electrode (IE) and 178 mm for the outer electrode (OE). In addition, the heights of the two electrodes differ, being 45 mm for the IE and 101 mm for the OE. Thereby, an electric field perpendicular to the deflection plane is created and focussing in this plane is possible as well (double-focussing) [31]. Picture (3.10) shows the system implemented in the chamber (right), and a CAD section view of the interior parts (left). The OE is further equipped with a hole on the trap axis, in order to transmit the laser beam undisturbed. The two electrodes are mechanically mounted on both sides onto two so-called face plates with apertures of 35 mm x 16.5 mm in size for the particle beam to enter and leave. The two

57

face plates are further used to align and fix the whole device in a CF-160 T-piece vacuum chamber. Simulations have been performed with *SIMION*, a field and particle trajectory simulator [71].
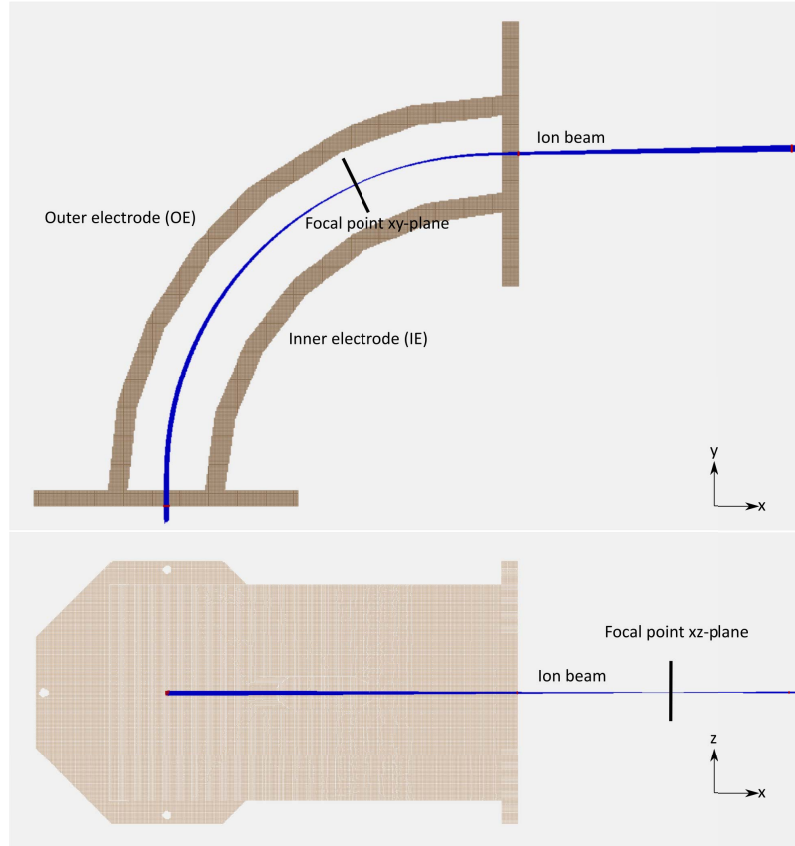

Figure 3.11.: *SIMION* geometry of the 90°-deflector with the particle trajectories of 200 C^{2+} ions. The kinetic energy was $E_{ion} \approx 900$ eV/q and the voltages on the electrodes have been (OE $+355$ V, IE -10 V). One can see that the focal point for the two different planes are not necessarily at the same position. This can be tuned by the applied voltages.

Therefore, the geometry of the deflector was created within the software and the particle trajectories have been studied for various potentials applied on the electrodes and different particle starting conditions like kinetic energy, ion species, charge state and spatial distribution in order to find optimal operation parameters and compare them with the experimental results (see section 3.3.2). Figure (3.12) shows the simulation results for a C^{2+} ion beam consisting of 200 particles and a kinetic energy of $E_{ion} \approx 900$ eV/q. The starting distribution (black circle) 40 mm in front of the deflector, the distribution at the entrance of the deflector (blue dots) and the distribution 128 mm behind the deflector (red dots) at

the position of the Einzel lens are presented. Depending on the applied voltages on the electrodes, the shape of the beam after leaving the deflector can be adjusted as the three presented cases in figure (3.12) show.
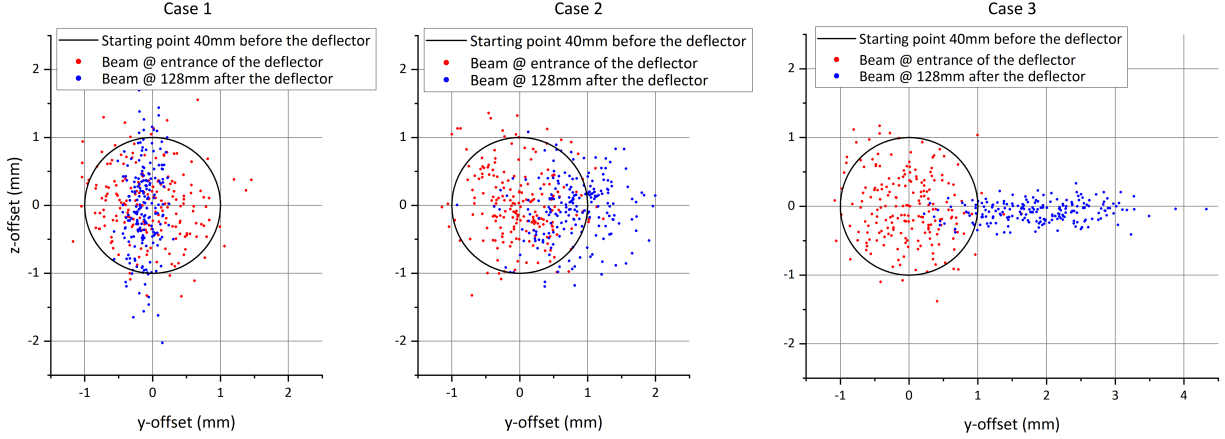

Figure 3.12.: Simulation of a C^{2+} ion beam with a kinetic energy of $E_{ion} \approx 900\,\mathrm{eV/q}$ for three different parameters sets (applied voltages), called 'cases'. From left to right, case 1 (OE $+10\,\mathrm{V}$, IE $-540\,\mathrm{V}$) leads to a vertical line-shaped beam, case 2 (OE $+219\,\mathrm{V}$, IE $-219\,\mathrm{V}$) to a spherical-shaped beam, and case 3 (OE $+355\,\mathrm{V}$, IE $-10\,\mathrm{V}$) to a horizontal line-shaped beam as expected from a double-focusing deflector [31].

As previously described, the different heights of the electrodes lead to an electric field perpendicular to the deflection plane causing a focussing in this plane as well. The focal points of the two planes are not necessarily located at the same position and can be described as a function of the applied voltage. If the voltages are distributed differently the ion beam has either a vertical line-shape or a horizontal line-shape at a certain distance after the deflector as depicted in (3.12) for the cases 1 and 3. Only for similarly distributed voltages a spherical shape can be received as case 2 shows for equally-distributed voltages. Since a spherical shape of the ion beam is beneficial in terms of magnetic and electric field gradients (all applied fields have a radial symmetry related to the beam axis) for the following deceleration and capture process, this setup is further used in the experimental cycle. A more detailed investigation and presentation was performed in the course of a master's thesis and can be looked up in [30].

3.3.2. Diagnostic Unit: MCP with a phosphor screen

For an efficient ion capture process, not only the number of ions in the beam is of relevance, but also the spatial distribution in radial as well as axial direction is of great importance. The axial distribution, or length of the bunch can be determined by our non-destructive flyby charge counter device which will be presented in detail in the next section. The radial distribution is more challenging and is done by the detection of fluorescence light created by a MCP detector equipped with a phosphor screen from *PHOTONIS* [72]. Since the number of particles in such an ion beam is rather small, the MCP stage is needed to amplify the signal. The MCP is mounted onto a metal frame which houses a mirror, placed under a 45° angle in order to extract the produced light through a vacuum window onto a computer-controlled camera. Figure (3.13) shows the interior parts of the diagnostic unit with the most important parts. A more detailed description of the setup and the devices and parameters are given in [30].
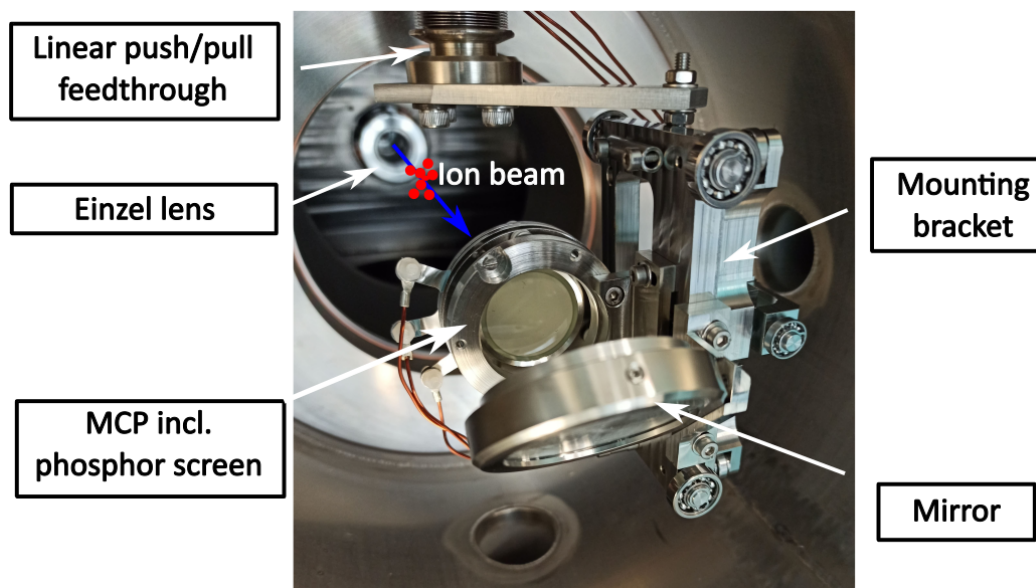
Figure 3.13.: Picture of the diagnostic unit seen against the flight direction of the ions. The MCP with phosphor screen on the back, the mirror and the mounting bracket of the system which is connected to the linear vacuum feedthrough in order to place the detector inside or outside of the beam is labelled. From [30] - modified.

The whole frame is fixed to a mechanical feedthrough which allows to retract the detector if not needed. A position scale indicates the central position of the device in relation to the ion beam axis in order to make assumptions about the ion beam position in the radial

direction. Based on the simulations performed and presented in the previous section (3.3.1) one expects either a vertical, a horizontal or a spherical shape of the ion beam depending on the applied voltages. This can be confirmed and is depicted in figure (3.14), from left to right for the cases 1, 2 and 3 respectively. The parameters used have been the same as in the simulations, i.e. a C^{2+} ion beam with a kinetic energy of $E_{ion} \approx 900\,\text{eV/q}$. The applied voltages are given in the pictures and agree with the ones used for the simulations. The Einzel lens was used to focus the ion beam onto the MCP, since the diagnostic unit had to be placed further 'downstream' of the beamline and is therefore at a different position than in the simulations.
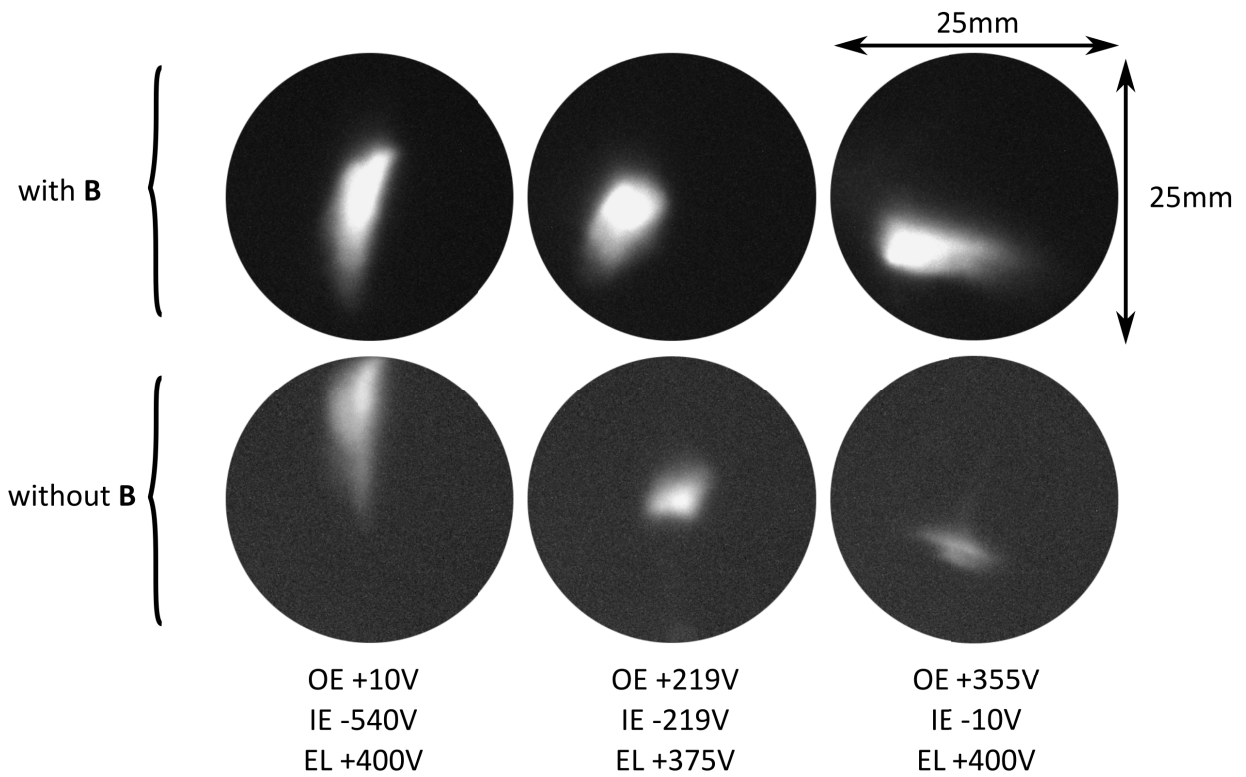
Figure 3.14.: Images of the C^{2+} ion beam on the $25\,\text{mm}$ phosphor MCP in the diagnostic chamber. The upper row shows the signals with an applied magnetic field of $B = 3\,\text{T}$, while the lower one depicts the results without a magnetic field. From left to right the three corresponding cases 1, 2, 3 from section (3.3.1) are depicted. The applied voltages on the deflection electrodes are shown. A vertical, a spherical and a horizontal profile can be recognized. The Einzel lens (EL) was used in all cases to focus the ion beam onto the MCP.

It is worth noting that the influence of the magnetic field in terms of focussing/compressing of the beam can clearly be seen and is helpful to compensate the divergence due to space

charge effects.

3.4. Inside the magnet bore: Detection, deceleration and storage

The next important part in terms of ion optics after the diagnostic chamber are all placed inside the 150 mm magnet bore. Since this is already the in the cryogenic environment (4 K and 45 K stages), a CAD section view is shown in figure (3.15) to show the interior parts.

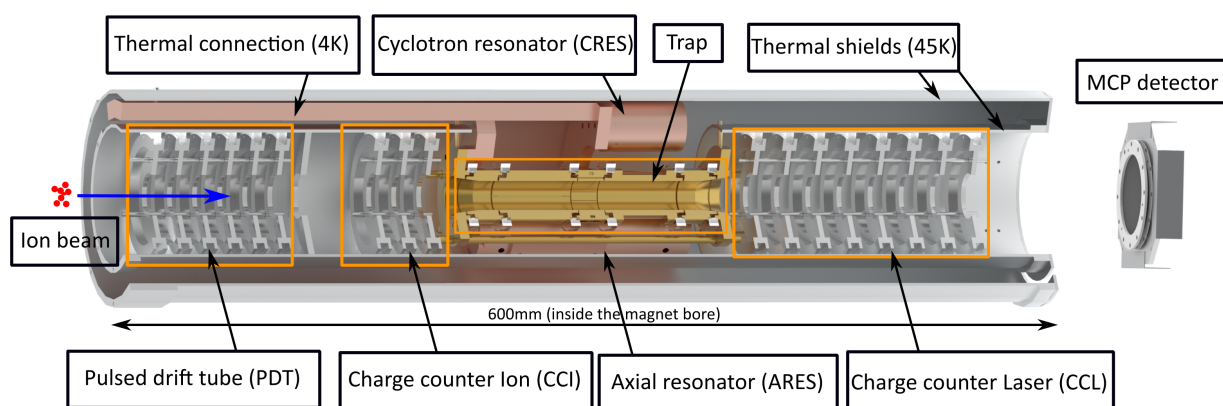Figure 3.15.: CAD section view of the interior of the magnet bore. The whole setup measures about 600 mm in length. From left to right the pulsed drift tube (PDT), the charge counter on the ion side (CCI), the Penning trap in the centre and the charge counter at the laser side (CCL) is shown. A thermal connection out of copper cools the trap and surrounding axial and cyclotron resonators (ARES+CRES) down to around 4 K. Two thermal shields protect the system from the room temperature magnet bore. A bit outside, a MCP is placed for timing information and destructive detection of the ion beam.

The ion beam enters the magnet bore from the left and is first decelerated in the pulsed drift tube (PDT). Afterwards, it passes the first charge counter (CCI) and is detected non-destructively before being captured and stored in the Penning trap. A second charge counter (CCL) is located on the opposite side of the trap and can be used to detect either extracted ions from the trap or the primary ion beam in a transmission-mode operation where ion storage is not required. All devices are placed inside of two cylindrical aluminium tubes operated as a thermal shield at 45 K in order to cool the trap and the surrounding detection systems (ARES + CRES) and electronics down to 4 K. The thermal connection to

the pulsed-tube cooler is realized by a copper rod and additional aluminium parts housed in a dedicated vacuum chamber on the left side of the magnet bore, but is not further discussed here. Since a statement about the efficiency of the deceleration process is mainly done by an analysis of the non-destructive charge counter signals, the order of the two following sections is inverted, although the PDT is passed first, seen from the ions perspective.

3.4.1. Ion detection: Non-destructive single-pass ion counter

The non-destructive charge counter setup consists of two independent devices, the charge counter on the ion side (CCI) and the charge counter on the laser side (CCL) as shown in figure (3.15). The overall operation principle was already described in section (2.4.1). In picture (3.16) the real systems from the ion and the laser side with corresponding dimension are shown.
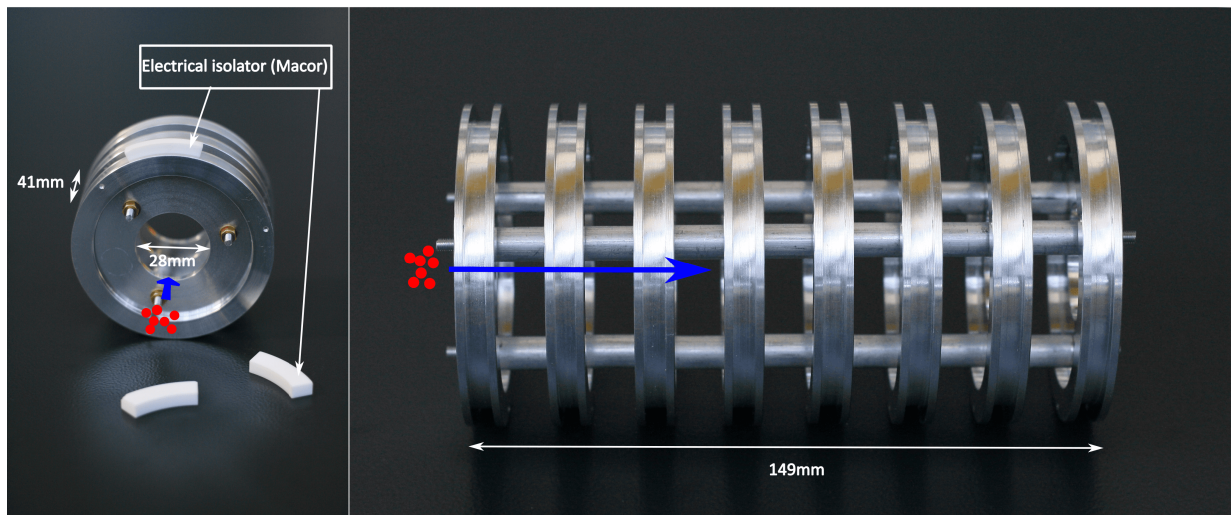
Figure 3.16.: Pictures of the CCI (left) and CCL (right) outside of the temperature shields without attached electronics.

A bunch of charged particles which flies through such a device induces an image charge in the electrode which can be picked up, amplified and detected. Depending on the geometry of the electrode, the electrical properties (most importantly the capacitance) and the size of the particle beam the signal can vary. Figure (3.16) shows a typical signal obtained by the CCI and CCL for a Ar^{13+} ion beam.
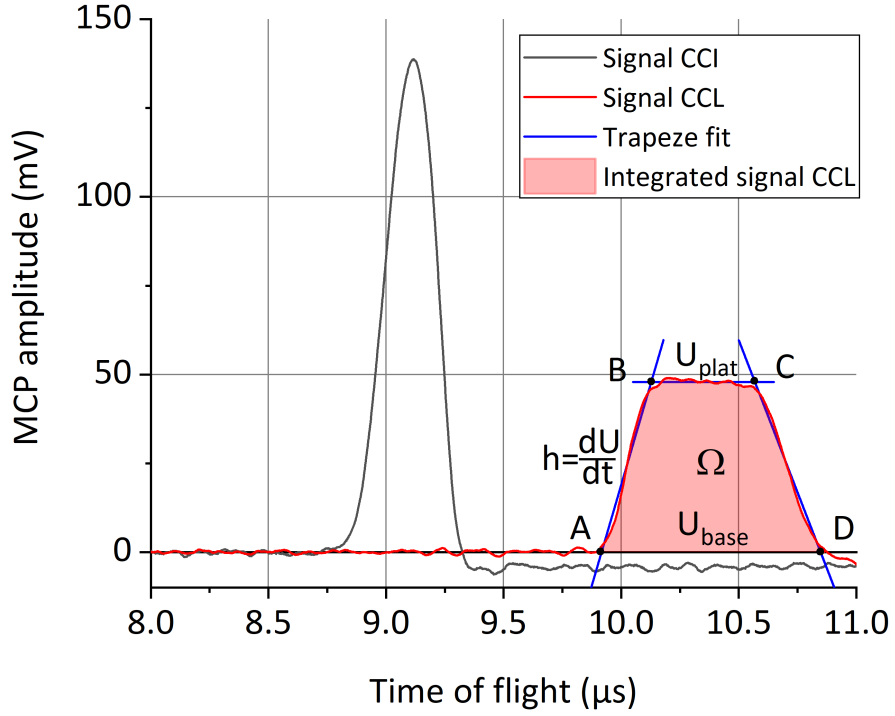
Figure 3.17.: Typical signals for both charge counters for an ion beam of Ar^{13+}. The black signal is from the CCI, while the red one is received from the CCL. The time delay between the two signals is due to the axial distance between the devices. Based on the analysis procedure described in section (2.4.1) a trapeze is fitted (blue) to the data of the CCL to extract the necessary parameters for the determination of the ion beam properties.

Since a more detailed analysis relies on the formation of a plateau, see section (2.4.1) and [42, 56], the CCL was most often used for the ion beam determination. In figure (3.17) such a signal with a plateau can be seen. A trapeze is fitted to the signal in order to extract the important quantities. The points A,B,C and D are the corners of the trapeze and define the values of U_{plat} and U_{base} and the four points t_A, t_B, t_C, and t_B respectively. In addition, $h = dU/dt$ defines the slope of the rising edge of the trapeze. The results are given in table (3.3).

Table 3.3.: Important parameters extracted from the trapeze fit.

Parameter	Value	Error
U_{plat} [mV]	47.85	± 0.05
U_{base} [mV]	0.10	± 0.03
t_A [µs]	9.92	± 0.28
t_B [µs]	10.13	± 0.29
t_A [µs]	10.57	± 0.19
t_A [µs]	10.85	± 0.20
h (slope) [mV/µs]	226.68	± 3.28

Those parameters combined with the sensitivity $S_{CCL} = (519 \pm 20)$ nV/e of the detection system and characteristic length $L_{char,CCL} = 0.1716$ m of the electrode which have been determined beforehand [57], the beam properties like particle number N given by equation (2.22), kinetic energy E_{kin} given by (2.26) and bunch length l_{bunch} given by (2.28) can be determined. The results are presented in the following table (3.4).

Table 3.4.: Determined beam properties for the presented Ar^{13+} ion beam.

Parameter	Value	Error
N [#]	7092	± 280
E_{kin} [eV/q]	995	± 23
l_{bunch} [mm]	52.6	± 6.7

The kinetic energy of the ion beam can be compared with the expected energy due to the applied central drift tube potentials U_2 of the EBIT, see section (3.1), which to first order defines the energy of the extracted ion bunch. In the case shown here it was set to $U_2 = 979$ V and hence corresponds to an energy of $E_{kin} = 979$ eV/q which is in good agreement with the value obtained from the charge counter. Additionally it becomes apparent why the CCI is not able to provide a signal with a plateau like the CCL does. Since the bunch length is about 52 mm, which is longer than the CCI with a total length of 41 mm as shown in picture (3.16), there is always a part of the beam which is either not in, or already out of the CCI. Therefore, only a part of the charge is induced and a plateau cannot be established. More details about the limitations in terms of particle number etc. and further improvements of such devices are presented in [57].

3.4.2. Ion deceleration: The pulsed drift tube (PDT)

One of the most important parts of the setup is the pulsed drift tube (PDT), which is used to decelerate the ion bunch in order to be caught by the trap electrodes. Since the ions have typical kinetic energies around $E_{kin} \approx 1000\,\mathrm{eV/q}$ a deceleration down to about 20% of their initial kinetic energy by the PDT is needed in order to be further slowed down and finally caught by the trap itself. It is the first part inside of the two temperature shields before the CCI, as shown in the drawing (3.15). The design is similar to both charge counters, although the overall length is different with a value of 89 mm. A picture of the PDT outside of the system is shown in (3.18).
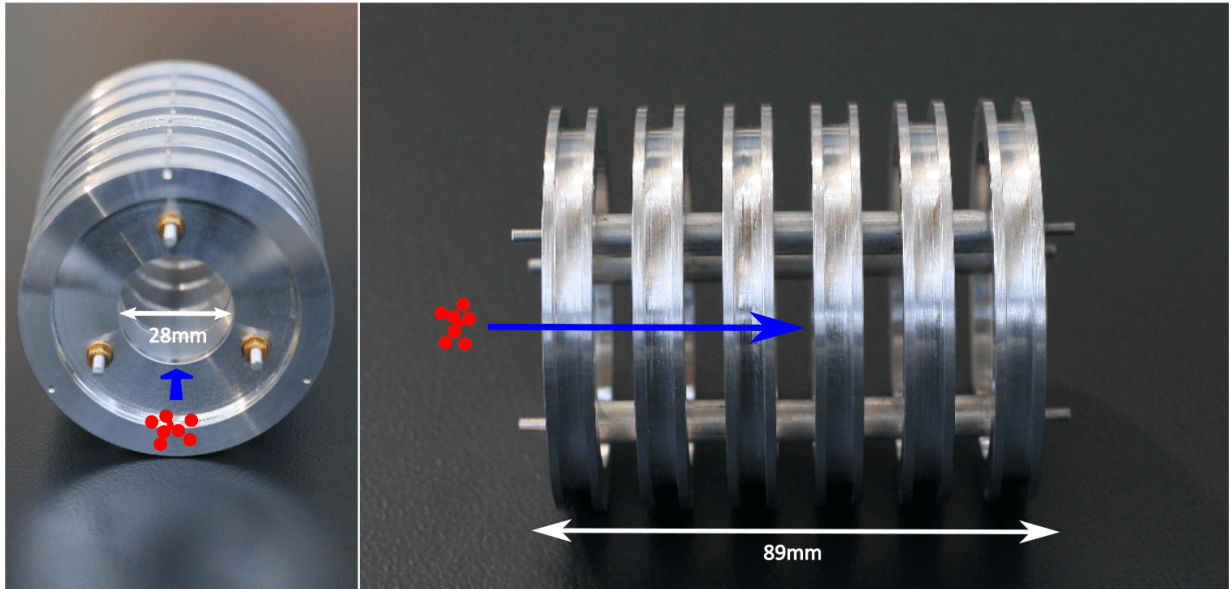
Figure 3.18.: Picture of the PDT outside of the temperature shield.

The operation principle was presented in section (2.2) and is based on fast switching from a positive to a negative voltage while the ion bunch is inside the PDT. Therefore, the efficiency is highly dependent on the switching time, and was found to be optimal at $t_{PDT} = 8.45\,\mathrm{\mu s}$ for Ar^{13+} based on the extraction point from the EBIT. The voltage was switched form $U_{PDT} = +450\,\mathrm{V}$ to $U_{PDT} = -400\,\mathrm{V}$. An exemplary result is plotted in figure (3.19).
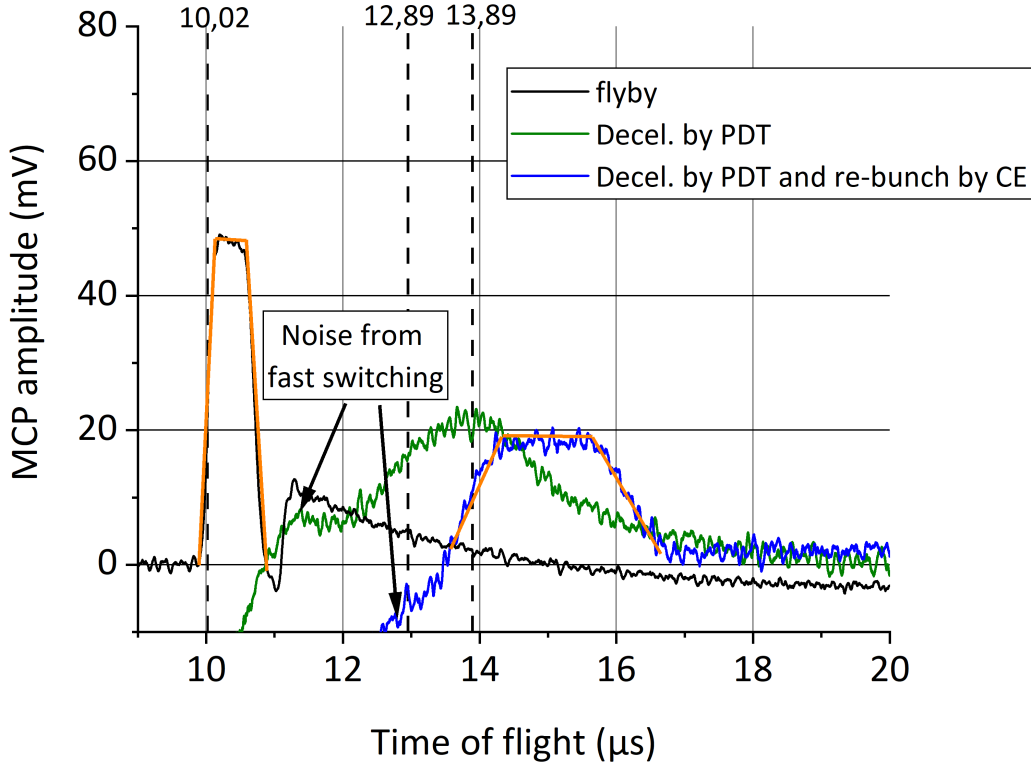
Figure 3.19.: Deceleration of an Ar^{13+} ion beam. The first signal (black) shows the un-
decelerated bunch, which just passed by. The second signal (green) demon-
strates the effect of the PDT. It was switched from $U_{PDT} = +450\,\text{V}$ down to
$U_{PDT} = -400\,\text{V}$, as described in section (2.2). It is delayed by about $2.8\,\mu\text{s}$.
From the shape it can be concluded that the bunch became elongated and a
plateau is not formed. The last signal (blue) shows the so-called 're-bunching'
effect, in which a voltage at the first trap electrode is used. The delay is
enlarged to about $3.8\,\mu\text{s}$ and a plateau is again formed, hence a trapeze fit
can again be applied.

Three different signals picked-up by the CCL are plotted. The first one (black) shows the
undecelerated signal of the bunch which just flies through the setup. Based on this, the
important bunch properties like particle number, kinetic energy and bunch length can be
extracted by the trapeze fit, as presented in (3.4.1). The second signal (green) shows the
effect of the PDT. The signal is delayed by about $2.8\,\mu\text{s}$ and deformed, so a plateau is
no longer present. The kinetic energy has therefore to be calculated by the time-of-flight
between the charge counter and the MCP detector and is about $E_{ion} \approx 180\,\text{eV/q}$. To
compensate for that the first trap electrode (Capture electrode, CE) is used as second
deceleration and 're-bunching' stage. The applied voltage for the CE was set to $+100\,\text{V}$

and switch-off was done with a delay time of $t_{CE} = 9.75\,\mu s$. Therefore, the shape can be restored and the analysis based on the plateau can be applied again. The signal is further delayed by $3.8\,\mu s$, which corresponds to an energy of $E_{ion} \approx 90\,eV/q$ by a time-of-flight analysis. If the analysis procedure of the charge counter signal (fitted trapeze) is used, one gets $E_{ion} = (89 \pm 6)\,eV/q$.

3.4.3. Ion storage: Penning trap and non-destructive detection system

After the previously described deceleration process of the ion bunch, the final step is the capture and storage of the ions inside the trap. It was already depicted in the overview picture of the magnet bore in figure (3.15), and in greater detailed now in (3.20).
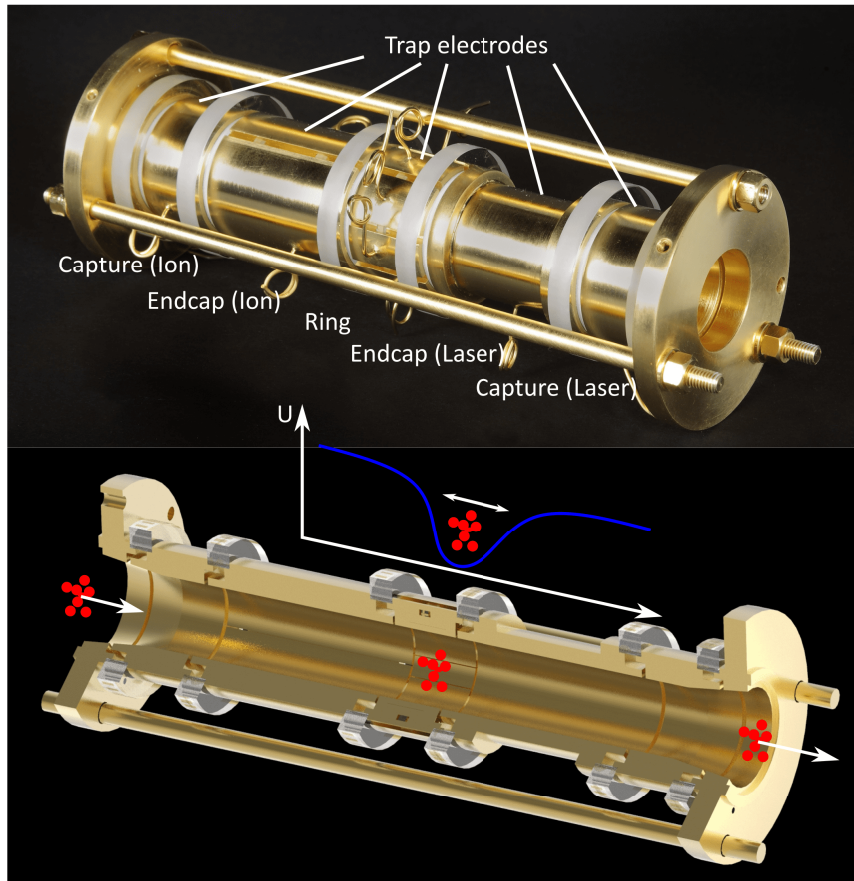

Figure 3.20.: (Top) Picture of the Penning trap electrodes without electronics and detection systems. (Bottom) Rendered CAD section view of the inside of the electrode stack and a schematic of the applied trap potential with stored ions.

It shows the gold-plated copper electrode stack of the HILITE Penning trap as a real

picture (top) and a CAD section view to show the inside (bottom). The trap consists of two capture electrodes on the 'ion' and the 'laser' side (CI, CL) for the capture and 're-bunching' process, see section (3.4.2), followed by two endcap electrodes (EC-I, EC-L) for the creation of the trapping potential. A schematic of this potential is depicted in figure (3.20) as well. The electrode on the 'ion' side is further split radially into two half-shells. By doing so, one segment serves as an excitation electrode for the axial motion of the stored ions, see section (2.3.4), while the second one works as a pick-up electrode as described in section (2.4.2) for the resonant non-destructive detection by a tuned RLC-circuit. Since both detection and excitation are AC-signals, the DC potential for the confinement in the trap is unaffected and superimposed. The central electrode, called 'ring' is further divided into eight segments ($4 \times 30° + 4 \times 60°$) for radial excitation, mode coupling and resonant non-destructive detection of the cyclotron motion (section 2.3.4, 2.4.2). For the resonant detection in the trap, tuned RLC-circuits (resonators) in close vicinity to the corresponding pick-up electrodes are needed. Two of such devices are implemented within HILITE, one for the axial (ARES) and one for the cyclotron (CRES) motion. Figure (3.21) gives an impression of that.
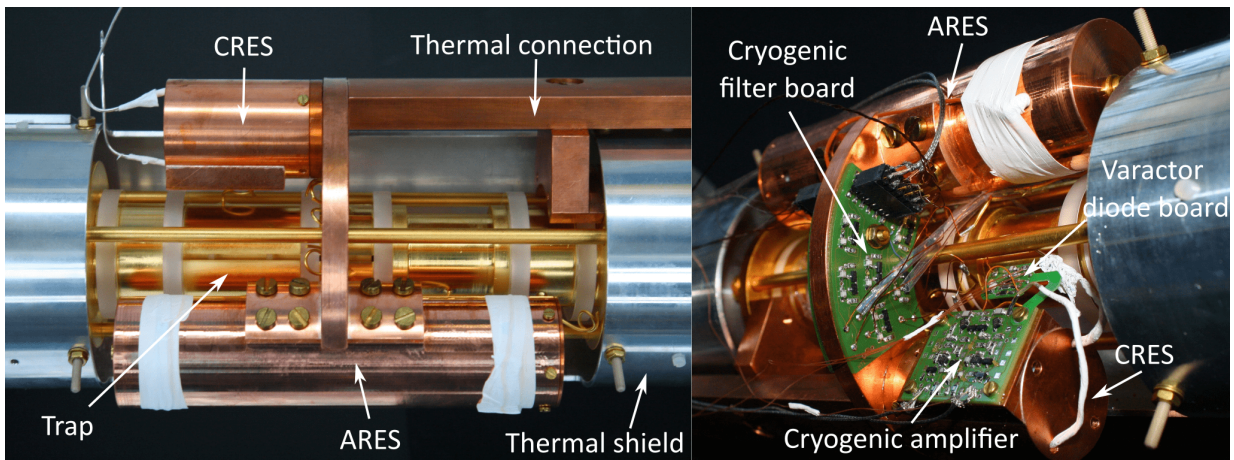
Figure 3.21.: (Left) Picture of the electrode stack placed inside the inner thermal shield and the attached tuned circuits ARES + CRES. (Right) Additional cryogenic electronics, like filterboard, amplifiers and varactor diodes are further implemented.

Both resonators are attached close to their pick-up electrode to reduce the parasitic capacitance and are thermally connected to the 4 K-stage of the setup. This ensures a thermal equilibrium with the trap and the surrounding electronics. Therefore, the background (thermal) noise can be reduced. The aforementioned electronics is depicted on

the right hand side of figure (3.21). Each resonator is equipped with a cryogenic amplifier and varactor board for tuning the resonance frequency of the circuit. All bias supply lines of the trap and electronics are AC-filtered by a dual-stage RC-low-pass ($\nu_{cutoff} = 15\,\text{kHz}$) cryogenic filter board. All signal lines (e.g. detection and excitation) are realised by coaxial wires as short as possible to reduce parasitic capacitance and enhance noise robustness. In the following both circuits will be briefly presented in terms of design and properties. A more detailed description can be found in [73].

Tuned RLC-circuit for the axial motion (ARES)

The first resonator is the one for the axial motion of the ions (ARES). It is connected to one of the half-shells of the split endcap electrode on the ion side (EC-I) to pick up the signal of the ions while they oscillate in the trapping potential (section 2.4.2). The design frequency of the circuit has to be chosen roughly beforehand based on the motional frequency of the ions of interest (carbon and oxygen) and was found for HILITE to be at $\omega_0 = 2\pi \times 457\,\text{kHz}$. Since ω_0 depends on L and C which are highly sensitive to the manufacturing process, material properties, temperature etc., the actual setup of such a device is quite challenging. Therefore, the tuning towards the final frequency is later on achieved by adjusting the voltage of an attached varactor diode board which changes the overall capacitance and therefore the frequency as explained already in section (2.4.2).
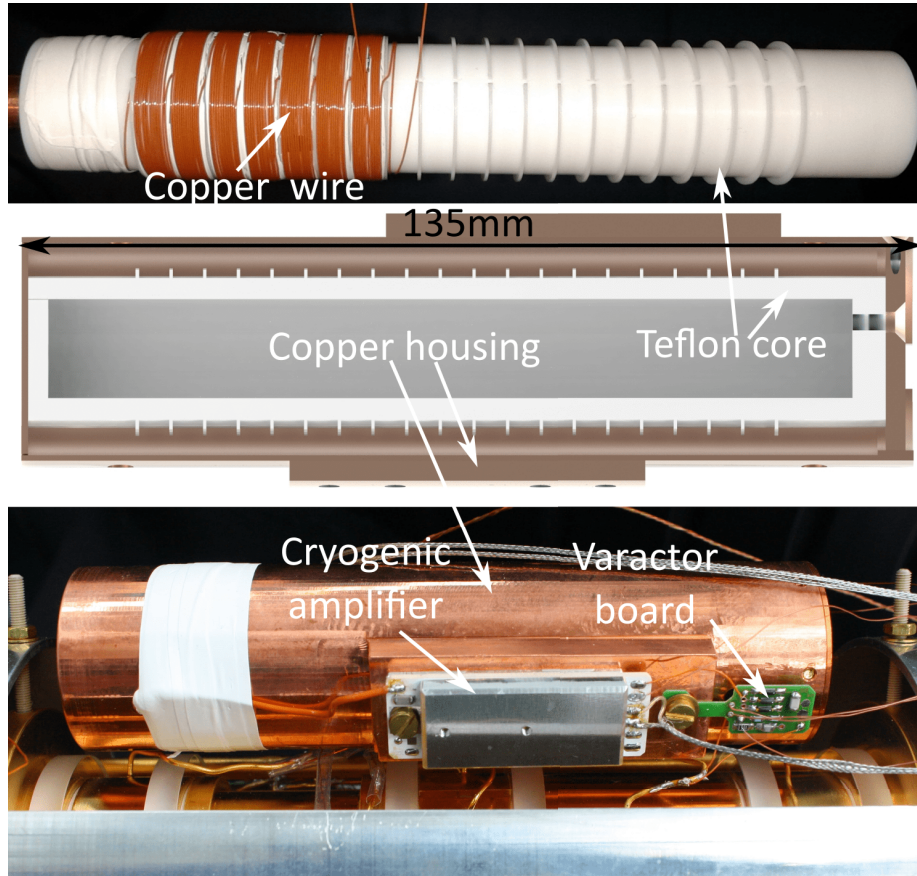
Figure 3.22.: (Top) Multilayer coil winding on the PTFE core. (Centre) CAD section view of the ARES. The PTFE core placed in the centre of the copper housing is shown. (Bottom) Picture of ARES attached to the trap including amplifier and varactor diode board.

The ARES of HILITE has a helical geometry based on multilayer coil design with four layers and 1200 turns in total on a PTFE (Teflon) core, see figure (3.22). The overall length of the copper housing is 135 mm and has a diameter of 33 mm. From equation (A.3) the inductance of such a coil can be calculated and is about $L_{ARES} \approx 4.5$ mH. The capacitance can be estimated likewise by equation (A.4) to be $C_{ARES} \approx 27$ pF. A varactor diode board equipped with three varactor diodes placed in parallel is connected to the coil, increasing the total capacitance by $C_{var} = 6 - 24$ pF depending on the applied voltage, (see figure 3.22). Additionally, a low-noise cryogenic amplifier from *Stahl electronics* is capacitively coupled to the ARES, see figure (3.22) before the signal is forwarded by a coaxial wire to an electrical feedthrough flange. The overall properties of the ARES and more details about the varactor board and the amplifier are given in table (A.1) in the appendix. From equation (2.8) it

follows that the motional frequency of the ions, besides the intuitive $\sqrt{q/m}$-dependency, has an additional dependency on the applied trap potential U_0. The most common way of operation is therefore to fix the resonance frequency ω_0 of the circuit and change the motional frequency of the ions ω_z by ramping the trap voltage U_0. Thereby, different ion species with q/m-ratio corresponding to the applied voltage are successively in resonance with the circuit, however the trap depth should not fall below a lower limit of around twice the axial energy to avoid particle losses. Characteristic measurements regarding resonance frequency ω_0, quality factor Q (width at $-3\,$dBm) and frequency tuning capability $\Delta\omega_0$ due to the varactor diodes are presented in figure (3.23).
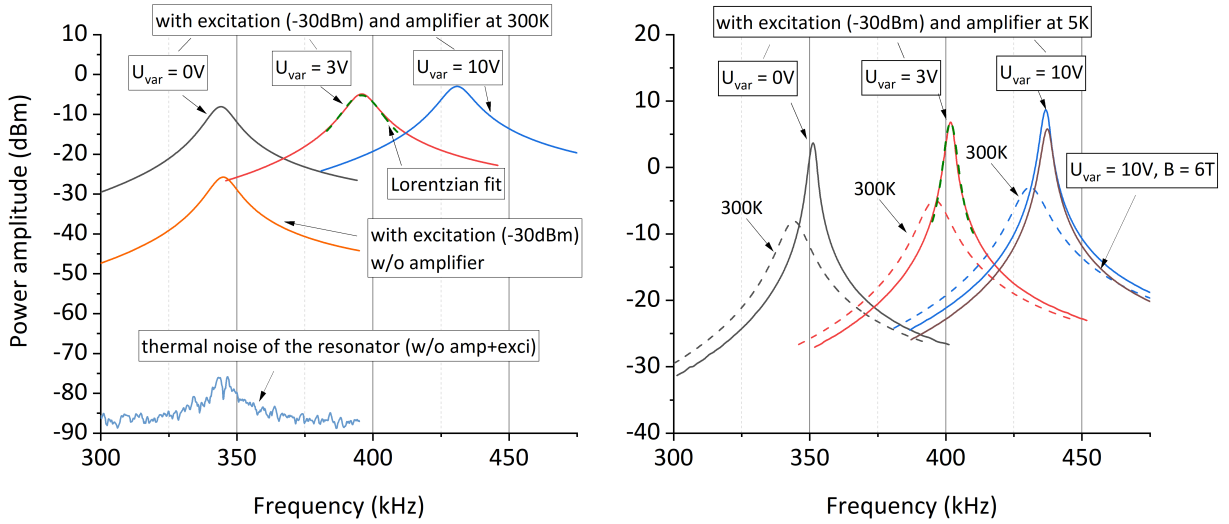
Figure 3.23.: (Left) Spectral response of the ARES circuit at $300\,$K for different varactor voltages. (Right) Corresponding spectral response for cryogenic conditions of $5\,$K. The $300\,$K curves are still present as dashed lines. Exemplary Lorentz fits are shown in both figures, as well as a response for an external magnetic field of $B = 6\,$T.

The measurements have been performed at room temperature ($300\,$K) and cryogenic temperature ($5\,$K), respectively, for different varactor diode voltages ($0\,$V, $3\,$V, $10\,$V). The spectral response of the circuits have been picked-up by a spectrum analyser *Keysight N9000B CXA* with an integrated tracking generator used for the excitation ($-30\,$dBm). For comparison, the intrinsic thermal noise of the system without excitation and amplifier was measured as well. By fitting of a Lorentzian-shape function the frequency as well as the quality factor can be extracted. The results are presented in table (3.5).

Table 3.5.: ARES characteristics.

T (K)	ω_0 $(2\pi \times \text{kHz})$			$\Delta\omega_0$ (kHz)	Q
	$U_{var} = 0\,\text{V}$	$U_{var} = 3\,\text{V}$	$U_{var} = 10\,\text{V}$		
300	344.1	395.9	430.9	86.8	42
5	351.2	401.7	436.7	85.5	122

Between $300\,\text{K}$ and $5\,\text{K}$ a slight overall increase of the resonance frequency ω_0 is observed mainly caused by small geometric displacements of the coil and the housing due to different thermal expansion coefficients. The tunability is constant and around $\Delta\omega_0 \approx 85\,\text{kHz}$. The quality factor increases significantly by a factor of three to $Q = 122$. This is due to an increase in electrical conductivity at lower temperatures and hence a smaller resistance series resistance. Since the resonator acts as a parallel circuit (see equation 2.31), the effective parallel resistance increases and therefore the quality factor increases as well. The difference of the quality factor between different varactor voltages is negligible. In addition, at $T = 5\,\text{K}$ a measurement including a magnetic field of $B = 6\,\text{T}$ was performed since at room temperature an effect could not be observed. A small drop in signal strength, as well as a slight increase in frequency towards $\omega_0 = 437.3\,\text{kHz}$ can be seen.

Tuned RLC-circuit for the cyclotron motion (CRES)

The second tuned circuit is the one for the perturbed cyclotron motion ω_+ (see section 2.3.2) of the stored ions. From equation (2.9) and (2.10) it follows that the frequency is mainly determined by the magnetic field and around two orders of magnitude larger than in the axial case ($\omega_+ \approx 2\pi \times 30\,\text{MHz}$) for the field strength of $B = 6\,\text{T}$ and target species of carbon, oxygen and argon. Since the capacitance is somehow limited to several pF, the inductance of the coil has therefore to be lowered significantly to increase the resonance frequency of the circuit. This is achieved by a much smaller number of turns and hence a more compact design as depicted in figure (3.24).
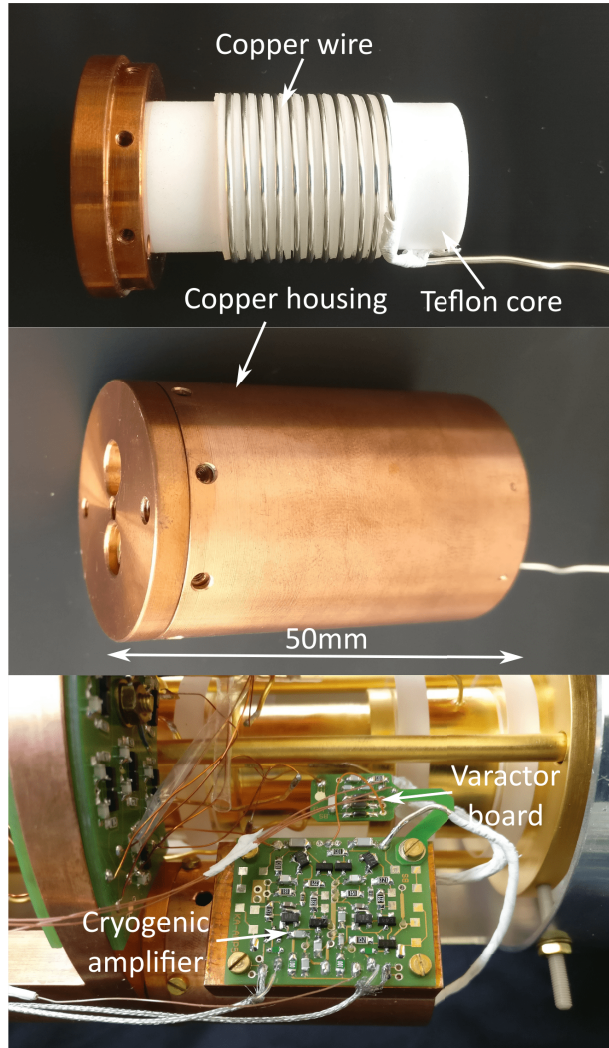
Figure 3.24.: (Top) Coil winding on the PTFE core. (Centre) Picture of CRES housing with coil placed inside. (Bottom) Picture of CRES attached to the trap including amplifier and varactor diode board.

The CRES circuit is a helical, single-layer design with a total number of turns of 10 for the coil. It is made out of silver-plated copper wire on a PTFE core placed in a 50 mm long and 32 mm in diameter large copper housing (outer dimension). The inductance can be calculated by using equation (A.2) to be $L_{CRES} \approx 1\,\mu\text{H}$ and likewise the capacitance with equation (A.4) to be $C_{CRES} \approx 17\,\text{pF}$. Like in the ARES-case a low-noise cryogenic amplifier from *Stahl electronics* is directly attached to the CRES-housing (see figure 3.24) to minimise the parasitic capacitance further. Additionally, a second varactor diode board ($C_{var} = 6 - 24\,\text{pF}$) based on the design of the ARES is attached, to shift the resonance frequency accordingly. Since the magnetic field cannot be changed that easily as the trap

voltage, the applied voltage on the varactor diodes will bring the circuit into resonance with the stored ions. In table (A.1) in the appendix, the overall details of the circuit are mentioned. Like in the ARES-case, the same characteristic measurements of the spectral response of the circuit have been performed and are shown in figure (3.25).
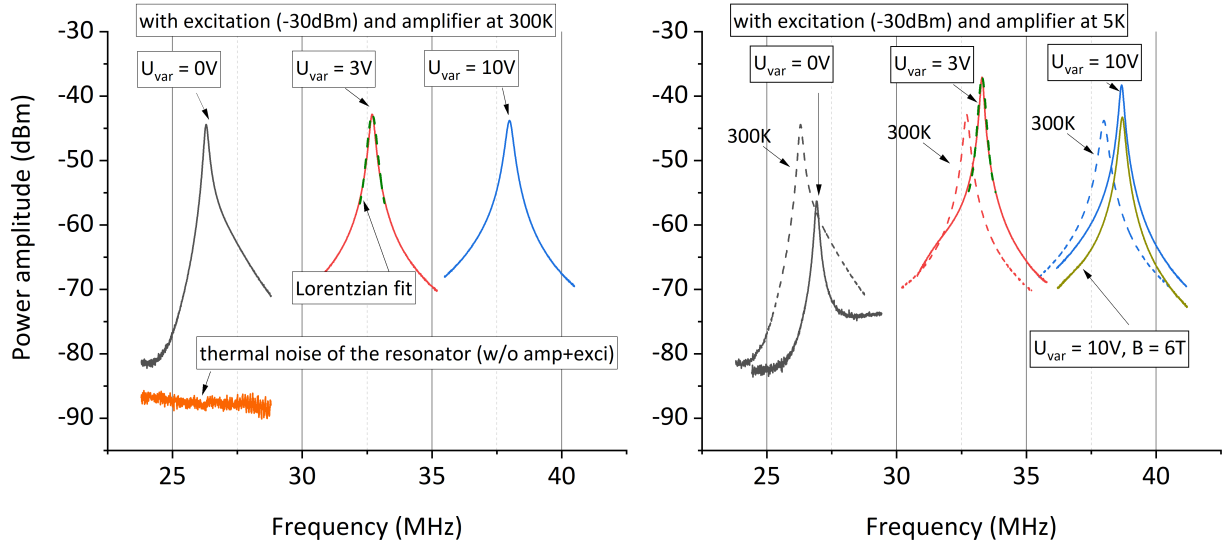
Figure 3.25.: (Left) Spectral response of the CRES circuit at $300\,\mathrm{K}$ for different varactor voltages. (Right) Corresponding spectral response for cryogenic conditions of $5\,\mathrm{K}$. The $300\,\mathrm{K}$ curves are still present as dashed lines. Exemplary Lorentz fits are shown in both figures, as well as a response for an external magnetic field of $B = 6\,\mathrm{T}$.

The fitted Lorentzian provides again the properties like resonance frequency and quality factor. They are extracted and given in table (3.6).

Table 3.6.: CRES characteristics.

T (K)	ω_0 $(2\pi \times \mathrm{MHz})$			$\Delta\omega_0$ (MHz)	Q
	$U_{var} = 0\,\mathrm{V}$	$U_{var} = 3\,\mathrm{V}$	$U_{var} = 10\,\mathrm{V}$		
300	26.30	32.70	37.99	11.69	160
5	26.91	33.29	38.67	11.76	220

While like in the ARES-case the tunability is not affected by the temperature and stays around $\Delta\omega_0 \approx 11.7\,\mathrm{MHz}$, the resonance frequency is slightly shifted towards higher frequencies. The same argument of small geometric displacements due to thermal contraction holds true here as well. Likewise the quality factor, although the overall increase is not as

much as in the previous case. Adding a magnetic field has the same effect as for the ARES. The signal amplitude drops a bit, while the frequency increases to roughly $\omega_0 \approx 38.70\,\mathrm{MHz}$.

3.4.4. Ion detection: Non-destructive resonant detection

The previously described circuits fulfil two purposes at once. First, the non-destructive detection of ions in the trap by induced and amplified image charges (see section 2.4.2), and at the same time to cool those ions by damping the induced currents, called 'resistive cooling' (see section 2.3.5). In our case, the ions (C^{2+}) have been externally produced, transported, decelerated and captured in the trap as described in the previous part of the thesis. They have been trapped at a potential of $U_0 = 45\,\mathrm{V}$. Since it is much easier to scan for the axial resonance of the ions due to the trapping voltage dependency (see equation 2.8), the ARES is mainly used for detection and cooling purposes. The expected axial frequency of C^{2+} for $U_0 = 45\,\mathrm{V}$ is $\omega_z = 2\pi \times 416\,\mathrm{kHz}$. So, ARES was tuned to be at $\omega_0 = 2\pi \times 416\,\mathrm{kHz}$. Therefore the varactor diode voltage was set to $U_{var} = 4.52\,\mathrm{V}$. After the capture process, a voltage ramp from $U_0 = 40\,\mathrm{V}$ to $U_0 = 52\,\mathrm{V}$ and backwards in steps of $\approx 0.24\,\mathrm{V}$ was performed. Each ramp took about $100\,\mathrm{s}$, and in total five of them have been carried out. The results are depicted in figure (3.26).
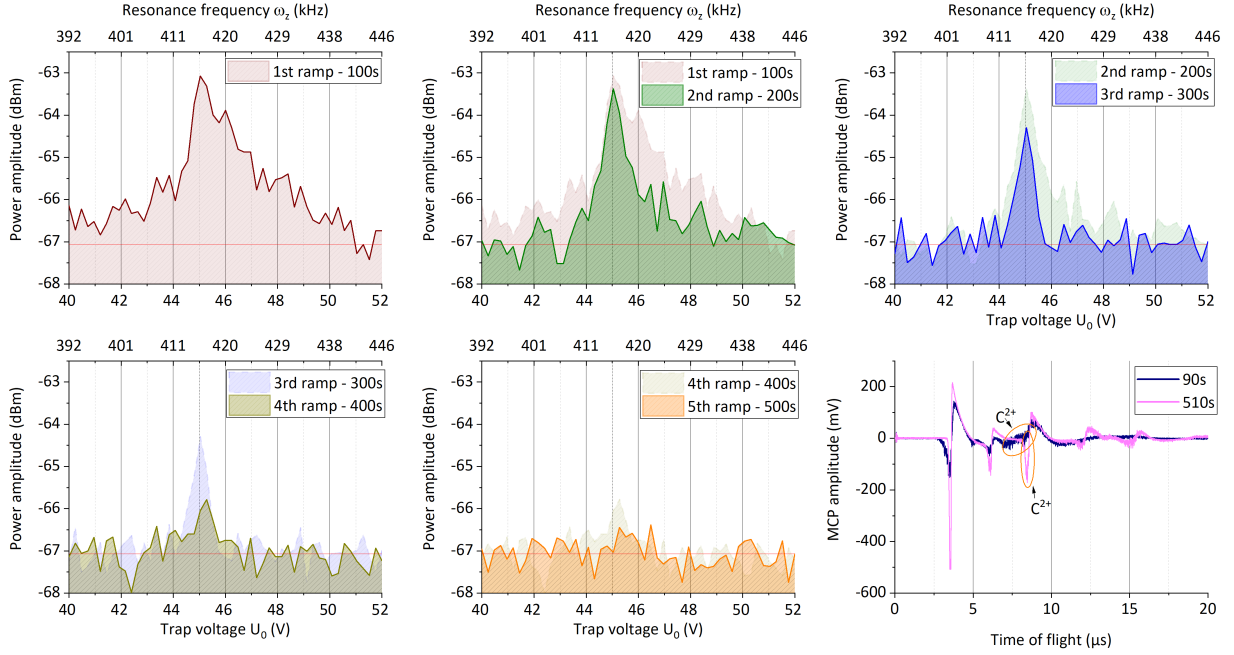
Figure 3.26.: Measurement sequence of C^{2+} ions in the trap. From left to right and top to bottom five consecutive voltage ramps of the trapping potential between $U_0 = 40\,V$ and $U_0 = 52\,V$. The circuit was tuned to be in resonance with the ions at $\omega_0 = 2\pi \times 416\,kHz$ for a trapping potential of $U_0 \approx 45\,V$ by an applied varactor voltage of $U_{var} = 4.52\,V$. The last graph (bottom right) shows the corresponding ion signal of the MCP detector of the extracted ions for storage times of $90\,s$ and $510\,s$. Although the resonator does not show an ion signal after the 5th ramp anymore, C^{2+} is still apparent.

For a trap voltage of around $45\,V$, a peak can be identified which is rather broad and asymmetric ($44\,V - 50\,V$). This can be explained by an initial high axial energy of the ions after trapping. Since they are externally produced and although they are decelerated, the remaining energy can easily be still in the range of $E_z = 10 - 20\,eV$ which corresponds to an amplitude of several millimetres. Therefore, they leave the harmonic region of the confinement volume which results in higher axial frequencies than expected. This effect causes the asymmetry of the resonance towards higher frequency and can clearly be seen in the first plot. In addition, the energy distribution of the ion cloud leads to a generally broad resonance. During the second and the third ramp, the peak becomes much narrower (tails are gone) and the amplitude drops slightly. This can be explained by a cooling process which occurs in the meantime. By a reduction of the mean axial kinetic energy, the amplitude of the motion drops and the ions oscillate in the harmonic region of the trap. Therefore their frequency is in the first order independent of the amplitude. During the

next ramp the signal drops further and is gone for the last ramp, after about $500\,\mathrm{s}$. A loss of ions can be excluded, since they can still be detected after extraction onto a destructive (MCP) detector as shown in the bottom right figure of picture (3.26). The disappearance is mainly due to the spectral noise of the system (circuit, amplifiers etc.), indicated by a red horizontal line at about $-67\,\mathrm{dBm}$. Once the ions have reached this level, they are in thermal equilibrium with the circuit and cannot be distinguished from the background [48].

3.4.5. Ion detection: Destructive detection by time-of-flight analysis

The second option to characterise and determine the composition of the trap content is to extract the stored ions and transport them onto a multi-channel plate (MCP) detector, as depicted in figure (3.15). By a time-of flight (ToF) analysis as it was used for the characterization of the EBIT content (3.1.2) one uses the $\sqrt{m/q}$-dependency (see equation 3.1) to identify the different ion species and charge states. Since the travelled distance is much shorter than in the EBIT-case and the stored ions are basically 'at rest' in the trap, the resolution can be quite challenging. Therefore one uses the concept of 'floating ground', in which the complete trap is 'floating' at a potential of $U_{float} = 50\,\mathrm{V}$ in relation to ground, as shown in figure (3.27).
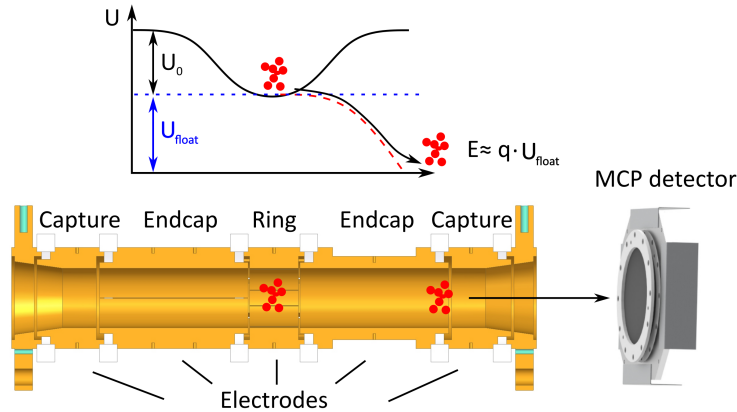
Figure 3.27.: Schematic of the 'floating ground' principle. The complete trap with all electrodes is set to a floating potential ($U_{float} = 50\,\mathrm{V}$). Thereby, the extracted ions gain an additional kinetic energy of $E_{float} \approx q \cdot 50\,\mathrm{eV}$. Typically their kinetic energy while stored is much less $E_z \ll E_{float}$, so their time-of-flight is in first order given by E_{float} and a time-of-flight analysis can be applied more easily.

Once the extraction is performed, the ions gain an energy of those $E_{float} \approx q \cdot 50\,\mathrm{eV}$ in

addition to their axial energy E_z. Since they have been cooled in the trap beforehand one can assume $E_z \ll E_{float}$ and their time-of-flight is in first order given by E_{float} only. For this measurement, C^{2+} ions have been stored inside the trap. Instead of detection by the tuned RLC-circuit as described in the previous section (3.4.4), the ions have been extracted onto the MCP detector after different storage times. The signals obtained are depicted in figure (3.28).
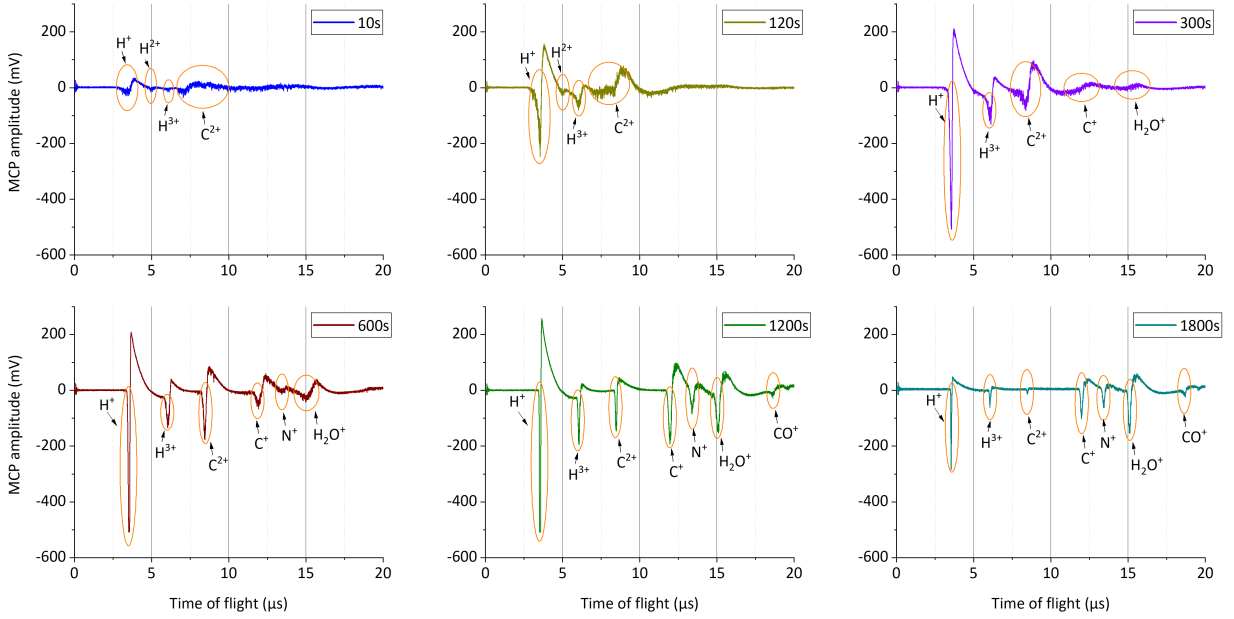
Figure 3.28.: From top left to bottom right a measurement sequence of extracted ions from the trap for different storage times. Previously, C^{2+} ions have been decelerated and stored.

The signal after a storage time of 30 s is rather blurred and consists of many tiny 'peaks' distributed over a long time period. One can identify four areas with larger amplitudes corresponding to the stored C^{2+} ions, and three hydrogen species (H^+, H_2^+, H_3^+,). Those areas become more pronounced the longer the storage time. The blurriness vanishes, especially C^{2+} becomes sharp and its amplitude increases until around 600 s of storage before it becomes smaller. It is worth noting that although it seems to be that the amount of C^{2+} increases this is not the case as the right picture in figure (3.29) shows. Due to a cooling process, the total energy and energy distribution reduces, leading to narrow and sharp peak. At around 300 s the decay towards C^{1+} can be identified together with other residual gas components like N^+, H_2^+ and CO^+. The amplitude of C^{2+} drops significantly after 600 s and is almost gone after half an hour of storage time (1800 s). Once gone, the

amount of other species drops as well, since their primary source (C^{2+}) is gone. Hydrogen overall is the most prominent residual gas present in the trap. It outgases from the chamber walls (stainless steel) since most of them cannot be baked out (temperature-sensitive devices like the magnet bore etc.). A typical appearance is the hydrogen molecule H_2^+. It becomes dissociated to atomic hydrogen due to the high energy of C^{2+}. H_3^+ or 'protonated molecular hydrogen', which is actually one of the most abundant ions in the universe, requires low temperatures and pressures to form - as is the case in a typical Penning trap. The remaining components are expected in a typical residual gas spectra, especially for a target gas of CO_2 used in the EBIT.

The identification of the species is then finally done by a time-of-flight analysis as already explained and applied for the EBIT characterisation (section 3.1.2) and earlier in this part. The results are presented in the left picture of figure (3.29) and show a good agreement with the expectation and verify the assignment.

The evolution of the different species over time allows further to conclude about the residual gas pressure in the trap. Typically stored ions collide with the residual neutral gas and decay to lower charge states, as charge exchange occurs during the collisions. The lifetime of the species can therefore be used as an estimation of the background pressure, since higher background leads to more collision and hence a shorter lifetime. In our case the species of interest is C^{2+}, which collides with hydrogen being the most prominent background species. The decay is expected to follow an exponential behaviour of the form

$$N_1 = N_0 \cdot \exp(-\frac{t_{ion}}{t}) \tag{3.2}$$

in which t_{ion} is the lifetime constant of the charge state and N_1, N_0 the number of ions at time t and at the start $t = 0$. The ions' lifetime t_{ion} is given by

$$t_{ion} = \frac{1}{\sigma p} \sqrt{\frac{k_B T \mu_m}{3}} \ \text{[32]} \tag{3.3}$$

with σ being the electron capture cross section, p the residual gas pressure, T the temperature and μ_m the reduced mass of the target and residual gas. The simplest model describing electron capture processes is the 'Classical Over-the-Barrier Model' (CBM) [32], in which the cross section is expressed by

$$\sigma = \frac{1}{2}\pi R_C^2, \tag{3.4}$$

with the effective collisional radius R_C given by

$$R_C = \frac{27.2 a_0 (2\sqrt{q/e} + 1)}{I}. \tag{3.5}$$

Here, a_0 is the Bohr radius given in metres, e the elementary charge and I the ionisation potential of atomic hydrogen in eV. The results obtained for C^{2+} for different storage times are presented in the right picture of figure (3.29).
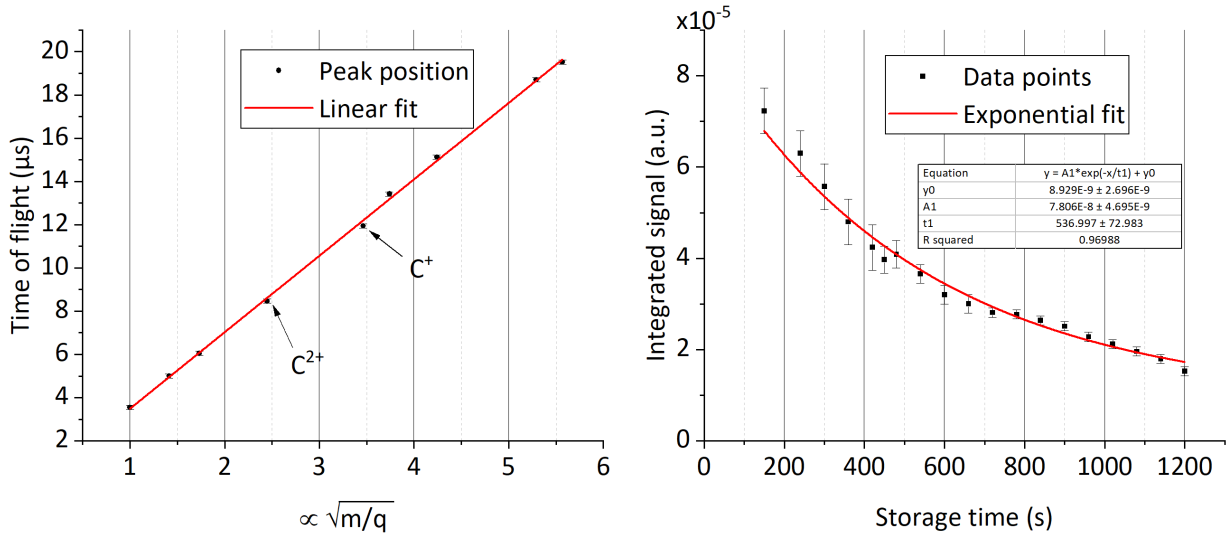
Figure 3.29.: (Left) Peak position and corresponding linear fit to identify the ion species and charge states presented in figure (3.28). (Right) Evolution of the C^{2+}-signal as a function of storage time and corresponding exponential fit. By that, the lifetime of C^{2+} in the trap and the residual gas pressure can be estimated.

An exponential decay was fitted to the data to extract the ions lifetime to be

$$t_{ion} = (537 \pm 73)\,\text{s}. \tag{3.6}$$

By rearranging equation (3.3) the residual gas pressure in the trap can be estimate to be

$$p \approx 1 \cdot 10^{-10}\,\text{mbar}. \tag{3.7}$$

assuming an ionisation potential $I = 13.9\,\text{eV}$ for atomic hydrogen and a temperature of the residual gas of around $300\,\text{K}$. This pressure is one to two orders of magnitude lower than the values the pressure gauges further away attached to the chambers are showing. This can be explained by the cryogenic environment of the trap electrodes which improves the

pressure by the so-called 'cryogenic pumping' technique in which most of the residual gas freezes out at the cold surfaces of the trap.

4. HILITE beamtime at FEL facility

This chapter is about the first beamtime HILITE performed at a dedicated high-intensity laser - the free electron laser FLASH at the DESY campus in Hamburg. I will give a short overview about the facility itself, the measurement proposal for that beamtime as well as the transport and operation of HILITE at FLASH. Finally, I will conclude with the measurements and results we obtained during the beamtime and future aspects which have to be incorporated.

4.1. FLASH @ DESY
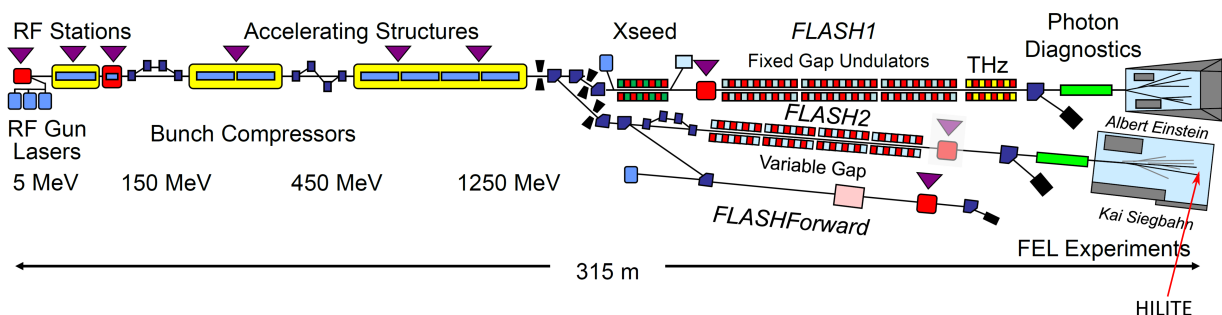
Figure 4.1.: Schematic layout of the FLASH facility. Electron accelerator and the two FEL lines FLASH 1 and FLASH 2 are shown. From [74] - modified. The position of HILITE within the beamtime is highlighted.

The FLASH facility, in operation since 2005 was the first free-electron laser (FEL) worldwide in the XUV and soft X-ray regime [74]. As described already in section (1.2), electrons in a FEL are accelerated up to relativistic velocities and forced on sinusoidal-like trajectories by a consecutive arrangement of dipole magnets with alternating polarity, which is called undulator. It defines the energy of the thereby created synchrotron radiation. FLASH consists of two individual FEL lines FLASH 1 and FLASH 2 with separated undulators as depicted in figure (4.1). Both are fed by the same linear FLASH accelerator which can provide electrons with energies up to $E_e = 1.25\,\text{GeV}$ at a $10\,\text{Hz}$ repetition (burst) rate. The

pulses of such bursts are shared between the two lines, which allows for a parallel operation [74]. The major difference between the two lines is the variable gap of the undulators in case of FLASH 2 . Thereby, the energy of the photons can be adjusted and tuned over a wide range without influencing the operation of FLASH 1. Pulses shorter than 100 fs and focal spot sizes smaller than 20 µm lead to peak intensities of up to 10^{16} W/cm² [74].

In addition, both beamlines of FLASH 2 (FL24 and FL26) offer the possibility to scan the photon energy by adjusting the gap between the undulators. Furthermore, at beamline FL24 a KB (**K**irkpatrick-**B**aez) active optics system is installed that allows a micro-focus of the FEL pulses both vertically and horizontally [75]. This is of particular interest, since ionisation experiments inside a Penning trap need the largest possible overlap between ion cloud and laser focus in order to enhance the signal-to-noise ratio. Other important parameters of FLASH 2 and beamline FL24 are given in table (A.4) of the appendix.

4.2. Beamtime proposal – Measurement goals

The beamtime proposals for FLASH are reviewed and rated. In this process the submitted HILITE proposal to perform the '*Background-free measurement of multi-photon absorption and transition-isolated excitations in simple ionic systems*, as shown by a cutout of the original application in figure (4.2), was given the highest rating.
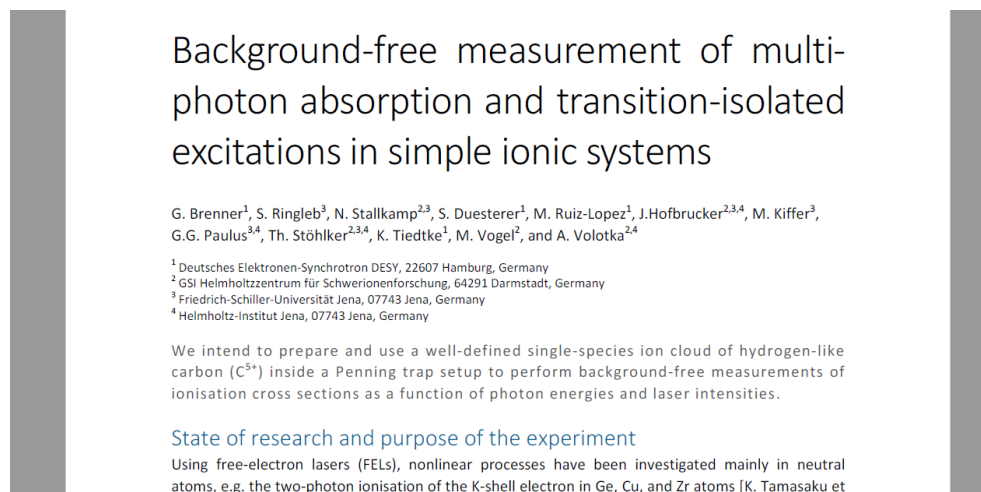

Figure 4.2.: Cutout of the beamtime proposal of HILITE for the FEL facility FLASH.

Two major objectives were pursued:

- General feasibility of laser-ionisation processes of trapped ions at high laser intensities and a subsequent storage and detection of the reaction products.

- Measurement of the energy-dependent photo-ionisation cross-section of highly charged ions.

While the first one is a more technical objective, the second one is of high physical interest since experiments in the XUV and soft X-ray regime have mainly been performed with neutral atoms [76]. They typically have to deal with obstructions by background due to interaction processes with outer electrons. Thus, the theoretical description is challenging and not well understood either [77]. It can vary by orders of magnitude [78] depending on the used model, target selection and laser system.

4.2.1. Ion target of interest - lithium-like oxygen (O^{5+})

The ion target of interest is lithium-like oxygen, O^{5+}. It has a closed K-shell with two 1s-electrons and an open L-shell with a 'single active' 2s-electron with an ionisation potential of $I_P = 138\,\text{eV}$. 'Single active' means that in order to access the inner K-shell by incident photons a much higher potential of $I_P \approx 700\,\text{eV}$, and hence photon energy is needed, so the probability is strongly suppressed. This also results in an easier description by theory, since effects by remaining electrons are of minor importance.
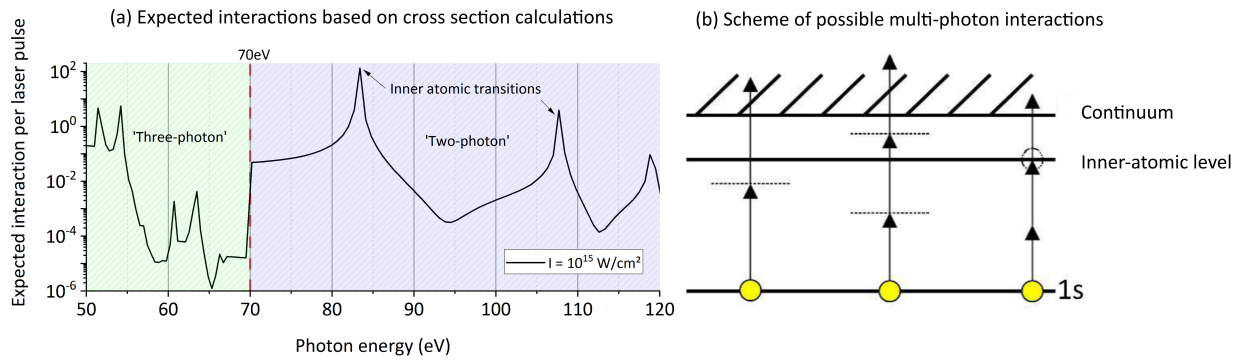
Figure 4.3.: (a) Expected interactions per laser pulse for different photon energies and laser intensities, based on theoretical calculations [79]. (b) Scheme of possible multi-photon interactions.

Based on strong-field approximation (SFA) [80] calculations performed by our colleagues [79], the expected number of interactions per laser pulse as a function of photon energy E_γ and laser intensity I can be estimated. The results are plotted in figure (4.3 (a)). The

transition between a three-photon and two-photon ionisation is marked with a dotted red line at $E_\gamma \approx 70\,\text{eV}$. The resonances occurring are due to inner-atomic transitions which are addressed by the laser for specific photon energies, for instance the 1s-2s transition. Figure (4.3 (b)) shows schematically those possible multi-photon absorption effects from left to right two-photon, three-photon absorption and inner-atomic excitation with subsequent absorption. All of them can be addressed by the FLASH FEL and are apparent in the calculations presented in figure (4.3 (a)).

4.2.2. Ion target of interest - beryllium-like carbon (C^{2+})

The second ion target was chosen to be C^{2+} for the purpose of finding a good overlap between the ion cloud and the laser focus. The reasons for C^{2+} were on the one hand the experiences we gained during our 'offline'-tests (only the Penning trap without a laser) back at GSI, which have been presented in the previous chapter (section 3.4.4 and 3.4.5) and the other hand the easy accessibility (high ionisation cross section) by the FEL. Thereby a large fraction of the ion cloud is expected to be ionised by a single bunch and the signal of created C^{3+} is supposed to be seen easily. A schematic of this process is depicted in figure (4.4).
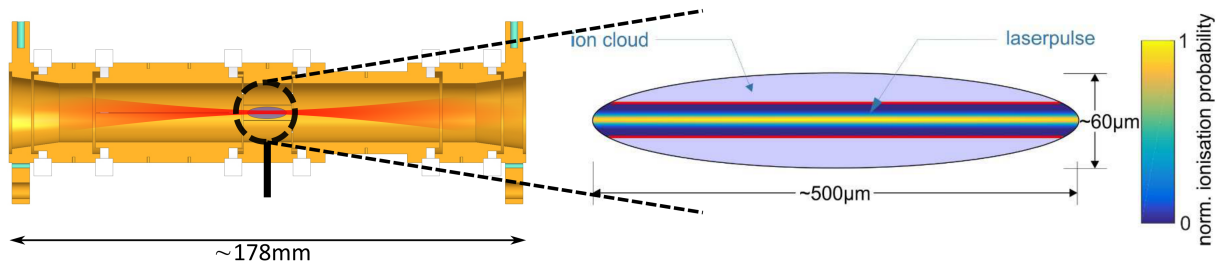
Figure 4.4.: (Left) Overlap between ion cloud and laser pulse. The position of the focal spot of the laser has to match with the position of the ion cloud. (Right) Depending on the intensity profile of the laser the probability of ionisation is a function of the relative position between the laser and the ion cloud (right picture).

4.3. Transport and operation of HILITE @ FLASH

One, if not the most important feature of the HILITE Penning trap is its possibility to be disassembled and transported rather easily to different laser facilities in order to perform photo-ionisation experiments on site. In the previous chapter, a picture (3.1) of

the assembled setup at GSI is shown. The whole process of disassembly, transport and re-assembly of the experiment at FLASH was performed in roughly one month and one has to emphasize that planning and execution was performed by ourselves without any external support.

Once arrived, the reassembly of the setup and connection to the FL24 beamline of FLASH 2 was started. The overall process took about two weeks, in which the experiment was pre-adjusted mechanically by adjustable feet in a way that the alignment laser of the beamline (which is supposed to imitate the FEL pulse) is superimposed with the Penning trap centre, both axially and radially. After that, the following parts (downstream - seen from the perspective of the laser) like ions diagnostic chamber (section 3.3.2), 90°-deflector (section 3.3.1), Wien filter (section 3.2) and ion source (section 3.1) have been installed. After closing the whole setup, the pumps and cooling were started and the individual parts were put back into operation. An impression of the final, assembled state is shown in figure (4.5)
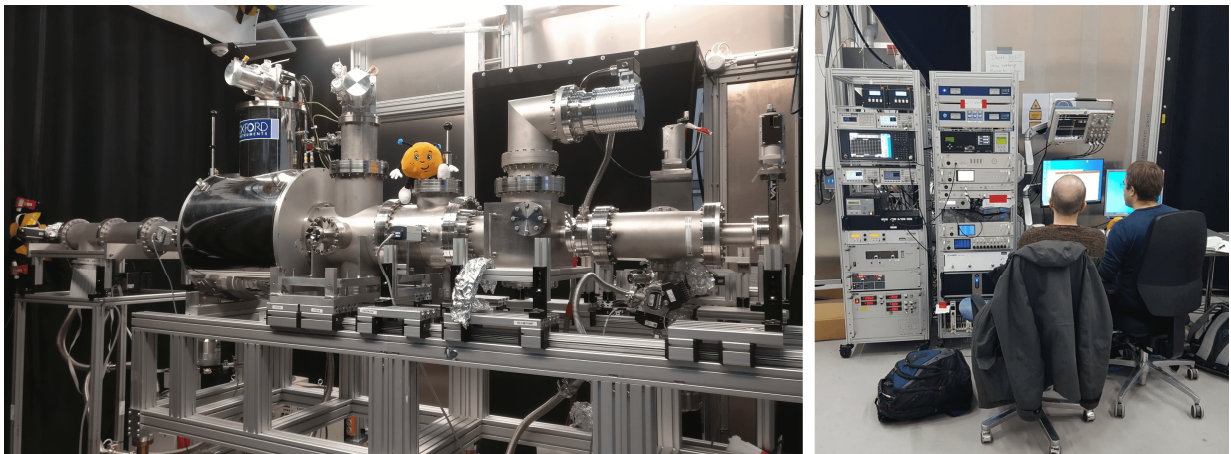
Figure 4.5.: Assembly of HILITE @ FLASH (left picture) and restart of the setup (right picture).

Before the actual beamtime started, the operation of HILITE had to be verified and the parameters for ion production, selection, transport, deceleration, capture and storage had to be found for the targets of interest (C^{2+}, O^{5+}), based on the experiences and values obtained back at GSI. Those parameters are given in table (A.5) in the appendix. The results are presented in picture (4.6). The left part shows the signal obtained by the MCP detector of an extracted and previously stored C^{2+} ion cloud, while the right one shows a corresponding signal of O^{5+}. The storage time for both ions clouds was 50 ms.
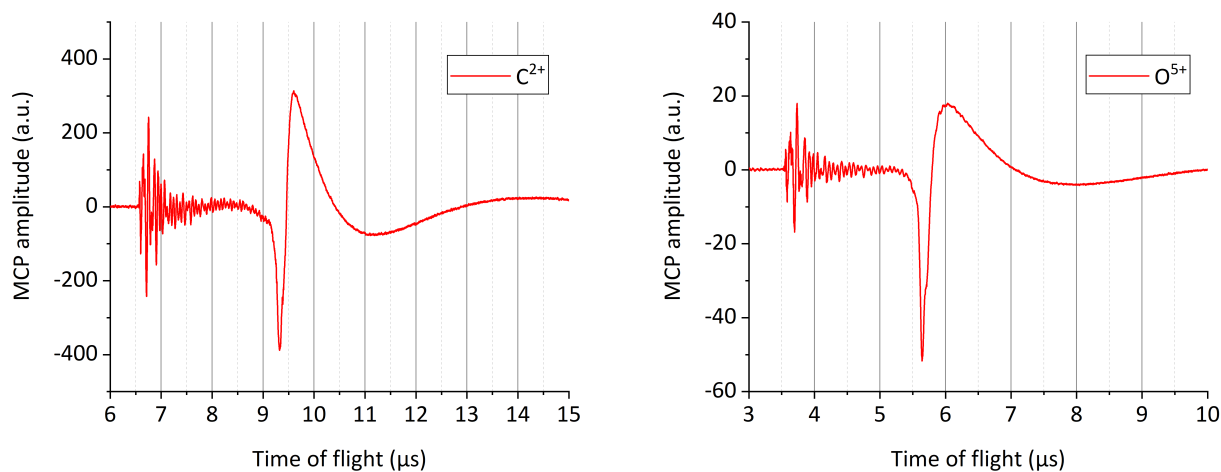
Figure 4.6.: First signals of extracted and previously stored (50 ms) ions for the relevant species at FLASH. C^{2+} on the left side and O^{5+} on the right side.

4.4. Beamtime operation @ FLASH

The beamtime was divided into two separated slots. The first one with three days and a second one with five days of operation. The idea was to tune the laser and the Penning trap in the first slot to get an appropriate overlap between the ion cloud and the laser beam (focal spot) and use the second slot for the ionisation measurements of O^{5+}.
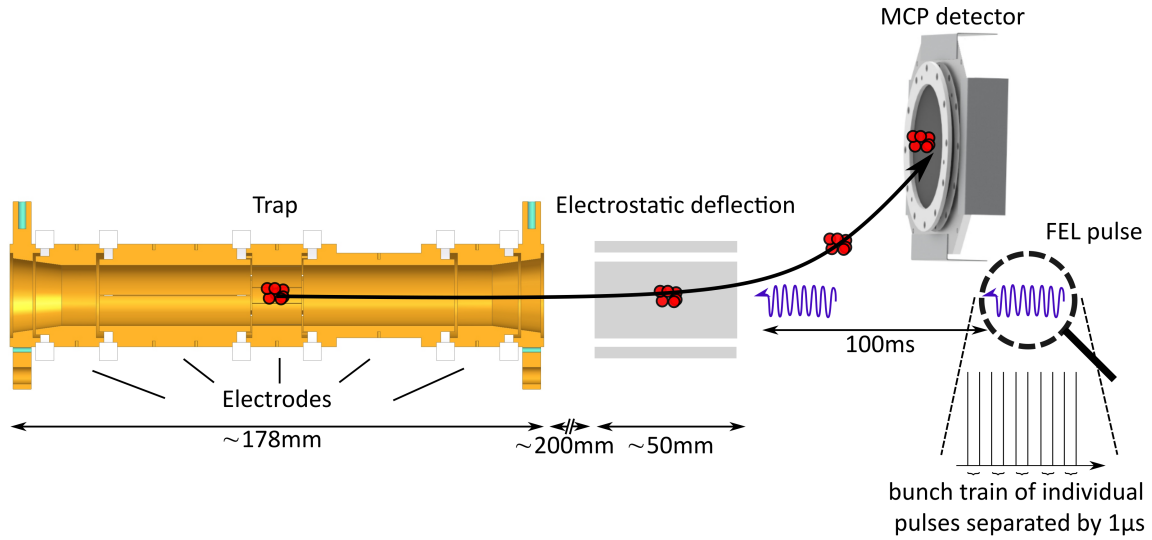
Figure 4.7.: Scheme of the experimental procedure. Ions are stored in the Penning trap and after the laser irradiation extracted onto an off-axis placed multichannel plate (MCP) detector. The time-of-flight is recorded and by that an identification of the ion species can be achieved. FEL pulses consist of a bunch train of individual pulses, separated by 1 μs.

Since FLASH operates at a repetition of 10 Hz, this 'base clock' was most often used as a trigger pulse for the operation cycle of HILITE. This means that the trigger signal of FLASH was slightly shifted to earlier times (-10 ms) and was used to trigger our EBIT ion source and the following deceleration and capture procedure. Therefore, the ion cloud was prepared once the FEL pulses arrived. Each FEL pulse consists of a bunch train of individual pulses (up to 400), separated in time by 1 μs, so that the laser irradiation only takes place at the beginning of this 100 ms cycle. Depending on the experimental conditions, one or more of those cycles have been used until the ions have been extracted by an electrostatic deflection onto an off-axis placed multi-channel plate (MCP) detector, as shown in figure (4.7). The flight time could therefore be evaluated to identify the ion species and charge state.

4.4.1. Residual gas ionisation

The first measurements performed have been the ionisation of residual gas inside the trap. The 'offline' (only Penning trap) measurements at GSI, as shown in section (3.4.5) had revealed an expected residual gas pressure in the trap of $p_{res} \approx 10^{-10}$ mbar and hence an ion lifetime of about 10 min for C^{2+}. The particle number density N_{res} is around $\approx 10^5$ mm^{-3}

and in the same order of magnitude as plasma densities of an ion cloud in a Penning trap. Hence, one can expect a background signal caused by those particles during the actual ionisation experiment which has to be known in order to extract and distinguish between interaction and background signal. Those measurements have been performed in the following way. First, the trap was closed, i.e. a potential on the endcap electrodes was applied. The ion source was not operated, so the trap was empty at the beginning besides the presence of residual gas. Then, the FEL pulse was switched on and the trap content was afterwards extracted onto the MCP detector as shown in figure (4.7). In order to reduce the amount of background, the last beam-defining FEL aperture was reduced from 10 mm diameter down to 3 mm in order to cut off the 'halo' of the FEL and by that decreased the volume exposed to the laser, see figure (4.8).
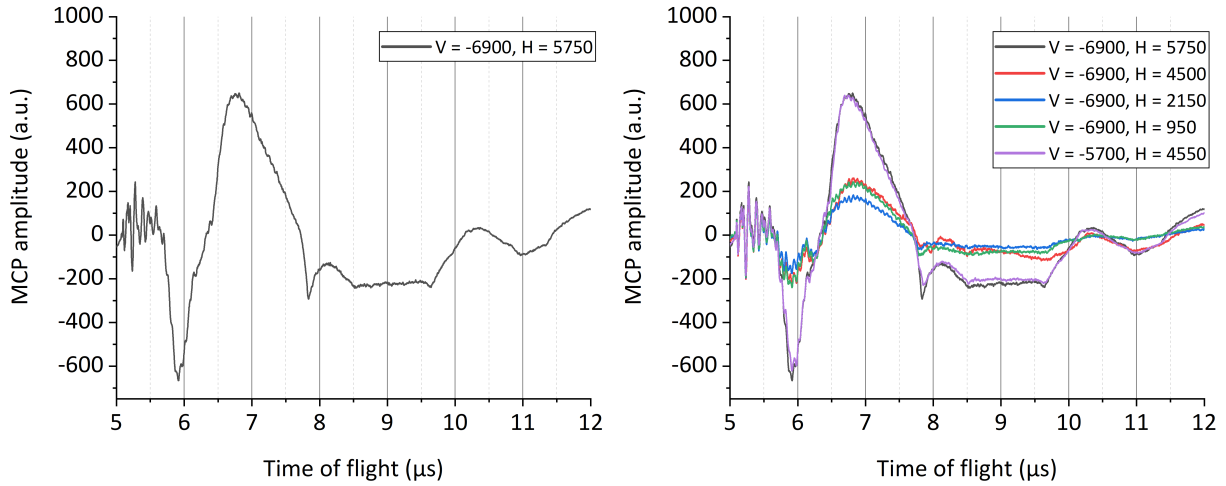
Figure 4.8.: (Left) MCP signal of residual gas inside the trap, ionised by the FEL and after a short storage time (50 ms) extracted onto the MCP. (Right) The focus position was shifted vertically (V) and horizontally (H). 1000 steps correspond to a shift of roughly 0.5 mm.

A scan of the focus position, both horizontally and vertically in 0.5 mm steps, was performed. It revealed that the transport efficiency of stored ions onto the off-axis MCP detector, as shown in the previous section (4.4), depends on the focus position of the FEL. Since remaining residual gas or photo-ionised particles outside of the confinement volume of the Penning trap leave the setup unaffected, the received signal can be related to the interaction of the FEL with the residual gas inside the trap. A relative focus position with KB actuator positions of (V = -6900, H = 2150 blue curve) revealed the lowest background.
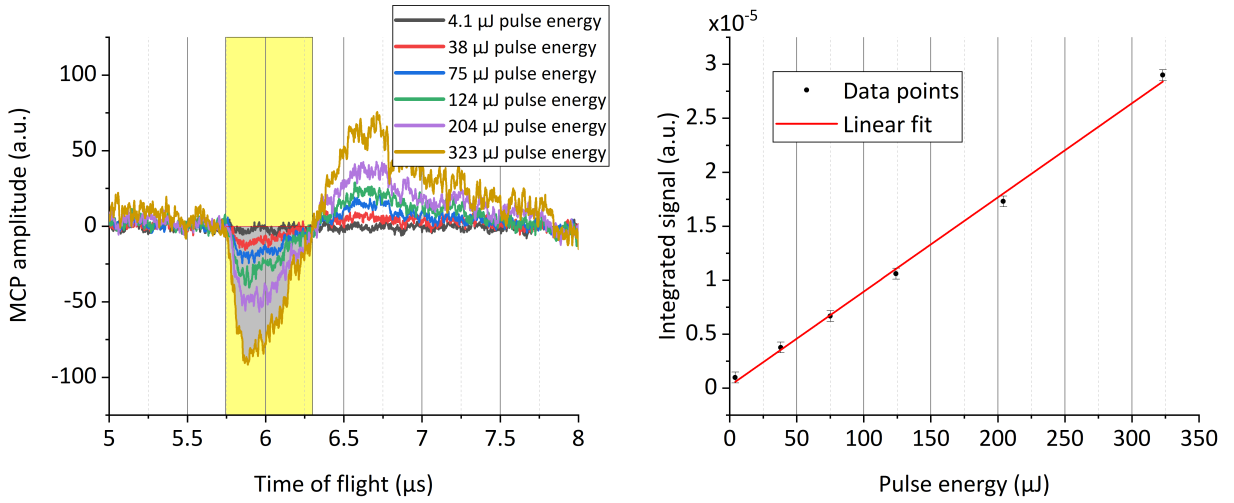
Figure 4.9.: (Left) MCP signal of residual gas inside the trap, ionised by the FEL and extracted onto the MCP. The pulse energy was changed and the effect onto the residual gas signal evaluated. (Right) Taking the integrated signal as a measure of the relative particle number reveals a linear dependency, which is expected for single-photon ionisation. Furthermore, a saturation of the detector could be excluded for those amplitudes as well.

Additionally, at this position a scan of the pulse energy was performed and is shown in figure (4.9). One would expect a linear behaviour dependent on the pulse energy and hence intensity for a single-photon ionisation. This was verified and is shown in figure (4.9) as well. Furthermore, this shows that a saturation of the detector, at least for this signal amplitude, is not observed.

4.4.2. Overlap between FEL and ion cloud - C^{2+}

As discussed in section (4.2.2), the overlap between the laser focus and the ion cloud is of great importance in order to increase on the one hand the amount of ionisation products, i.e. signal strength and on the other hand to enable the extraction of photo-ionisation cross-sections. The focus geometry and intensity distribution within the ion cloud need therefore to be known. The procedure for the measurements with C^{2+} was the same as the previous one for the residual gas. A radial scan of the focus position by adjusting the horizontal and vertical KB actuator settings was performed. By that, a total shift of the focus position by $2.5\,\mathrm{mm}$ was achieved. In comparison to the results of the residual gas, no dependency for C^{2+} was seen, so the position of lowest background for the residual gas (V = -6900, H = 2150) from the previous section was therefore used for this measurement as well.

Since the background signal cannot be neglected, a procedure to distinguish between the background and the interaction signal of C^{2+} with the FEL has to be developed. Assuming that the interaction between C^{2+} and the FEL is independent of the interaction between the residual gas and FEL and the residual gas is equally distributed, a consecutive approach is used to disentangle the two effects. One has to emphasize that performing a measurement, if not otherwise mentioned, always implies the execution of several hundreds of individual measurements in order to cancel out fluctuation effects, such as deviations of the average stored ion number or laser intensity.

The first step was a measurement of the residual gas ionisation as described in the previous section (4.4.1). The second step was then a corresponding measurement of a stored ion cloud in the trap without interaction with the FEL. The third and last step was then the merging of C^{2+} and the FEL. By the combination of the obtained signals one was able to extract the so-called 'interaction' signal S_{int} given by

$$S_{int} = S_{comb} - S_{stored} - S_{residual}, \tag{4.1}$$

which represents the interaction of the stored ions by the superimposed FEL without the residual gas interference. The results obtained for each measurement step are depicted in figure (4.10) from top left to bottom right. The interaction signal, shown in green in the bottom right plot represents the reduction of stored C^{2+} due to the interaction of the ion cloud with the FEL pulse. The higher, the more of the previously stored ions have been affected by the laser.
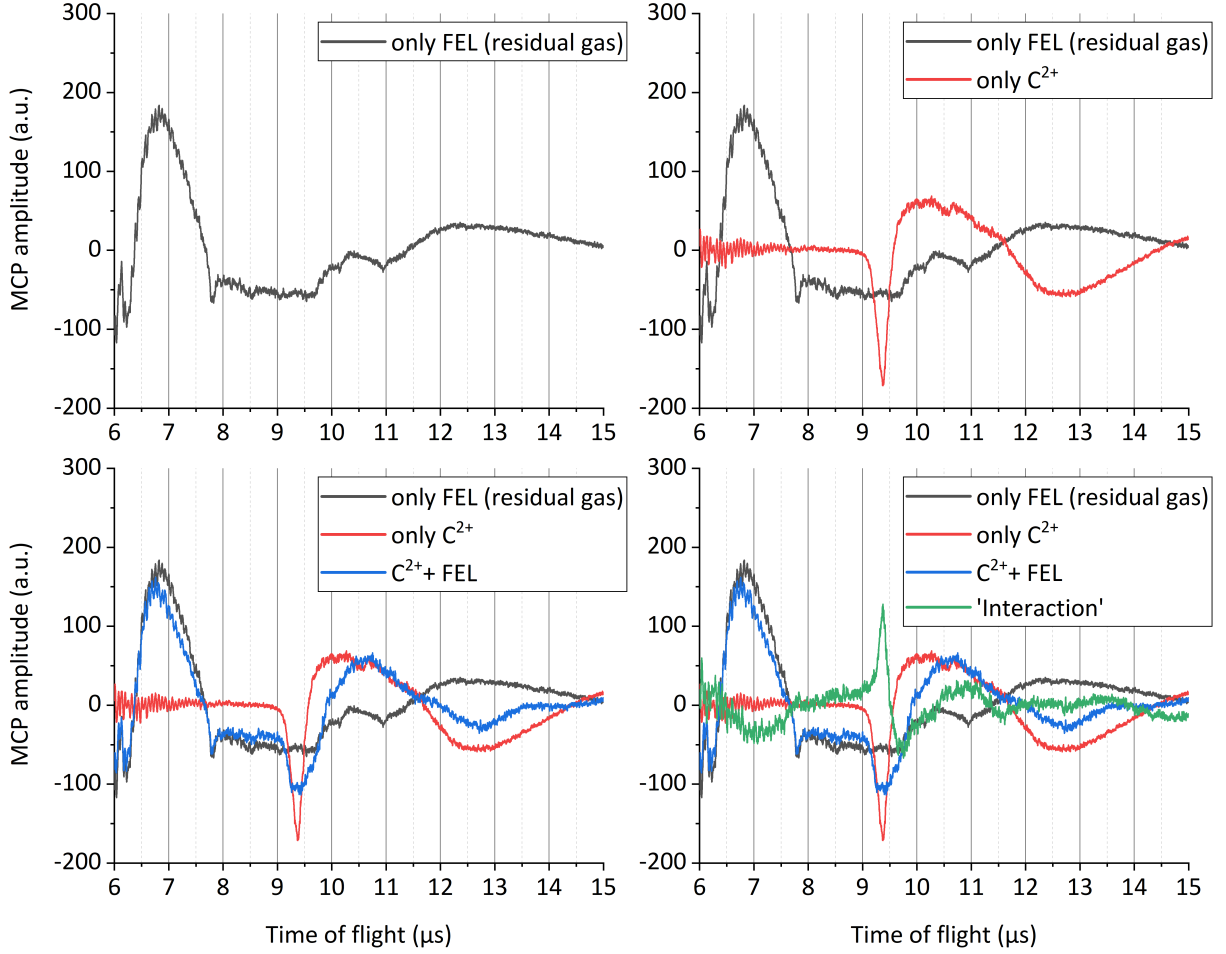
Figure 4.10.: Measurement sequence for the ionisation of C^{2+} to find the overlap between FEL and ion cloud. Trap content is extracted after laser irradiation onto an external MCP detector. Ionisation signal of residual gas by the FEL (top left). Stored ion signal of C^{2+} without the FEL (top right). Combined signal of stored ions and the FEL (bottom left). Interaction signal extracted from the previously shown individual measurements as explained by (4.1) (bottom right). A positive signal corresponds to a reduction of previously stored C^{2+} ions that have interacted with the laser.

In order to identify the ion species and charge states, the same time-of-flight (ToF) technique as presented in section (3.1.2) is used. The trap content, no matter whether residual gas or ions of interest, are extracted onto the external MCP detector and further analysed. Since the time of flight is proportional to the mass-over-charge ratio of the ion species

$$t_{ToF} \propto \sqrt{\frac{m}{q}}, \tag{4.2}$$

an assignment can be carried out and is supposed to follow a linear behaviour. A deviation from that would mean that the assumption was wrong. Figure (4.11) shows such an assignment (species, charge state and time of flight) for the performed measurements on the left plot, while the corresponding linear fit is shown on the right hand side. Since a deviation cannot be seen, the assumption can be considered correct.
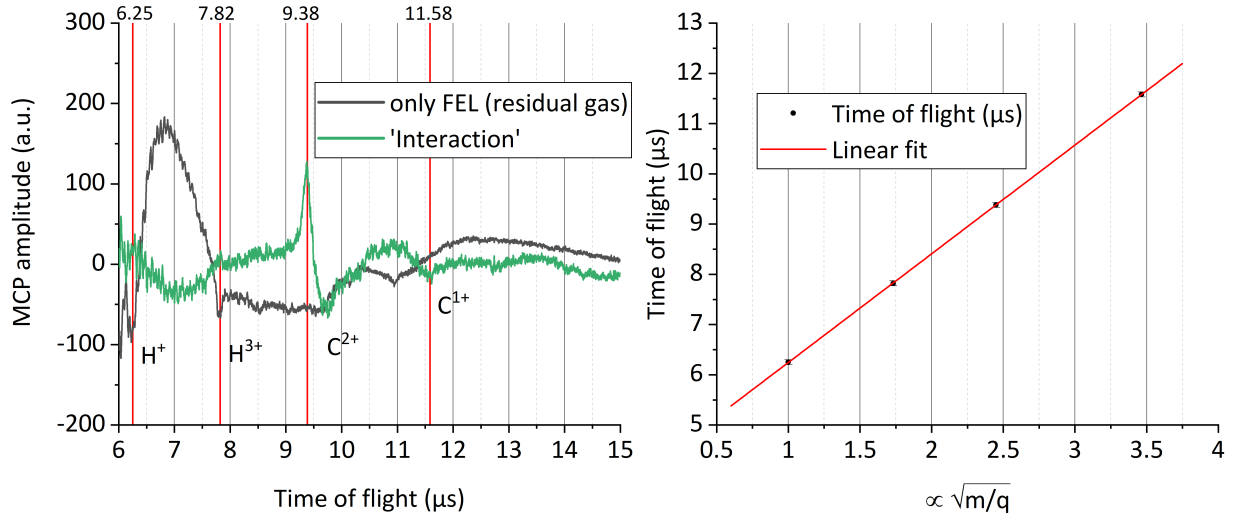
Figure 4.11.: (Left) Trap content is extracted onto the MCP detector and the identification of ion species and charge state is done by a time-of-flight measurement. (Right) Linear behaviour verifies the correct assignment. Error bars are barley visible.

From the intersection and slope of the linear fit, the expected position of C^{3+} can be calculated by

$$t_{ToF}(C^{3+}) = \sqrt{\frac{12}{3}} \cdot 2.16\,\mu s + 4.08\,\mu s = (8.4 \pm 0.05)\,\mu s. \tag{4.3}$$

Although an interaction between the FEL and the stored ion cloud of C^{2+} could be verified, at the expected position for C^{3+} a signal could not be found.

4.4.3. Ionisation of O^{5+}

The next ion target of interest was O^{5+}. Therefore, the trapping parameters have been adjusted accordingly as shown in table (A.2). The FEL was set to 400 bunches with an energy of 70 eV and 330 µJ pulse energy. This photon energy corresponds to transition between the two-photon and three-photon ionisation of O^{5+} as predicted by the calculations and shown in figure (4.3). First, the same measurement as in the previous C^{2+}-case was performed. So a residual gas background signal created by the FEL and stored in the trap,

a stored ion signal, and the combination of both have been performed as shown in figure (4.12). According to equation (4.1), the 'interaction' signal was extracted and can be seen in (4.12) in the bottom right plot in green.
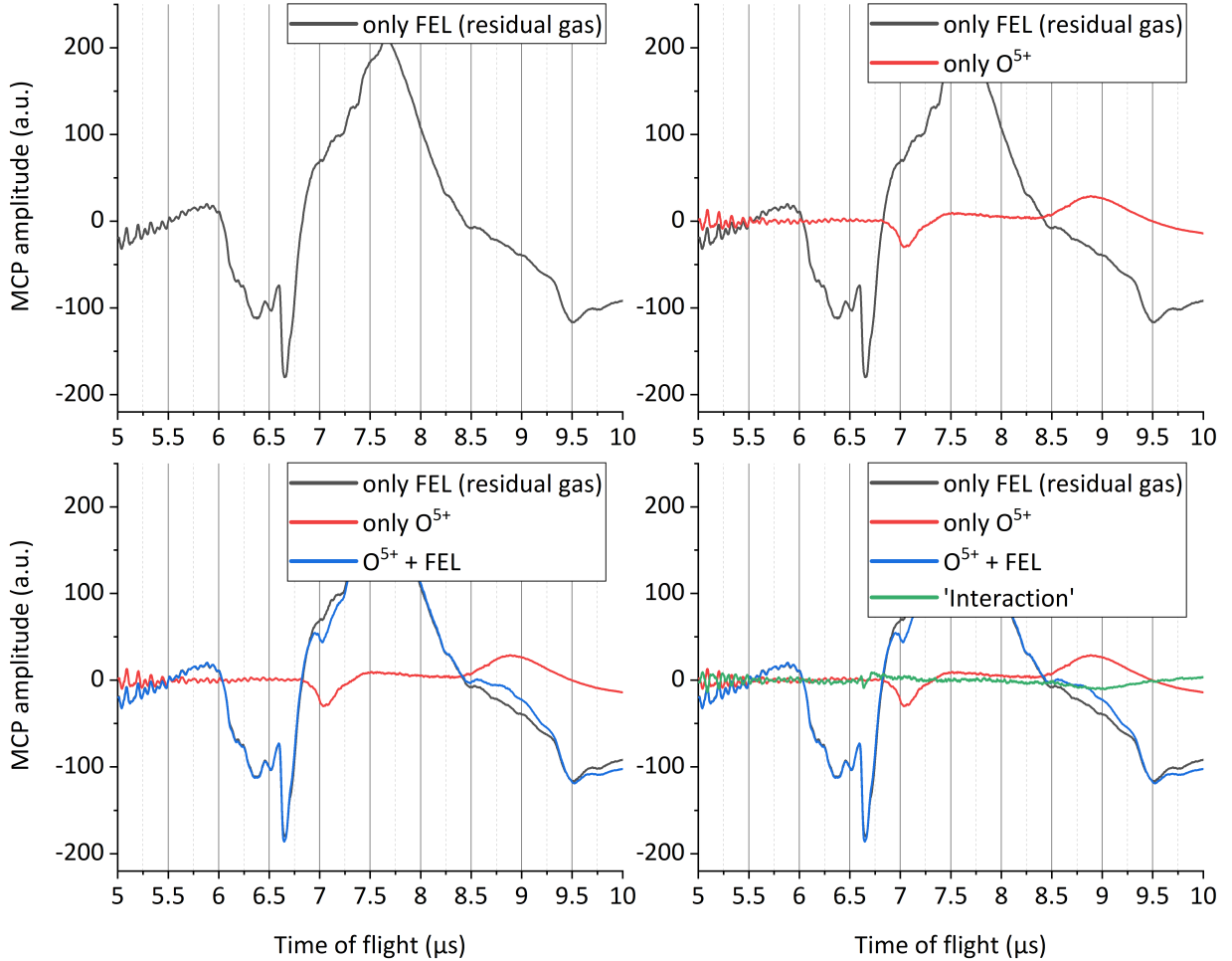
Figure 4.12.: Measurement sequence for the ionisation of O^{5+}. The procedure is the same as for C^{2+}. Trap content is extracted after laser irradiation onto an external MCP detector. Ionisation signal of residual gas by the FEL (top left). Stored ion signal of O^{5+} without the FEL (top right). Combined signal of stored ions and the FEL (bottom left). Interaction signal extracted from the previously shown individual measurements as explained by (4.1) (bottom right). Unlike in the C^{2+} case, no evidence for interaction between the ion cloud and the FEL could be found.

In comparison to the C^{2+} case, an interaction could not be seen. The lack of 'interaction' signal is unexpected, since one would expect at least a reduction of O^{5+} due to the FEL; an absence of O^{6+} could in the first place be explained by a small cross section in this energy

region. The transition from two-photon to a three-photon absorption results in a decrease of expected interactions by four orders of magnitude, as depicted in figure (4.3).

The next measurement step was therefore a photon energy scan of the FEL from $70\,\text{eV}$ - $90\,\text{eV}$ with a step size of $2\,\text{eV}$. The results are presented in figure (4.13).
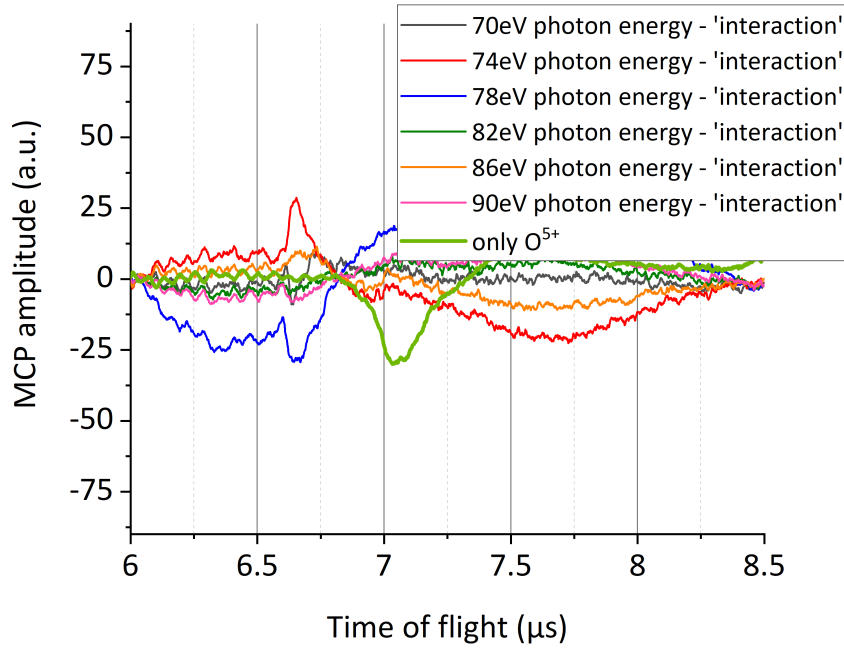
Figure 4.13.: Photon energy scan of O^{5+} from $70\,\text{eV}$ up to $90\,\text{eV}$. As a reference, the signal of stored O^{5+} without interaction with the FEL is additionally shown in green.

Again, neither an interaction of O^{5+} nor a signal of O^{6+} could be detected, although the expected number of interactions should have been sufficient.

4.4.4. Background pressure estimation by life-time measurements

Due to the strong background signal caused by residual gas and the absence of the expected C^{3+} and O^{6+} signals, an estimation regarding the vacuum conditions was performed. As described in section (3.4.5), the residual gas pressure can be estimated by a determination of the stored ions' lifetime. Therefore, several storage time measurements ($1\,\text{s}$ up to $300\,\text{s}$) for C^{2+} have been performed and the time evolution of the signal was detected. Since no signal for storage times above $30\,\text{s}$ have been observed, only five data points could be used. The result is depicted in figure (4.14).
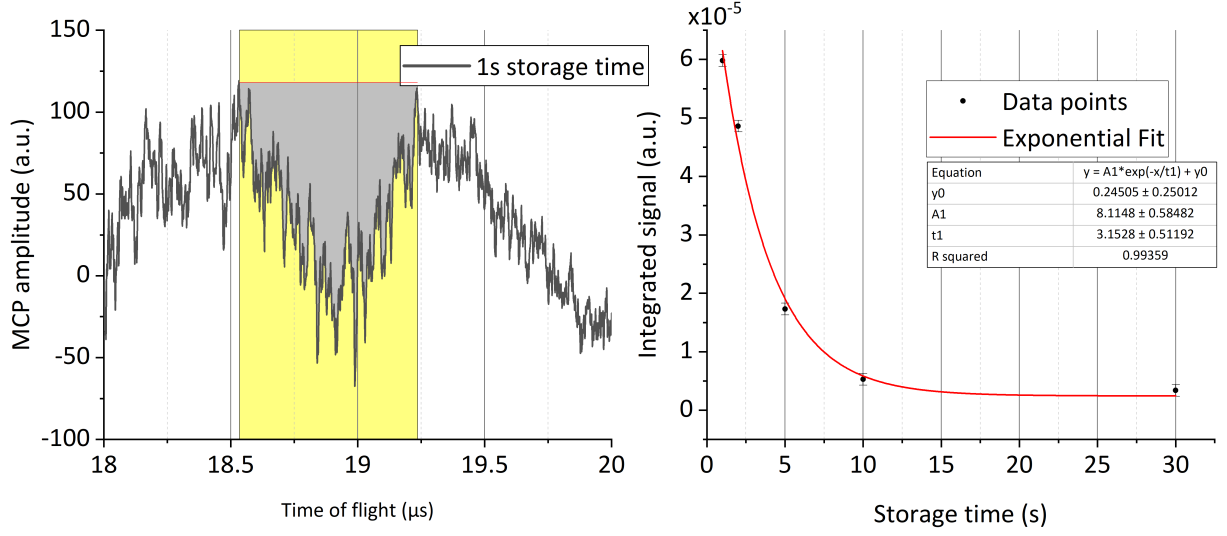
Figure 4.14.: (Left) Exemplary signal of C^{2+} for a storage time of 1s including the extracted integrated signal used for the lifetime measurement. (Right) Exponential fit for five different storage times results in an ion lifetime of $t_{ion} = (3,15 \pm 0,51)\,\text{s}$. Error bars are barley visible.

One obtains an ion lifetime constant based on those measurements of $t_{ion} = (3,15 \pm 0,51)\,\text{s}$, and hence by rearranging equation (3.3) a residual gas pressure of

$$p_{res} \approx 2 \cdot 10^{-8}\,\text{mbar}, \tag{4.4}$$

assuming hydrogen being the most prominent constituent in the cryogenic Penning trap environment. This is at least two orders of magnitude higher than during the 'offline' commissioning at GSI, where lifetimes of several hundred of seconds and correspondingly a pressure of 10^{-10} mbar have been achieved and can explain why the residual gas background dominates and higher charge states are not visible in the spectra. The explanation for this difference could not conclusively be found since neither did the vacuum gauges showed relevant discrepancy from the values back at GSI, nor did the performed leak tests showed a suspicious spot at the setup. The most probable reason from our perspective is a constant 'gas flow' from the beamline on the Penning trap axis which increases the local pressure without being seen by the gauges.

4.4.5. Lessons learned

The beamtime at the FLASH facility was the first 'online' commissioning (with laser) of the HILITE experiment. Although the interaction between the FEL and the ion cloud for the applied C^{2+} ion target could be shown, the physics case for O^{5+} remained unfortunately unsuccessful. Two major points have to be addressed for future beamtimes.

Vacuum conditions

> The most important quantity which made work challenging has been the residual gas pressure in the setup during the experiments. Back at GSI it was in the range of $p_{res} \approx 10^{-10}$ mbar, while during the beamtime only $p_{res} \approx 10^{-8}$ mbar was achieved. Hence, a lot of effort is put into improving the vacua conditions in general. The goal is to achieve a trap pressure of around $p_{res} \approx 10^{-12}$ mbar which would result in storage times in the order of minutes to hours depending on the ion species and charge state.

Ion cloud - laser overlap

> The second topic that needs to be taken care of is the proper overlap between the laser pulse and the ion cloud. Depending on the laser system (focal spot size and Rayleigh length) this can be critical or less critical. The first step in this regard is the mechanical alignment between the focus and the trap centre, both axially and radially. In case of this beamtime, the FLASH alignment laser (optical laser, which imitates the FEL beam) was used to align the setup. Even if the focus spot matches the trap centre, an inefficient deceleration and capture process due to small offsets of the ion beam trajectory from the central beam axis, for instance caused by field imperfections, general emittance of charged ion beams, or imperfections of ion optical elements can lead to stored ion clouds on large radii which are therefore outside of the laser focus.

A last and not less important point, which belongs to both of the previous points is the improvement of the ion cooling technique, mainly resistive cooling, see section (2.3.5), since it allows to increase the target density by reducing the motional amplitude and hence helps in terms of the laser overlap with the ion cloud, but needs longer storage times in order to be efficient and therefore better vacuum conditions. The planned and partially implemented changes will be addressed in the following chapter.

5. Improvements of the setup for further laser-ion experiments

The biggest challenges we faced during the beamtime at FLASH have been the poor vacuum conditions. A background pressure of around $\approx 10^{-8}\,\text{mbar}$ is disadvantageous in several ways. First and most obvious is the storage time of trapped ions, even for lower charge states. Due to recombination processes it is too short for a proper target preparation in terms of purity and density. Since the ions are lost quickly, a cooling process and hence an increase of the target density cannot be efficiently applied. In addition, the non-destructive detection, which is based on the same image charge effect as the cooling process is therefore not applicable. The second consequence of having a high pressure is the residual gas itself, since it can interact (and be ionised) with the FEL and cause a significant/predominant background signal due to its high abundance.

A second part which we want to address in the future is the increase of transport, deceleration and capture efficiency of the externally produced ions. An ion beam has a finite emittance, hence it diverges the longer the trajectory is. Additionally, the Coulomb interaction further increases the divergence, like space-charge effect or intra-beam scattering. Therefore, proper ion optical elements have to be used in order to compensate for that.

Additionally, some further changes on the detector side will be presented in order to increase the sensitivity and efficiency of the detection system.

5.1. Changes to the Penning trap

As mentioned several times throughout this thesis, for instance in figure (2.7) and (3.20), or table (2.1) the HILITE Penning trap is an open-endcap design with $20\,\text{mm}$ openings on both sides for particle loading and laser access. In comparison to most other Penning trap experiments, this is quite unusual. It opens the possibility for an easy laser access, but at the same time for a high gas flow into the trap volume. The experiences gained during the

beamtime at FLASH show that we have to limit the open access to a minimum. We address this by the implementation of dedicated entrance and exit apertures on both trap sides equipped with central holes with a diameter suited for the laser in operation. That means that for instance in terms of an FEL with a long Rayleigh length a smaller diameter can be used than for an Ti:Sa laser system in the optical regime. The experimental realization can be seen in picture (5.1), as an example with a 4 mm aperture.
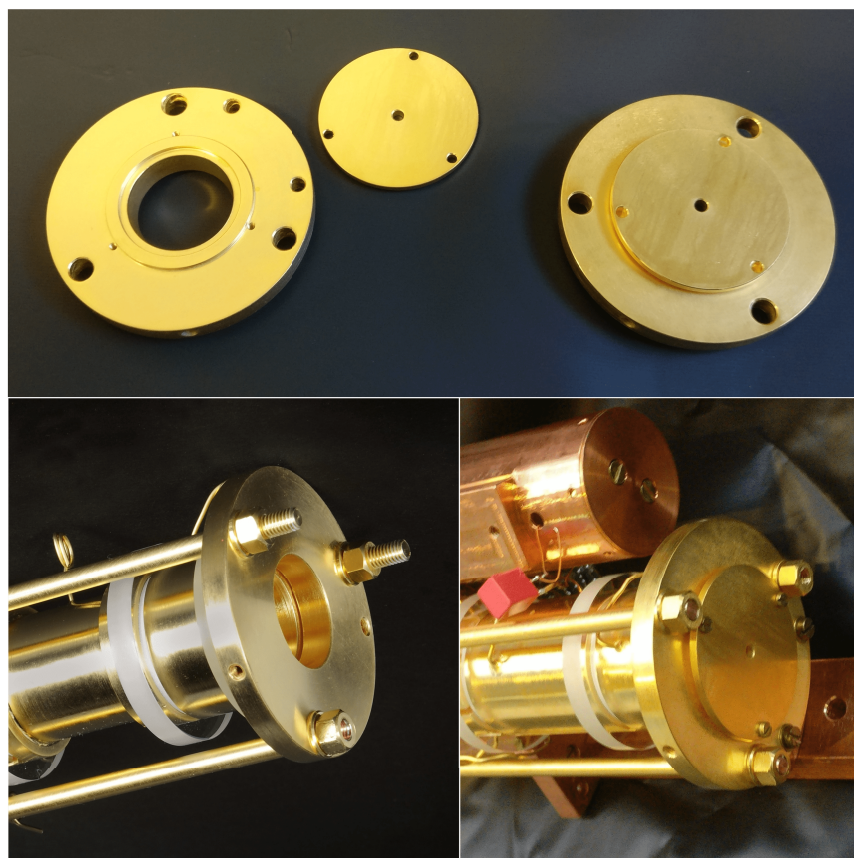
Figure 5.1.: (Top) Dedicated gold-plated copper apertures with a central hole adapted to the corresponding laser to reduce the open access to the bare minimum. (Bottom left) Trap opening without aperture and an opening of 20 mm. (Bottom right) Trap with an implemented aperture with a diameter of 4 mm.

Those apertures work like a diaphragm in the sense that they act as a barrier for the gas molecules and thus separate the trap volume from the magnet-bore volume. So the pressure gradient is much larger and hence the pressure inside much lower compared to the outside. Vacuum simulations have been performed in order to verify the benefit of the implementation. The program used was *MolFlow+*, a test-particle Monte-Carlo simulator

developed at CERN [81]. It allows to compute the vacuum conditions of a given setup by creation of the geometry and definition of parameters like outgassing, desorption rates, temperature distributions and pumping capabilities. Two different simulations have been performed. First, a simulation of the current trap design with the full 20 mm opening, and a second one including 2 mm apertures, which would be the smallest ones, that could be used for the FEL. The central trap part was set to a temperature of 5 K and a sticking coefficient $\alpha = 0.9$ for hydrogen according to [82, 83] was used. The remaining parts were set to 80 K and α was now assumed to be $\alpha \approx 0.5$, since the main constituent for a non-baked vacuum system is water, which will be frozen out at this temperature. Furthermore, all parts beside the trap have been configured in order to have an outgassing rate of 10^{-10} mbar $\cdot$ l/s/cm², which is according to [84] a typical value for non-baked metal surfaces. The two openings on the left and right hand side have been set to 10^{-8} mbar $\cdot$ l/s/cm² to simulate a large residual gas flow from the outside of the magnet bore. The simulation results can be seen in figure (5.2).
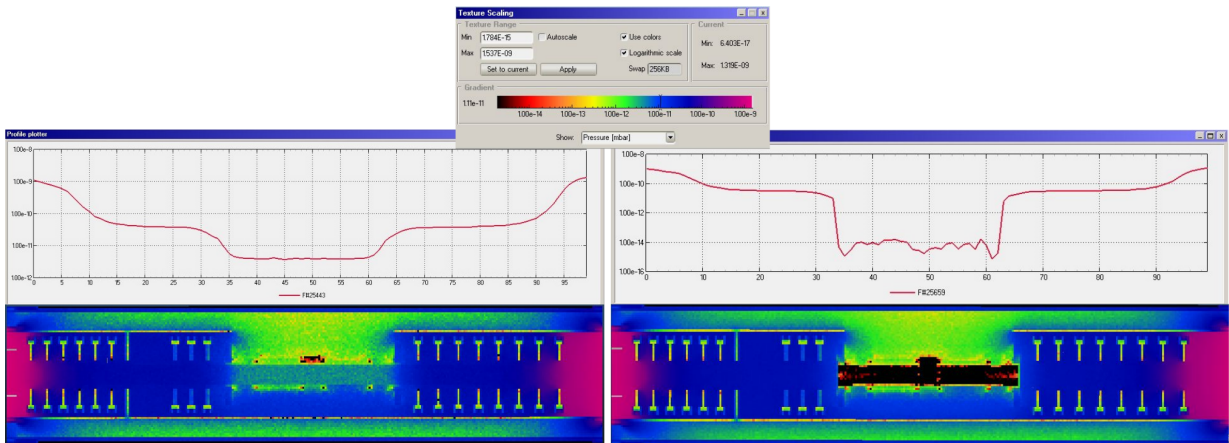
Figure 5.2.: *MolFlow+* vacuum simulation of HILITE. The setup which is placed inside the bore of the superconducting magnet is shown. The left side shows the case without apertures, while the right hand side shows the effect of 2 mm entrance and exit apertures. The central plots show the pressure distribution on axis, while the coloured plot at the bottom depicts the overall distribution. The colour scale used in shown in the top figure. Outgassing and desorption rates have been the same for both simulations.

The differences in the outcome can be seen directly with the bare eye. While without apertures the pressure in the trap decreases roughly by an order of magnitude in comparison to the outside of the trap, in case of 2 mm apertures the decrease is about 3.5 orders of magnitude, hence 2.5 orders of magnitude better than without the apertures. This can be

explained by the smaller diameter of the opening and hence smaller gas flow. Additionally, the stainless steel vacuum chambers attached to the left and right of the magnet will be replaced by appropriate chambers out of a specific aluminium alloy (6000 series). The achievable outgassing rates for this alloy is about one order of magnitude smaller than the one of stainless steel [85].

Both changes in combination will allow us to improve the the vacuum conditions inside the trap by around three orders of magnitude and therefore enable us to store low charge states up to several hours, and highly charged ions for at least several minutes, both of which sufficient for laser-ion interaction experiments.

5.2. Changes to the ion optics

The second part which has to be addressed as a consequence of the FLASH beamtime is the increase of the transport, deceleration and storage efficiency. Effects like space charge, ion beam emittance and stray fields (electric and magnetic) can lead to deviations of the ion trajectory and hence an off-axis capture process. Therefore, a large effort is necessary in order to provide an ion cloud of sufficient density for the laser interaction. This increase in efficiency can be achieved in the first place by additional and specifically designed ion optical elements which compensate for those effects. One of those elements is the newly designed 90°-electrostatic deflector as depicted in figure (5.3). The overall working principle is the same as for the old deflector, presented in section (3.3.1), i.e. double-focussing and equipped with a hole in the outer electrode for the laser exit. Changes have been made in mechanical stiffness and adjustability, since the electrodes of the old deflector were made of thin plates, which could be bent easily while being assembled. Therefore, field imperfections could occur and lead to distortions of the ion beam trajectory. Now, the electrodes are manufactured from massive aluminium blocks and polished on the inner surface. Additionally, two Sikler lenses have been attached on the entrance and the exit ports. The advantage of a Sikler lens in comparison to a typical Einzel lens is the possibility to focus and steer the passing ion beam at the same time [86]. Thereby, it is possible to compensate for small misalignments of the ion beam which can occur on the way from the EBIT due to space charge and stray field effect. Furthermore, the transmitted beam after the deflector can be focused towards the next ion optical element, like the pulsed drift tube (PDT), where a centrally aligned and focused ion beam increases the efficiency of the deceleration process. The deceleration stage will also be updated in this context. In section
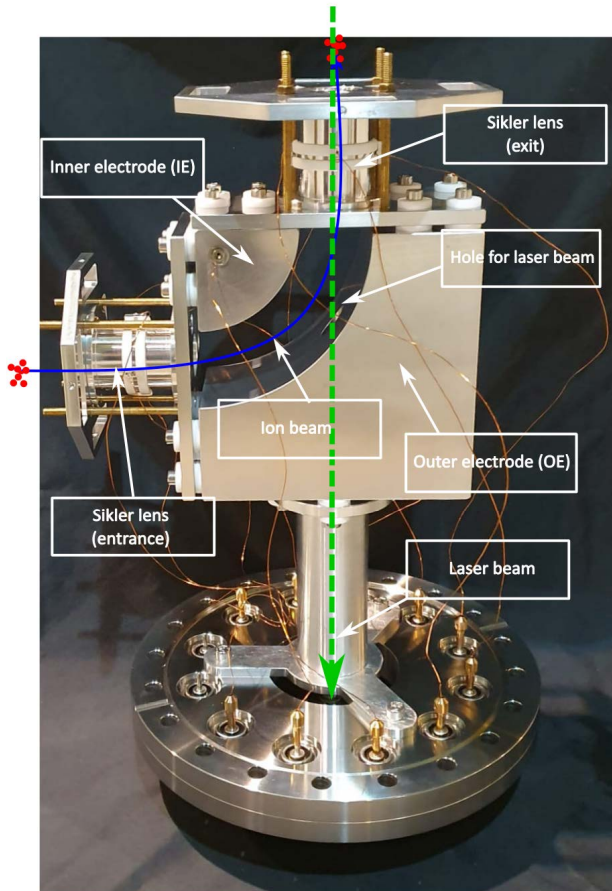
Figure 5.3: New electrostatic 90°-deflector, with an improved design in terms of stiffness and adjustability compared to the previously used one. Furthermore, two Sikler lenses at the entrance and the exit of the deflector are used to address beam misalignment and focus the ion beam.

(3.4.2) the pulsed drift tube (PDT) was separated from the trap by a grounded electrode and a charge counter (3.4.1) was placed several centimetres away from the entrance of the trap. Additionally, it was electrically a single-electrode design which was switched from a positive to a negative potential while the ion bunch was inside of the tube. In the new design, it is located closer to the trap and is made of two serrated, interlaced electrodes which in addition allows an axial bunch-compression due to a voltage gradient which can be applied on top of the deceleration voltage [87]. A CAD section view of the design and the real component can be seen in figure (5.4). Beside the PDT, the electrode stack consists of another Sikler lens, placed right in front of the drift tube and an upstream charge counter electrode to detect the incoming ion beam.
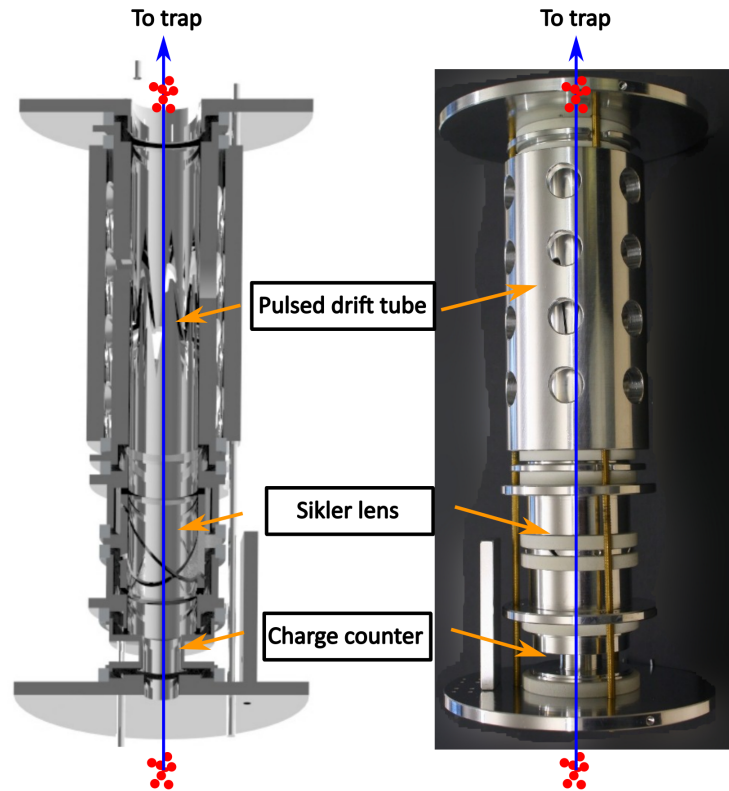
Figure 5.4.: New pulsed drift tube with two serrated, interlaced electrodes which enables beside a deceleration an axial bunch-compression. Upstream a charge counter and a Sikler lens is placed in order to detect and adjust the ion beam if needed.

5.3. Additional changes - Detector changes

The last part which has to be addressed is the detection of the extracted particles. In figure (4.7) of the previous chapter, the experimental scheme was depicted with an off-axis MCP detector. From residual gas ionisation measurements, see figure (4.8), a position-dependent extraction efficiency can be extracted. Therefore the approach is to use a MCP detector with a central hole for future experiments, so that the deflection onto the MCP becomes unnecessary. In addition, large signals, from a large number of particles hitting the detector in a short time period, are an issue regarding saturation effects and associated overshoot signals, as can be seen in figure (4.8). This will be addressed by a new, two-stage amplification system provided by *Roentdek*, in which one of the stages is optimized for large signals (small amplification) and the second one for small signals (high amplification). Thereby, the signal-to-noise ratio can be improved once one has to distinguish between small signals of interest, and large signals of background.

6. Summary and outlook

Since the description of the photoelectric effect by Einstein in the early 20th century, the study of interactions between light and matter has been advanced to a much wider range of light intensities and energies, thus forming a much broader field of research. First, limited by intensity, frequency and coherence, the study of experimental cases and the applicability was restricted. With the introduction of lasers, the circumstances changed severely and effects like laser-ionisation, -excitation, spectroscopy in terms of atomic physics, or industrial applications became accessible. While intensity steadily increased, non-linear effects like multi-photon ionisation or tunnel ionisation became experimentally accessible and have been described by theory. Since the development of the free-electron laser (FEL), the XUV and X-ray regime became available as well. Nowadays, intensities of the order of $10^{20}\,\mathrm{W/cm^2}$ allow access to inner atomic shells (down to the last k-shell electron) of highly charged ions to investigate single active electrons.

The HILITE experiment presented within this thesis aims for the investigation of such ions under the influence of highly intense laser light. Due to its specific design in terms of 'built-in' ion production (EBIT), transportability and laser accessibility, it is not limited to a certain type of laser system and can be attached to basically any of the large user facilities, depending on the experimental case. HILITE is based on a Penning trap to capture, store and detect ions and facilitates the possibility to control the target properties before the laser irradiation takes places. By keeping the target properties known, the interaction between the laser and the ions can be studied in more detail than previously with other target techniques.

During the thesis, the complete experiment comprised Penning trap, ion production, ion transport, deceleration, capture, storage, detection and extraction has been designed, built and commissioned. The operation of our dedicated ion source (EBIT) to provide several different ion species and charge states was performed and could be verified. The selection of those ion species and charges states after extraction of the source as well as the consecutive redirection of the ion bunch onto the beam axis by an electrostatic deflector

could be achieved and verified. To this end, several ion optical elements, like Einzel lens and deflection electrodes have been implemented and diagnostic systems like multi-channel plate, fluorescence screen, Faraday cup have been installed to verify the intended operation of the devices. Additionally, a single-pass non-destructive detection system called 'charge counter', based on the principle of induced image charges [13], was developed by us [56] and implemented and tested in the setup. Storage times of the order of several minutes for lower charged ions have been achieved and could be detected with the non-destructive tuned RLC-circuits. A first 'laser-ion' beamtime application was submitted and granted to study the ionisation cross section of hydrogen-like carbon C^{5+} and lithium-like oxygen O^{5+} at the free-electron laser system FLASH @ DESY in Hamburg. An interaction between the stored ions C^{2+} and the focused laser beam could be verified, although unfortunately an unexpected high background pressure prevented the ionisation study of the proposed target species.

To address this issue, several improvements of the setup, for instance apertures at the entrance and exit of the trap specifically designed for the laser system supported by vacuum-simulations have been installed to improve the inner-trap vacuum. Additionally, a newly designed electrostatic beam deflector together with enhanced ion optical elements (Sikler lens) will improve the possibility to guide the ions on axis and hence lead to better deceleration and capture efficiency. After implementation and commissioning of the new parts a second beamtime at the JETI laser in Jena is planned with a possible target of hydrogen-like neon Ne^{9+}.

A. Appendix

A.1. Inductance and capacitance of resonance circuits

The most important electrical properties defining a resonator circuit are the inductance and capacitance of the coil and the housing. The calculation of those for ideal parts is rather easy, but one struggles transferring them to real parts. Therefore, semi-empirical formulas given in the following are used to design the circuits and to estimates their properties. The inductance in units of μH for a helical single-layer air coil reads as [51]

$$L \approx \frac{D_1^2 N^2}{18 D_1 + 40 l_1} \tag{A.1}$$

with D_1 and l_1 being the diameter and length of the coil given in inches and N the number of winding around the core as depicted in figure (2.14). Inside a housing as described above and shown as well in figure (2.14), the inductance decreases and can be estimated by [32, 50]

$$L_H \approx L \left[1 - \left(\frac{D_1}{D_2} \right)^3 \right] \left[1 - \left(\frac{l_1}{2 l_2} \right)^2 \right] \tag{A.2}$$

with l_2 and D_2 being the inner dimensions of the housing. Two empirical ratios, $l_1 = 0.55 D_2$ and $l_1 / 2 l_2 = 0.377$ ensure a minimal decrease of the coils inductance. As mentioned briefly, most often space limitations require the use of a multilayer winding technique for the coil. For those cases, the inductance can be estimated by [32, 50]

$$L \approx \frac{0.2 (D_1^2 N^2)}{3 D_1 + 9 l_1 + 10 D_w} \tag{A.3}$$

with D_w being the thickness of the layers (wire thickness times number of layers). The quality factor for such a coil can be estimated by $Q \approx 20 D_2 \sqrt{\omega_0}$.

Likewise, the capacitance of a single-layer air coil can be estimated and described [32, 50] by the 'turn-to-turn' capacitance C_{TT} and the 'coil-housing' capacitance C_{TH}, which account

for the capacitance introduced by neighbouring wires and the housing of the coil. They are given by

$$C_{TT} \approx \frac{\pi^2 D_1 \epsilon_0}{ln(p/2r + \sqrt{(p/2r)^2 - 1})}, \;\; C_{TH} \approx \frac{2\pi^2 D_1 \epsilon_0}{ln(h/r + \sqrt{(h/r)^2 - 1})}, \qquad \text{(A.4)}$$

with the vacuum permittivity ϵ_0, the wire thickness r, the distance between neighbouring wires p and the distance of the wire from the housing h. Typical values obtained for the inductance and capacity are several mH and pF. Based on those estimations the design of such resonators is performed. Since small variations in the geometric design, for instance the distance between adjacent wires may change, which can easily happen due to thermal contraction while cooling the system to liquid helium temperature $(4\,\text{K})$, could result in values for the inductance and capacity which differs by a factor of two or three from the estimated ones. Therefore the proper design is challenging and becomes basically a trial and error process up to a certain degree.

Based on those guidelines, the axial and cyclotron resonators for HILITE have been designed. Both circuits consists of a helical coil wound around a PTFE (Teflon) core placed inside an OFHC copper housing. Impressions have ben shown in (3.22) and (3.24). In the following table, the most important electrical and physical properties are given. Furthermore picture (A.1) shows the implemented varactor circuit board, which was developed in close collaboration with *Stahl electronics* to tune both resonance circuits. Three independent diodes conneced in parallel increases the capacitance between $8 - 24\,\text{pF}$ and allows therefore a shift of the resonance frequency of the attached circuit.

Table A.1.: ARES and CRES electrical and mechanical properties.

Property	Axial resonator	Cyclotron resonator
Material (housing and wire)	Copper	Copper
Material (core)	PTFE	PTFE
Design frequency (MHz)	0.457	38.4
Inductance (µH)	≈ 4500	≈ 1
Capacitance (pF)	27	17
Number of turns N	1200	10
Number of layers	4	1
Wire diameter (mm)	0.282 (incl.PTFE isolation)	1 (bare)
DC ohmic resistance (Ω)	120	0.1
Inner length of the housing l_2 (mm)	130	40
Inner diameter of the housing D_2 (mm)	33	30
Length of the coil l_1 (mm)	86	22
Diameter of the coil D_1 (mm)	24	20
Varactor diode capacitance (3x) (pF)	2 (10 V) - 8 (0 V)	2 (10 V) - 8 (0 V)
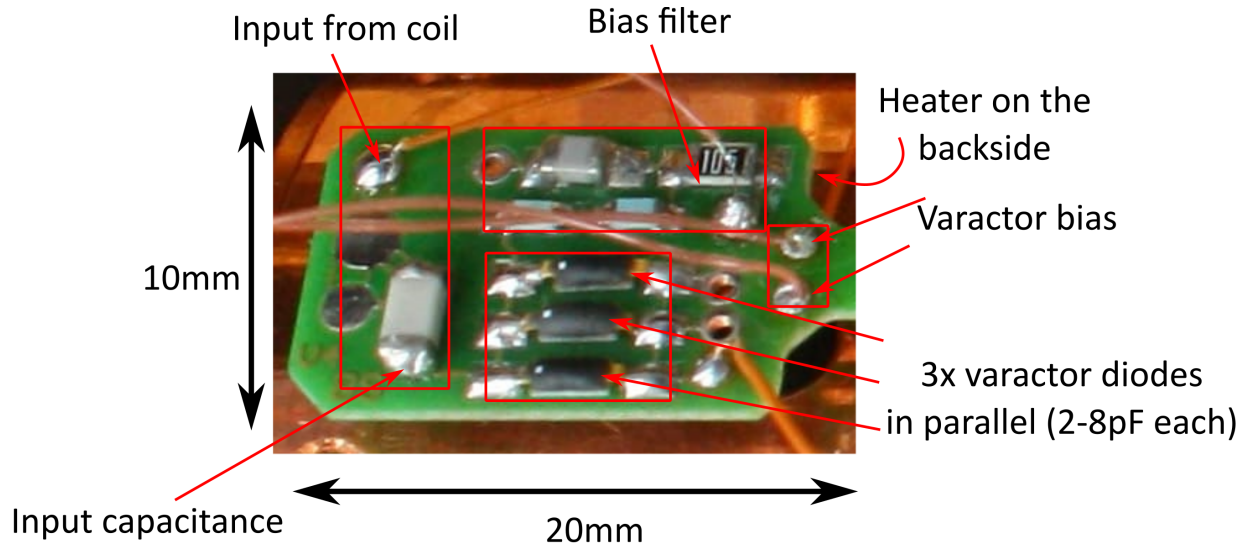
Figure A.1.: Custom-designed varactor board in collaboration with *Stahl Electronics* used to tune the ARES and CRES circuits.

The amplifiers in operation are the *'Cryogenic super low noise KC-05'* for the ARES and *'Dual Cryogenic RF-Amplifier KA-AMP4'* for the CRES from *Stahl electronics* [88].

A.2. EBIT and Wien filter settings

Table A.2.: Dresden EBIT settings for different ion species.

Source parameter	max.	typical
Electron current I_e (mA)	50	$10 - 30$
Electron energy E_e (keV)	15	$3 - 5$
Cathode potential U_{cath} (kV)	-3	-3
Central drift tube Potential U_2 (kV)	12	0.8 - 1.0
Extraction potential $U_{extr1,2,3}$ (kV)	-6,-6,-6	$<U_{cath}, \approx -2, \approx -2$
Magnetic field strength (mT)	250	
Ionisation factor α_{IF} (e/cm^2)	$\approx 10^{21}$	
Heating current I_{cath} (A)	2.1	1.9 - 2.1
Operation pressure (mbar)	10^{-8}	$3 - 4 \cdot 10^{-9}$
Breeding time t_{breed} (pulsed mode) (ms)	10000	$10 - 500$

Table A.3.: Wien filter setting for argon and a magnetic field strength of $B = 140\,\text{mT}$. The kinetic energies per charge for carbon and oxygen have been the same, with $E_{kin} \approx 900\,\text{eV}$, while the kinetic energy for argon was around $E_{kin} \approx 980\,\text{eV}$. Therefore the potentials for argon cannot directly be compared with those for carbon or oxygen.

Charge state	Potential (V)	Charge state	Potential (V)	Charge state	Potential (V)
Ar^{1+}	28	O^{1+}	44	C^{1+}	50
Ar^{2+}	40	O^{2+}	60	C^{2+}	70
Ar^{3+}	50	O^{3+}	74	C^{3+}	86
Ar^{4+}	57	O^{4+}	86	C^{4+}	99
Ar^{5+}	64	O^{5+}	95	C^{5+}	110
Ar^{6+}	69	O^{6+}	106	C^{6+}	122
Ar^{7+}	76	O^{7+}	-	-	-
Ar^{8+}	80	O^{8+}	-	-	-
Ar^{9+}	86	-	-	-	-
Ar^{10+}	90	-	-	-	-
Ar^{11+}	94	-	-	-	-
Ar^{12+}	98	-	-	-	-
Ar^{13+}	102	-	-	-	-
Ar^{14+}	106	-	-	-	-
Ar^{15+}	110	-	-	-	-
Ar^{16+}	114	-	-	-	-

A.3. HILITE beamtime operation parameters @ FLASH 2

Table A.4.: FLASH 2 and beamline FL24 operation parameters.

FL24 parameter	used	possible
Wavelength λ (nm)	$14 - 18$	$4 - 90$
Photon energy E_γ (eV)	$70 - 90$	$14 - 295$
Pulse energy E_{pulse} (µJ)	$2 - 400$	$1 - 500$
# bunches per second (1/s)	$10 - 4000$	$10 - 4000$
Focus diameter (µm)	$10 - 300$	$10 - \infty$
Focal length (mm)	2000	$2000 - 6000$
Beam height (mm)	1705	
Last beam defining aperture (mm)	3 (mainly)	3, 10, 16

Table A.5.: HILITE parameters used during the beamtime at FLASH.

Device	Parameter	C^{2+}	O^{5+}
EBIT	Electron energy E_e (keV)	3.94	3.94
	Cathode potential U_{cath} (kV)	-3.0	-3.0
	Central drift tube Potential U_2 (kV)	0.94	0.94
	Extraction potential $U_{extr1,2,3}$ (kV)	-3.9, -3.7, -1.5	-3.9, -3.7, -1.5
	Breeding time t_{breed} (ms)	11	25
	Opening time t_{open} (ms)	89	75
Wienfilter	Potential U_{wien} (V)	73	99
	Magnetic field B (mT)	140	140
90°-deflector	pos. potential U_{pos} (V)	227	225
	neg. potential U_{neg} (V)	-225	-225
Ion optics	Einzel lens potential U_{einzel} (V)	485	150
	Pulsed drift tube pos. potential U_{PDT} (V)	600	750
	Pulsed drift tube neg. potential U_{PDT} (V)	-245	-100
	Pulsed drift tube timing t_{PDT} (µs)	12.63	9.70
	MCP deflection U_{deflec} (V)	70, -70, -70, -70	-400, 100, 100, -150
Trap	Capture electrode (ion side) potential U_{pos} (V)	110	100
	Capture electrode (ion side) potential U_{neg} (V)	-50	-50
	Capture electrode (ion side) timing $t_{cap,ion}$ (µs)	14.29	10.69
	Endcap electrode (laser side) potential U_{end} (V)	90	60
	Endcap electrode (laser side) timing t_{end} (µs)	19.09	15.5
	Endcap electrode (laser side) downtime t_{dwon} (µs)	8.00	1.6
	Capture electrode (laser side) potential U_{cap} (V)	150	130
	Capture electrode (laser side) timing $t_{cap,laser}$ (µs)	13.76	11.8

Bibliography

[1] Hertz, H. "Ueber einen Einfluss des ultravioletten Lichtes auf die electrische Entladung". *Annalen der Physik und Chemie* **267** (8) (1887), pp. 983–1000. DOI: `10.1002/andp.18872670827`.

[2] Herrmann, K. H. *Der Photoeffekt*. Vieweg+Teubner Verlag, 1994. DOI: `10.1007/978-3-322-98787-7`.

[3] Hallwachs, W. "Ueber den Einfluss des Lichtes auf electrostatisch geladene Körper". *Annalen der Physik und Chemie* **269** (2) (1888), pp. 301–312. DOI: `10.1002/andp.18882690206`.

[4] Lenard, P. "Erzeugung von Kathodenstrahlen durch ultraviolettes Licht". *Annalen der Physik* **307** (6) (1900), pp. 359–375. DOI: `10.1002/andp.19003070611`.

[5] Planck, M. "Ueber das Gesetz der Energieverteilung im Normalspectrum". *Annalen der Physik* **309** (3) (1901), pp. 553–563. DOI: `10.1002/andp.19013090310`.

[6] Einstein, A. "Über einen die Erzeugung und Verwandlung des Lichtes betreffenden heuristischen Gesichtspunkt". *Annalen der Physik* **322** (6) (1905), pp. 132–148. DOI: `10.1002/andp.19053220607`.

[7] Strickland, D. and Mourou, G. "Compression of amplified chirped optical pulses". *Optics Communications* **55** (6) (Oct. 1985), pp. 447–449. DOI: `10.1016/0030-4018(85)90151-8`.

[8] Madey, J. M. J. "Stimulated Emission of Bremsstrahlung in a Periodic Magnetic Field". *Journal of Applied Physics* **42** (5) (Apr. 1971), pp. 1906–1913. DOI: `10.1063/1.1660466`.

[9] Penning, F. "Die Glimmentladung bei niedrigem Druck zwischen koaxialen Zylindern in einem axialen Magnetfeld". *Physica* **3** (9) (Nov. 1936), pp. 873–894. DOI: `10.1016/s0031-8914(36)80313-9`.

[10] Pierce, J. *Theory and Design of Electron Beams*. Van Nostrand, 1949.

Bibliography

[11] Major, F. G. and Dehmelt, H. G. "Exchange-Collision Technique for the rf Spectroscopy of Stored Ions". *Physical Review* **170** (1) (June 1968), pp. 91–107. DOI: `10.1103/physrev.170.91`.

[12] Dehmelt, H. G. and Walls, F. L. ""Bolometric" Technique for the rf Spectroscopy of Stored Ions". *Physical Review Letters* **21** (3) (July 1968), pp. 127–131. DOI: `10.1103/physrevlett.21.127`.

[13] Shockley, W. "Currents to Conductors Induced by a Moving Point Charge". *Journal of Applied Physics* **9** (10) (Oct. 1938), pp. 635–636. DOI: `10.1063/1.1710367`.

[14] Itano, W. M. et al. "Cooling methods in ion traps". *Physica Scripta* **T59** (Jan. 1995), pp. 106–120. DOI: `10.1088/0031-8949/1995/t59/013`.

[15] Guan, S. and Marshall, A. G. "Stored waveform inverse Fourier transform (SWIFT) ion excitation in trapped-ion mass spectometry: Theory and applications". *International Journal of Mass Spectrometry and Ion Processes* **157-158** (Dec. 1996), pp. 5–37. DOI: `10.1016/s0168-1176(96)04461-8`.

[16] Huang, X.-P. et al. "Phase-Locked Rotation of Crystallized Non-neutral Plasmas by Rotating Electric Fields". *Physical Review Letters* **80** (1) (Jan. 1998), pp. 73–76. DOI: `10.1103/physrevlett.80.73`.

[17] Hanneke, D., Fogwell, S., and Gabrielse, G. "New Measurement of the Electron Magnetic Moment and the Fine Structure Constant". *Physical Review Letters* **100** (12) (Mar. 2008). DOI: `10.1103/physrevlett.100.120801`.

[18] Mooser, A. et al. "Direct high-precision measurement of the magnetic moment of the proton". *Nature* **509** (7502) (May 2014), pp. 596–599. DOI: `10.1038/nature13388`.

[19] Heiße, F. et al. "High-Precision Measurement of the Proton's Atomic Mass". *Physical Review Letters* **119** (3) (July 2017). DOI: `10.1103/physrevlett.119.033001`.

[20] Levine, M. A. et al. "The Electron Beam Ion Trap: A New Instrument for Atomic Physics Measurements". *Physica Scripta* **T22** (Jan. 1988), pp. 157–163. DOI: `10.1088/0031-8949/1988/t22/024`.

[21] Donets, E. D., Ilyushchenko, V. I., and Alpert, V. A. "Ultrahigh Vacuum Electron Beam Source of Highly Stripped Ions." *Premiere Conference Internationale sur les Sources d'Ions* (Jan. 1970), pp. 635–642.

[22] Donets, E. and Ovsyannikov, V. "Investigation of ionization of positive ions by electron impact". *Sov. Phys. JETP* **53** (3) (1981), p. 466.

[23] Märk, T. D. *Electron impact ionization*. Wien New York: Springer-Verlag, 1985. ISBN: 3709140285.

[24] Ullmann, F. "Untersuchung der Erzeugung hochgeladener Ionen in einer Raumtemperatur-Elektronenstrahl-Ionenfale". PhD thesis. Fakultät für Mathematik und Naturwissenschaften, Technische Universität Dresden, 2006.

[25] Dreebit(GmbH). *Instruction Manual Dresden EBIT with Wien Filter*. 2010.

[26] Morgenroth, T. "Inbetriebnahme und erste Messungen einer Ionenquelle für HILITE". MA thesis. Institut für Optik und Quantenelektronik, Friedrich-Schiller-Universität Jena, 2017.

[27] Wien, W. "Untersuchungen über die electrische Entladung in verdünnten Gasen". *Annalen der Physik* **301** (6) (1898), pp. 440–452. DOI: 10.1002/andp.18983010618.

[28] Jackson, J. D. *Classical Electrodynamics*. John Wiley & Sons Inc, July 27, 1998. 832 pp. ISBN: 047130932X. URL: https://www.ebook.de/de/product/3240907/john_david_jackson_classical_electrodynamics.html.

[29] Fließbach, T. *Elektrodynamik*. Spektrum Akademischer Verlag, 2012. DOI: 10.1007/978-3-8274-3036-6.

[30] Reich, B. B. "Implementation and characterisation of an electrostatic ion beam deflector for the HILITE experiment". MA thesis. Fakultät für Physik und Astronomie, Ruprecht-Karls-Universität Heidelberg, 2020.

[31] Kreckel, H. et al. "A simple double-focusing electrostatic ion beam deflector". *Review of Scientific Instruments* **81** (6) (June 2010), p. 063304. DOI: 10.1063/1.3433485.

[32] Vogel, M. *Particle Confinement in Penning Traps*. Springer-Verlag GmbH, Mar. 30, 2018. ISBN: 3319762648. URL: https://www.ebook.de/de/product/32789560/manuel_vogel_particle_confinement_in_penning_traps.html.

[33] Murböck, T. et al. "Rapid crystallization of externally produced ions in a Penning trap". *Physical Review A* **94** (4) (Oct. 2016). DOI: 10.1103/physreva.94.043410.

[34] Gabrielse, G., Haarsma, L., and Rolston, S. "Open-endcap Penning traps for high precision experiments". *International Journal of Mass Spectrometry and Ion Processes* **88** (2-3) (Apr. 1989), pp. 319–332. DOI: 10.1016/0168-1176(89)85027-x.

[35] Brown, L. S. and Gabrielse, G. "Geonium theory: Physics of a single electron or ion in a Penning trap". *Reviews of Modern Physics* **58** (1) (Jan. 1986), pp. 233–311. DOI: 10.1103/revmodphys.58.233.

Bibliography

[36] Tan, J. and Gabrielse, G. "One electron in an orthogonalized cylindrical Penning trap". *Applied Physics Letters* **55** (20) (Nov. 1989), pp. 2144–2146. DOI: `10.1063/1.102084`.

[37] Gabrielse, G. and Mackintosh, F. "Cylindrical Penning traps with orthogonalized anharmonicity compensation". *International Journal of Mass Spectrometry and Ion Processes* **57** (1) (Apr. 1984), pp. 1–17. DOI: `10.1016/0168-1176(84)85061-2`.

[38] Kumar, S. et al. "Properties of a cylindrical Penning trap with conical endcap openings". *Physica Scripta* **94** (7) (Apr. 2019), p. 075401. DOI: `10.1088/1402-4896/ab0aaa`.

[39] Kretzschmar, M. "Particle motion in a Penning trap". *European Journal of Physics* **12** (5) (Sept. 1991), pp. 240–246. DOI: `10.1088/0143-0807/12/5/010`.

[40] Malmberg, J. H. and O'Neil, T. M. "Pure Electron Plasma, Liquid, and Crystal". *Physical Review Letters* **39** (21) (Nov. 1977), pp. 1333–1336. DOI: `10.1103/physrevlett.39.1333`.

[41] Kittel, C. *Introduction to Solid State Physics*. John Wiley & Sons Inc, Oct. 28, 2004. 704 pp. ISBN: 047141526X. URL: `https://www.ebook.de/de/product/4290142/charles_kittel_introduction_to_solid_state_physics.html`.

[42] Kiffer, M. "Selektive Breitbandanregung von Ionen in einer Penningfalle". Institut für Optik und Quantenelektronik, Friedrich-Schiller-Universität, 2016.

[43] McQuarrie, D. *Statistical mechanics*. Sausalito, Calif: University Science Books, 2000. ISBN: 9781891389153.

[44] Champenois, C. "Laser Cooling Techniques Applicable to Trapped Ions". *Advanced Textbooks in Physics*. World Scientific (Europe), Apr. 2016, pp. 117–145. DOI: `10.1142/9781786340139_0006`.

[45] Bryant, P. J. and Newman, W. S. "CAS - CERN Accelerator School : Antiprotons for Colliding-beam Facilities". CERN. Geneva, 1984. DOI: `10.5170/CERN-1984-015`. URL: `https://cds.cern.ch/record/157137`.

[46] Beverini, N. et al. "Stochastic cooling in Penning traps". *Physical Review A* **38** (1) (July 1988), pp. 107–114. DOI: `10.1103/physreva.38.107`.

[47] D'Urso, B. R. "Cooling and self-excitation of a one-electron oscillator". PhD thesis. Harvard University, Jan. 2003.

[48] Ringleb, S. "The HILITE setup for high-intensity-laser experiments with highly charged ions: design and commissioning". PhD thesis. Physikalisch-Astronomische Fakultät, Friedrich-Schiller-Universität Jena, 2020.

[49] Ramo, S. "Currents Induced by Electron Motion". *Proceedings of the IRE* **27** (9) (Sept. 1939), pp. 584–585. DOI: `10.1109/jrproc.1939.228757`.

[50] Ebrahimi, M. S. "Non-destructive detection and resistive cooling of highly-charged-ion ensembles for prescision spectroscopy in the ARTEMIS Penning trap". PhD thesis. Fakultät für Physik und Astronomie, Ruprecht-Karls-Universität Heidelberg, 2018.

[51] Carr, J. *Secrets of RF circuit design.* New York: McGraw-Hill, 2001. ISBN: 0071370676.

[52] Stahl, S. "Aufbau eines Experimentes zur Bestimmung elektronischer g-Faktoren einzelner wasserstoffähnlicher Ionen". PhD thesis. Institut für Physik, Joahnnes-Gutenberg-Universität Mainz, 1998.

[53] Johnson, J. B. "Thermal Agitation of Electricity in Conductors". *Physical Review* **32** (1) (July 1928), pp. 97–109. DOI: `10.1103/physrev.32.97`.

[54] Steinmann, J. "Analytical and numercial investigations of resistive cooling of trapped ion clouds". PhD thesis. Naturwissenschaftliche Fakultät, Friedrich-Alexander-Universität Erlangen-Nürnberg, 2016.

[55] Schlitt, B. et al. "Schottky mass spectrometry at the ESR: a novel tool for precise direct mass measurements of exotic nuclei". *Nuclear Physics A* **626** (1-2) (Nov. 1997), pp. 315–325. DOI: `10.1016/s0375-9474(97)00552-6`.

[56] Kiffer, M. et al. "Single-pass non-destructive electronic detection of charged particles". *Review of Scientific Instruments* **90** (11) (Nov. 2019), p. 113301. DOI: `10.1063/1.5110988`.

[57] Kiffer, M. "Non-destructive single-pass detection of highly charged ions". MA thesis. Institut für Optik und Quantenelektronik, Friedrich-Schiller-Universität Jena, 2019.

[58] Wineland, D. J. and Dehmelt, H. G. "Principles of the stored ion calorimeter". *Journal of Applied Physics* **46** (2) (Feb. 1975), pp. 919–930. DOI: `10.1063/1.321602`.

[59] ARRL. *The ARRL handbook for radio amateurs, 1994.* Newington, CT: American Radio Relay League, 1993. ISBN: 0872591719.

[60] Joachain, C. J., Kylstra, N. J., and Potvliege, R. M. *Atoms in Intense Laser Fields.* Cambridge University Press, 2011. DOI: `10.1017/cbo9780511993459`.

Bibliography

[61] Göppert-Mayer, M. "Elementary processes with two quantum transitions". *Annalen der Physik* **18** (7-8) (July 2009), pp. 466–479. DOI: 10.1002/andp.200910358.

[62] Beier, T. "The g-factor of a bound electron and the hyperfine structure splitting in hydrogenlike ions". *Physics Reports* **339** (2-3) (Dec. 2000), pp. 79–213. DOI: 10.1016/s0370-1573(00)00071-5.

[63] Keldysh, L. "Ionization in the Field of a Strong Electromagnetic Wave". *Sov. Phys. JETP* **20** (5) (1965), p. 1307.

[64] Ammosov, M., Delone, N., and Krainov, V. "Tunnel ionization of complex atoms and of atomic ions in an alternating electromagnetic field". *Sov. Phys. JETP* **64** (6) (1986), p. 1191.

[65] Damon, E. K. and Tomlinson, R. G. "Observation of Ionization of Gases by a Ruby Laser". *Applied Optics* **2** (5) (May 1963), p. 546. DOI: 10.1364/ao.2.000546.

[66] Voronov, G. and Delone, N. "Many-photon Ionization of the Xenon Atom by Ruby Laser Radiation". *Sov. Phys. JETP* **23** (1) (1965), p. 54.

[67] Agostini, P. et al. "Free-Free Transitions Following Six-Photon Ionization of Xenon Atoms". *Physical Review Letters* **42** (17) (Apr. 1979), pp. 1127–1130. DOI: 10.1103/physrevlett.42.1127.

[68] Dreebit GmbH. URL: https://www.dreebit-ibt.com/.

[69] Amptek. *XR-100CR Si-PIN X-Ray Detector*. URL: https://www.amptek.com/products/x-ray-detectors/si-pin-x-ray-detectors-for-xrf/xr-100cr-si-pin-x-ray-detector.

[70] Beam Imaging Solutions. *Columbia CIBD-100-H*. URL: http://beamimaging.com/product/columbia-cibd-100-h/.

[71] Scientific Instrument Services. *SIMION - The field and particle trajectory simulator*. URL: https://simion.com/.

[72] PHOTONIS. *Advanced Performance Detectors*. URL: https://www.photonis.com/products/advanced-performance-detectors.

[73] Kumar, S. "Desgin and setup of a Penning trap for the study of ions in extreme laser fields". PhD thesis. Inter-University Accelerator Centre New Delhi, 2020.

[74] DESY. *Free-electron laser FLASH*. URL: https://flash.desy.de/.

[75] Raimondi, L. et al. "Kirkpatrick–Baez active optics system at FERMI: system performance analysis". *Journal of Synchrotron Radiation* **26** (5) (Aug. 2019), pp. 1462–1472. DOI: 10.1107/s1600577519007938.

[76] Tamasaku, K. et al. "Nonlinear Spectroscopy with X-Ray Two-Photon Absorption in Metallic Copper". *Physical Review Letters* **121** (8) (Aug. 2018). DOI: 10.1103/physrevlett.121.083901.

[77] Sorokin, A. A. et al. "Photoelectric Effect at Ultrahigh Intensities". *Phys. Rev. Lett.* **99** (21 Nov. 2007), p. 213002. DOI: 10.1103/PhysRevLett.99.213002. URL: https://link.aps.org/doi/10.1103/PhysRevLett.99.213002.

[78] Doumy, G. et al. "Nonlinear Atomic Response to Intense Ultrashort X Rays". *Physical Review Letters* **106** (8) (Feb. 2011). DOI: 10.1103/physrevlett.106.083002.

[79] Hofbrucker, J. *Ionisation rates for laser ionisation.* Private communication. 2019.

[80] Reiss, H. R. "Foundations of the Strong-Field Approximation". *Progress in Ultrafast Intense Laser Science III.* Berlin, Heidelberg: Springer Berlin Heidelberg, 2008, pp. 1–31. ISBN: 978-3-540-73794-0. DOI: 10.1007/978-3-540-73794-0_1. URL: https://doi.org/10.1007/978-3-540-73794-0_1.

[81] Kersevan, R. and Ady, M. "Recent Developments of Monte-Carlo Codes Molflow+ and Synrad+". en. *Proceedings of the 10th Int. Particle Accelerator Conf.* **IPAC2019** (2019), Australia. DOI: 10.18429/JACOW-IPAC2019-TUPMP037.

[82] Baglin, V. "Cold/sticky systems". Geneva, May 2006.

[83] Chubb, J. and Pollard, I. "Experimental studies of hydrogen condensation on to liquid helium cooled surfaces". *Vacuum* **15** (10) (Oct. 1965), pp. 491–496. DOI: 10.1016/0042-207x(65)90344-1.

[84] Battes, K., Day, C., and Hauer, V. "Outgassing rate measurements of stainless steel and polymers using the difference method". *Journal of Vacuum Science & Technology A: Vacuum, Surfaces, and Films* **33** (2) (Mar. 2015), p. 021603. DOI: 10.1116/1.4905099.

[85] Vacom. *Ausgasraten von Aluminium im Vergleich zu Edelstahl.* URL: https://www.vacom.de/downloads/white-paper?download=3025:ausgasraten-von-aluminium-im-vergleich-zu-edelstahl.

Bibliography

[86] Mandal, P., Sikler, G., and Mukherjee, M. "Simulation study and analysis of a compact einzel lens-deflector for low energy ion beam". *Journal of Instrumentation* **6** (02) (Feb. 2011), P02004–P02004. DOI: 10.1088/1748-0221/6/02/p02004.

[87] Schmöger, L. et al. "Deceleration, precooling, and multi-pass stopping of highly charged ions in Be⁺ Coulomb crystals". *Review of Scientific Instruments* **86** (10) (Oct. 2015), p. 103111. DOI: 10.1063/1.4934245.

[88] Stahl, S. *Stahl electronics*. URL: https://www.stahl-electronics.com/index.html.

List of publications

[1] Stallkamp, N. et al. "HILITE – A well-defined ion target for laser experiments". *Journal of Physics: Conference Series* **1412** (Jan. 2020), p. 092009. DOI: `10.1088/17 42-6596/1412/9/092009`.

[2] Kiffer, M. et al. "Characterisation of ion bunches by a single-pass non-destructive charge counter". *Journal of Physics: Conference Series* **1412** (Jan. 2020), p. 242004. DOI: `10.1088/1742-6596/1412/24/242004`.

[3] Stallkamp, N. et al. "HILITE—A tool to investigate interactions of matter and light". *X-Ray Spectrometry* **49** (1) (June 2019), pp. 188–191. DOI: `10.1002/xrs.3087`.

[4] Kiffer, M. et al. "Single-pass non-destructive electronic detection of charged particles". *Review of Scientific Instruments* **90** (11) (Nov. 2019), p. 113301. DOI: `10.1063/1.51 10988`.

[5] Kumar, S. et al. "Properties of a cylindrical Penning trap with conical endcap openings". *Physica Scripta* **94** (7) (Apr. 2019), p. 075401. DOI: `10.1088/1402-4896 /ab0aaa`.

[6] Wiesel, M. et al. "Optically transparent solid electrodes for precision Penning traps". *Review of Scientific Instruments* **88** (12) (Dec. 2017), p. 123101. DOI: `10.1063/1.50 02180`.

Talks and poster presentations

- International Conference on Precision Physics of Simple Atomic systems (PSAS 2016 Jerusalem): Poster presentation

- European Conference on Atoms, Molecules and Photons (ECAMP 2017 Frankfurt): Poster presentation

- Deutsche Physikalische Gesellschaft Frühjahrstagung (DPG 2017 Mainz): Poster presentation

- Conference on Precision Physics, Quantum Electrodynamics and Fundamental Interactions (2017 Cargèse): Poster presentation

- 19th International Conference on the Physics of Highly Charged Ions (HCI 2018 Lisbon): Poster presentation

- Young scientists GSI-FAIR Poster Colloquium (2019 Darmstadt): Poster presentation (Best Poster Award)

- 31st International Conference on Photonic, Electronic and Atomic Collisions (ICPEAC 2019 Deauville): Poster presentation

- 16th Stored Particles Atomic Physics Research Collaboration Topical workshop (SPARC 2019 Jena): Oral presentation

Ehrenwörtliche Erklärung

Ich erkläre hiermit ehrenwörtlich, dass ich die vorliegende Arbeit selbständig, ohne unzulässige Hilfe Dritter und ohne Benutzung anderer als der angegebenen Hilfsmittel und Literatur angefertigt habe. Die aus anderen Quellen direkt oder indirekt übernommenen Daten und Konzepte sind unter Angabe der Quelle gekennzeichnet.

Die Arbeit wurde bisher weder im In- noch im Ausland in gleicher oder ähnlicher Form einer anderen Prüfungsbehörde vorgelegt. Die geltende Promotionsordnung der Physikalisch-Astronomischen Fakultät ist mir bekannt.

Ich versichere ehrenwörtlich, dass ich nach bestem Wissen die reine Wahrheit gesagt und nichts verschwiegen habe.

_____   _____

Ort, Datum   Unterschrift